ABSTRACT

Title of Dissertation: INVESTIGATING THE ROLE(S) OF MAMMALIAN HEME TRANSPORT BY HRG1

Rini Hartono Pek, Doctor of Philosophy, 2019

Dissertation directed by: Professor Iqbal Hamza
Department of Animal and Avian Sciences

The recycling of hemoglobin from damaged or senescent red blood cells (RBCs) contributes almost 90% of daily body iron requirements in humans for bone marrow erythropoiesis. Previously, our cell biological studies have shown that HRG1, a four transmembrane protein first discovered in *C. elegans*, facilitates the transport of heme within reticuloendothelial system (RES) macrophages during the turnover of RBCs, a process termed erythrophagocytosis. HRG1 transports heme from the phagolysosomes into the cytosol where heme is degraded to liberate iron for erythropoiesis. Here we show that mice deficient for *HRG1* are defective in heme-iron recycling by RES macrophages, resulting in over ten-fold excess heme accumulation as visible dark pigments within lysosomal compartments that are 10-100 times larger than normal. The sequestered heme is tolerated by macrophages through polymerization into crystallized hemozoin, a phenomenon typically observed in blood-feeding parasites as a detoxification method to protect against heme toxicity. *HRG1*$^{-/-}$ mice display ineffective bone marrow erythropoiesis which results in a

reduction in hematocrit and extramedullary erythropoiesis in the spleen. Under iron-deficient conditions *HRG1*$^{-/-}$ mice are unable to utilize hemozoin as an iron source to sustain erythropoiesis, causing severe anemia and lethality. Our studies establish that polymerizing cytotoxic heme into hemozoin is a previously-unanticipated heme tolerance pathway in mammals.

INVESTIGATING THE ROLE(S) OF MAMMALIAN HEME TRANSPORT BY HRG1

by

Rini Hartono Pek

Dissertation submitted to the Faculty of the Graduate School of the
University of Maryland, College Park, in partial fulfillment
of the requirements for the degree of
Doctor of Philosophy
2019

Advisory Committee:
Professor Iqbal Hamza, Chair
Dr. David M. Bodine
Dr. Sougata Roy
Dr. Chad Stahl
Dr. Antony Jose, Dean's Rep

Dedication

For all of my teachers

Acknowledgements

I am extremely blessed to be able to complete this chapter of my life, and I owe much of this to the people who have supported me on this journey. I would like to thank the people who helped me to get into graduate school: my previous mentors Jacklyn, Prof. Chew and Prof. Yas. Jacklyn was the first mentor I had in a lab, and watching the way she worked really set the tone for the way I work in the lab, even till today. Thank you for your patience and friendship. Prof. Chew and Yas accepted me into their labs as an undergraduate student and supported me in applying to graduate schools in the United States.

Thank you to my biggest mentor through the past five years, Xiaojing. Thank you for being so giving and patient with me. Thank you for listening to my endless complaining and for being the best collaborator I could have in the lab. I would also like to thank Nicole, who never turned down my requests for help with experiments. Thank you for being an amazing lab partner with strong work ethics. Thank you Jianbing for your generous help and advice in and out of work. Thank you Dave (Drescher) for being so reliable in the lab. Thank you Kate and Tamika, for helping me when we worked together, but more importantly for your friendship and support out of the lab, you both truly are gems. And thank you to all the other members in the Hamza lab that I have interacted with. Thank you Elda, Ana, Maya, Ian, Abisha and Sohini for the time we spent in lab. It is nice to not be alone in this long journey. These people have taught me many different things that have empowered me along the way.

Thank you to my friends here and back home, who always want nothing but the best for me. Thank you Weilun, Louise, Derek, Jiaxin, Qiuping and Janel, for your friendship and support. Thank you Hanyin for your generosity and love from miles away. Thank you Wenlin, for all the fun, laughter, and woes we share in this journey. Thank you Casey, for loving and protecting me in ways I never imagined.

Finally, I would not be here without the constant support from my family. Thank you Ryan, for being the rock of the family. Thank you to my grandmother, Aunt and cousins for quietly loving and supporting me. Thank you to my father, who taught me that I can do anything I want to; I just have to start with learning. And to my mother, words cannot convey my gratitude towards you. You are the representation of strength, selflessness, tenacity, and compassion. You are the first and most important teacher in my life, this is for you.

Professional Acknowledgements

I am honored to share this project with a dedicated group of scientists who has contributed tremendously in different ways. I would like to thank everybody who was involved in the generation of the *HRG1*$^{-/-}$ mouse: Dr. David Bodine, Ms. Lisa Garrett, Mr. Will Simmons and Ms. Jaya Jagadeesh. Thank you to Dr. John Phillips, Dr. Malay Haldar, Dr. Martina Ralle and Dr. Hiroshi Sugimoto for sharing your time and expertise on this project. Thank you Dr. Laurie Jackson and Mr. Hector Bergonia, who analyzed more than 300 mouse samples that we had sent to you. Thank you Ms. Stacie Anderson and Ms. Martha Kirby, for your guidance and help with flow cytometry-related experiments. Thank you Mr. Edward Case, for taking time out of your schedule to help with all the radioactive counting we had to do.

Thank you to the animal care facility members, Ms. Jessica Karunaratne and Ms. Mariana Guillen, for doing daily checks on the mice even on days of campus closure, and for notifying me of any happenings in the mouse room. I appreciate your dedication. Thank you Ms. Elda Kwong and Ms. Abisha Dowla for leading and supporting the dietary pig studies, sacrificing your time and effort to ensure that the piglets were well taken care of.

Thank you Ms. Gwen Warman (BISI Program Coordinator) for always being helpful when I had administrative questions or requests throughout my PhD. All of us graduate students in BISI are so fortunate to have you as our coordinator.

Thank you to my PhD committee members (Dr. David Bodine, Dr. Antony Jose, Dr. Sougata Roy, Dr. Chad Stahl) for providing guidance with your honest feedback for this project. Special thanks to Dave for your mentorship and for always

showing your appreciation for my work. Thank you for being someone I know I can count on for support and advice.

Finally, thank you Iqbal, for allowing me to pursue this wonderful project in your lab, for giving me the opportunities to keep learning, for guiding me to become a better scientist, and for having high expectations of me which only pushed me to achieving more. Thank you for trusting all of us with this project, I hope we did not let you down.

Table of Contents

List of Figures and Tables

Figures

Tables

List of Abbreviations

ACD	anemia of chronic disease
ALA	δ-aminolevulinic acid
ALAD	ALA dehydratase
ALAS	δ-aminolevulinic acid synthase
Bach-1	BTB and CNC homology 1
BFU-E	burst- forming unit- erythroid
BMDM	bone marrow derived macrophages
BMP	bone morphogenetic protein
CD163	cluster of differentiation receptor 163
CFU-E	colony- forming unit- erythroid
Cp	ceruloplasmin
CPgenIII	coproporphyrinogen III
CPOX	coproporphyrinogen oxidase
CRISPR	clustered regularly interspaced short palindromic repeats
DcytB	duodenal cytochrome b
DMT1	divalent metal transporter 1
EBI	erythroblastic island
EP	erythrophagocytosis
EPO	erythropoietin
ERFE	erythroferrone
FACS	Fluorescence activating cell sorting
FBXL5	F box and leucine-rich repeat protein 5
FECH	ferrochelatase
Fe-S	iron-sulfur cluster
FLVCR1	feline leukemia virus subgroup C receptor-related protein 1
Fpn	ferroportin
FTH1	ferritin heavy chain1
FTL	ferritin light chain
Hamp	hepcidin
HCP1	heme carrier protein 1
Heph	hephaestin
HIF	hypoxia-inducible factor
Hmox1, HO1	heme oxygenase 1
Hmox2, HO2	heme oxygenase 2
Hp	haptoglobin
Hpx	hemopexin
HRG1	Heme Responsive Gene -1

HRI	heme regulated inhibitor
HSC	hematopoietic stem cell
Hz	hemozoin
ICAM-1	intercellular adhesion molecule 1
IDA	Iron-deficiency anemia
IFN-γ	interferon-γ
IL-6	interleukin-6
iNOS	iron-regulated inducible NO synthase
IRE	iron responsive element
IRP	iron regulatory protein
Lamp1	Lysosomal-associated membrane protein 1
MARE	MAF recognition elements
MFRN	mitoferrin
mRNA	messenger RNA
NCOA4	nuclear receptor coactivator 4
NMR	nuclear magnetic resonance
NO	nitric oxide
NRAMP1	natural resistance-associated macrophage protein 1
NTBI	non transferrin bound iron
PBG	porphobilinogen
PBGD	porphobilinogen deaminase
PCBP	Poly r(C)-binding protein
PPgenIX	protoporphyrinogen IX
PPIX	protoporphyrin IX
PPOX	protoporphyrinogen oxidase
PS	phosphatidylserine
RBC	Red blood cell
RES	reticuloendothelial system
RPM	red pulp macrophage
SA	succinylacetone
SLC	solute carrier
Stat5	signal transducer and activator of transcription 5
STEAP3	six-transmembrane epithelial antigen of prostate 3 reductase
Tfn	transferrin
TfR1	transferrin receptor 1
TLR-4	toll-like receptor-4
TNF-α	tumor necrosis factor-α
UROD	uroporphyrinogen decarboxylase
UROgen III	uroporphyrinogen III
UROS	uroporphyrinogen synthase
VCAM-1	vascular cell adhesion molecule 1
WT	wildtype

Chapter 1 : Introduction

Heme is a tetrapyrrole that functions as a signaling molecule or cofactor to support numerous biological processes. As an iron-containing porphyrin, heme metabolism is invariably related to the metabolism of the inorganic micronutrient, iron. However, in comparison to iron, the mechanisms of inter- and intra-cellular heme transport are less clearly defined. Delineation of heme transport pathways has remained challenging due to the high binding affinity of heme to cellular proteins which maintains the low concentration of cellular labile heme at ~0.4 μM[1]. The utilization of genetics and whole animal nutritional studies in an animal model of heme transport deficiency represent our current efforts to define the necessity of heme transport in maintaining iron and heme homeostasis.

Heme Biosynthesis

In eukaryotic cells, heme is typically synthesized via a widely-conserved eight-step pathway which requires coordinated substrate transport between mitochondria and the cytosol[2]. The first step occurs in the mitochondrial matrix and is catalyzed by δ-aminolevulinic acid synthase (ALAS), resulting in the synthesis of δ-aminolevulinic acid (ALA) from glycine and succinyl-coenzyme A. Subsequently, ALA is transported out of mitochondria and into the cytosol where four enzymatic reactions follow: 1) ALA is converted to porphobilinogen (PBG) by ALA dehydratase (ALAD); 2) PBG to an unstable polymer hydroxymethylbilane by porphobilinogen deaminase (PBGD); 3) hydroxymethylbilane to uroporphyrinogen III (UROgen III) by uroporphyrinogen synthase (UROS); and 4) UROgen III to

coproporphyrinogen III (CPgen III) by uroporphyrinogen decarboxylase (UROD). CPgen III is then transported back into mitochondria where coproporphyrinogen oxidase (CPOX), a mitochondrial intermembrane space enzyme, catalyzes the formation of protoporphyrinogen IX (PPgen IX). PPgen IX is then converted to protoporphyrin IX (PPIX) by the inner mitochondrial membrane enzyme protoporphyrinogen oxidase (PPOX). The final step requires ferrochelatase (FECH) which facilitates the insertion of ferrous iron (Fe^{2+}) into PPIX to form heme. Therefore, heme is a tetrapyrrole made up of an iron-protoporphyrin complex. The electrical charge of the molecule is dependent on the ionic state of the central iron atom: heme, or ferroprotoporphyrin, is electrically neutral as the iron atom is in the ferrous (Fe^{2+}) state while hemin, or ferriprotoporphyrin, is positively charged as the iron atom is in the ferric (Fe^{3+}) state. Heme contains four methyl groups, two vinyl groups, and two propionic acid groups as side chains and is hydrophobic in nature[3].

Iron metabolism in mammals

Iron acquisition

Iron is a trace element essential to eukaryotic life. In mammals, absorption of inorganic iron begins with the reduction of ferric (Fe^{3+}) to ferrous (Fe^{2+}) iron, often catalyzed by the membrane-associated ferrireductase duodenal cytochrome b (Dcytb)[4] **(Fig. 1.1)**. Divalent metal transporter 1 (*DMT1/SLC11A2*), solute carrier family 11 member 2, or natural resistance-associated macrophage protein 2 (*NRAMP2*) catalyzes the transport of Fe^{2+} across the apical membrane in the duodenal epithelia[5] **(Fig. 1.1)**. Export of Fe^{2+} out of the intestinal epithelia and into circulation is facilitated by the transmembrane transporter, ferroportin/SLC40A1 (Fpn)[5] **(Fig. 1.1)**.

Ferroportin-associated export of Fe^{2+} is coupled to the oxidation of Fe^{2+} into Fe^{3+} by ferroxidases, the serum ceruloplasmin (Cp) or membrane-bound hephaestin (Heph) **(Fig. 1.1)**. Hephaestin is expressed on the basolateral membrane of duodenal enterocytes and physically interacts with ferroportin for iron export[6]. Fe^{3+} is subsequently bound by apo-transferrin (apo-Tf), which transports the redox inert iron to various tissues. Each Tf molecule contains two Fe^{3+} binding sites and under physiological iron conditions, plasma Tf is only partially saturated with iron (30-40%)[7]. The reservoir of abundant unsaturated apo-Tf acts as a buffer, which allows efficient binding when plasma iron levels increase. This buffering capacity prevents the buildup of non-transferrin-bound iron (NTBI), which is a major contributor to tissue iron loading in iron overload disorders as NTBI taken up by tissue parenchymal cells[8]. During iron overload, NTBI builds up when the levels of plasma iron exceeds the buffering capacity of transferrin at about 60% saturation. NTBI overload is directed mainly to the liver and NTBI import into hepatocytes occurs through *ZIP14/SLC39A14*[9]. In the absence of *ZIP14*, NTBI loading in the liver and pancreas is drastically reduced and directed to extra-hepatic tissues such as the kidney[10].

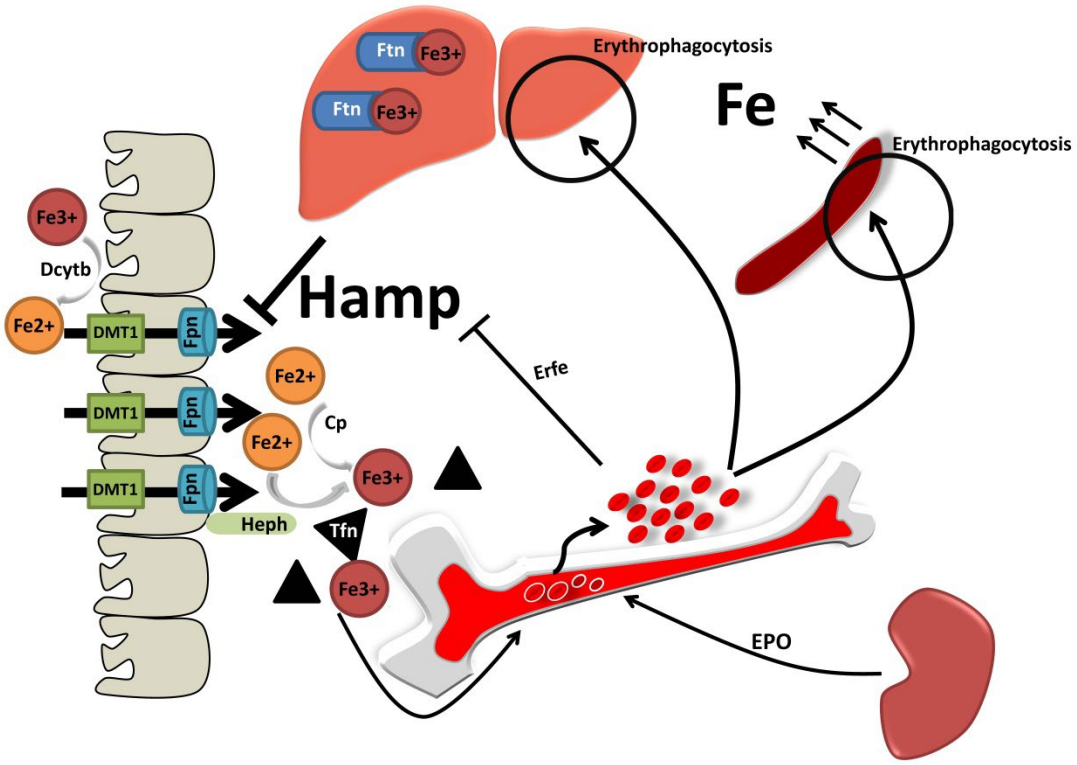

Figure 1.1 Iron metabolism in mammals

Ferric iron (Fe^{3+}) is converted by Dcytb into ferrous iron (Fe^{2+}) and transported into intestinal epithelial cells via DMT1 at the apical surface. Ferroportin (Fpn) exports Fe^{2+} through the basolateral surface of the epithelia where Fe^{2+} is converted into Fe^{3+} by ceruloplasmin (Cp) or hephaestin (Heph). Transferrin (Tfn) binds Fe^{3+} and transports iron through the circulation to different sites such as the bone marrow. Erythropoiesis in the bone marrow is stimulated by erythropoietin (EPO) secreted by the kidney. Erythrocytes remain in circulation and are phagocytosed in the spleen and liver upon senescence. Iron storage in tissues such as the liver is mediated by ferritin (Ftn). The liver produces hepcidin (Hamp), which negatively regulates iron absorption through Fpn. Hepcidin is in turn negatively regulated by erythroferrone (Erfe) produced by erythroblasts.

Heme as a dietary iron source

Another major dietary source of iron is heme, which has been shown to be more readily absorbed than inorganic iron in the human intestine[11,12]. In the intestine, heme is taken up by enterocytes as an intact metalloporphyrin[13,14], although the molecules responsible for intestinal heme uptake remain unknown. Intestinal heme uptake was initially demonstrated in swine and canine animal models using [^{59}Fe]heme. In intestinal brush border extracts isolated from adult pig duodenum, heme absorption and binding to a "heme receptor" was observed through spectrophotometric measurements[15]. A high-affinity heme-binding protein extracted from microvilli membranes of enterocytes was proposed to facilitate heme internalization into vesicles. In a different study, Mongrel dogs were fed with a diet containing [^{59}Fe]hemoglobin to evaluate dietary heme absorption[16]. The dogs were made iron-deficient by phlebotomy and fed with hemoglobin. In iron-deficient dogs, higher plasma [^{59}Fe]heme levels and greater [^{59}Fe]hemoglobin absorption was observed. Based on these studies, two long-standing hypotheses of intestinal heme uptake were proposed. The first hypothesis, receptor-mediated endocytosis, arose from early studies on the "heme receptor protein" (described above)[15] and the second, transporter-mediated uptake[17] was conceived after heme transporters such as *FLVCR1* (Feline leukemia virus subgroup C receptor-related protein 1) and *HCP1* (heme carrier protein 1) were discovered. *FLVCR1*, a cell surface heme exporter involved in erythroid cell maturation, prevents cell toxicity by exporting excess intracellular heme[18]. *HCP1* was first described to be a heme importer but it was later

independently characterized as a folate transporter[19]. Therefore, the *bona fide* intestinal heme transporter remains elusive.

Iron storage and distribution

In humans, there exists a total of ~3–5 g of iron[5] and 70% of total body iron (>2 g) exists in red blood cells (RBCs). Within RBCs, majority of the total iron is stored as heme in hemoglobin[20]. A portion of iron is also found as heme present in myoglobin of muscles (~300 mg). Macrophages residing within the spleen, liver, and bone marrow, collectively termed reticuloendothelial macrophages store a transient fraction of iron (~600 mg), while excess iron (~1000 mg) is stored within cellular ferritin in liver parenchymal cells. A minimal amount of intracellular iron is also bound to proteins and enzymes (~8 mg)[6].

Tissue iron not utilized in biological processes is stored within a cytosolic heteropolymer protein made of 24 subunits of heavy (FTH1) and light (FTL) ferritin chains, together known as the ferritin nanocage. Although both FTH1 and FTL are ubiquitous, the ratios of FTH1 and FTL expression vary between tissues and physiological conditions. FTL is predominantly found in iron storage tissues, while FTH1 is preferentially expressed in cells that acquire and export iron rapidly. Each ferritin nanocage can store up to 4500 iron atoms. FTH1 contains the ferroxidase activity required for the conversion of Fe^{2+} to Fe^{3+} for iron mineralization into the polymer while the enzymatically inactive FTL facilitates the transfer of electrons across the protein shell of the polymer[21]. In plasma, a glycosylated FTL subunit circulates and exhibits a low level of saturation with iron, although its origin and mechanism of release into circulation is debated. Serum ferritin levels have been

shown to increase in response to systemic iron overload or infection, and are therefore commonly used as biomarkers of such physiological conditions[22].

The mechanism of iron delivery to ferritin is aided by the cytosolic iron chaperone of Poly r(C)-binding protein (PCBP)[23]. PCBP1 and its paralog PCBP2 were shown to interact at high affinities with ferritin in HEK293 cells. In yeast, the concurrent expressions of *PCBP1*, *PCBP2*, and human ferritins activate an iron-deficiency response by increasing iron deposition into ferritin. However, only the knockdown of *PCBP1* but not *PCBP2* resulted in an impaired iron utilization phenotype during RBC maturation. Mice lacking *PCBP1* develop microcytic anemia as a result of ineffective RBC maturation[24].

Cellular iron stores can be mobilized by ferritin degradation. Under iron-deficient conditions, NCOA4 (Nuclear Receptor Coactivator 4) interacts with FTH1, which targets the ferritin complex for degradation in autolysosomes. This stimulates release of ferritin iron stores in a process known as ferritinophagy. In iron-replete conditions, cellular ferritinophagy is suppressed due to increased NCOA4 turnover[25]. *NCOA4*-deficient mice do not experience ferritinophagy, resulting in cellular ferritin accumulation and iron-deficiency anemia. The increase in cellular iron storage by ferritin accumulation causes an imbalance in systemic iron distribution and reduces iron availability for developing erythroblasts[26].

Systemic iron regulation

As ferroportin is the only known mammalian exporter of inorganic iron and ferroportin inactivation enhances intracellular iron retention, a critical regulation of iron metabolism occurs via the ferroportin-hepcidin axis. The liver-derived peptide

hepcidin negatively regulates ferroportin by binding to ferroportin on the plasma membrane of cells including enterocytes, macrophages, and hepatocytes. This interaction induces phosphorylation and internalization of ferroportin, resulting in its lysosomal degradation[27,28]. Hepcidin has also been implicated in the proteasomal degradation of DMT1[29].

Hepcidin (Hamp) is produced as an 84 amino acid precursor propeptide[30] **(Fig. 1.1)**. Post translationally, the prohormone convertase furin cleaves hepcidin into a biologically active 25 amino acid mature peptide, which is subsequently secreted into plasma[31]. Regulation of hepcidin expression occurs at the transcriptional level via the CCAAT enhancer-binding protein α (C/EBPα). C/EBPα binds to a CCAAT motif within the HAMP promoter to maintain its basal transcriptional activity[32]. Basal hepcidin expression is also shown to be maintained by Alk3, a type I bone morphogenetic protein (BMP) receptor[33]. In iron-deficiency, hepcidin repression occurs to trigger iron absorption and release of iron stores for increased erythropoiesis. Erythropoiesis is dependent on the kidney-produced cytokine erythropoietin (EPO) and recently, an EPO-responsive erythroid regulator of hepcidin, named erythroferrone (ERFE, also known as FAM132B and myonectin) was identified[34] **(Fig. 1.1)**. EPO induces erythroblastic ERFE secretion by signaling through the JAK2/STAT5 pathway[34]. *ERFE*-deficient mice are unable to suppress hepcidin during hemolysis or EPO stimulation[34]. Hepcidin expression can be induced by a variety of stimulants including hepatic iron loading or inflammation, leading to decreased iron uptake and mobilization.

Hepcidin transcription is induced upon hepatic iron loading via the BMP signaling pathway[35]. Hepatic iron induces expression of *BMP6* and mRNA levels of *BMP6* are correlated to hepatic iron loading in mice[36]. BMP6 (and other BMP ligands) binding to BMP receptors induces phosphorylation of SMAD1, SMAD5, and SMAD8 proteins[33]. The phosphorylated SMAD1/5/8 complex together with SMAD4 binds to the BMP responsive elements on the hepcidin promoter and stimulates hepcidin transcription[37]. Mice with a liver-specific disruption of BMP receptors Alk2, Alk3[33], or SMAD4[38] display defects in iron-induced hepcidin expression[39]. Mice lacking hepatic *BMP6* are unable to induce hepcidin and therefore suffer from iron overload[40,41]. Conversely, treatment of recombinant BMP6 in mice leads to increased production of hepcidin and hypoferremia[41].

Cellular iron regulation

Cellular iron metabolism, unlike systemic iron metabolism, is highly regulated at the post-transcriptional level by iron regulatory proteins (IRPs) in the cytoplasm. IRP1 and IRP2 bind to iron-responsive elements (IREs) on mRNAs and the interaction often determines the fates of iron-related mRNAs. Removal of either IRP1 or IRP2 is not lethal, but the ablation of both IRPs results in embryonic lethality at the early blastocyst stage[42]. The absence of both IRPs in the intestine has been associated with defects in growth and ineffective intestinal absorption, indicating the importance of IRPs in the intestine and duodenum[43] while hepatocyte-specific removal of IRPs leads to liver damage and premature death[44].

Under iron-replete conditions, IRP1 acquires an iron-sulfur cluster (4Fe-4S) and functions as an aconitase in the cytosol, catalyzing the conversion of citrate to

iso-citrate. The aconitase form of IRP1 is unable to bind to IREs. By contrast, the 4Fe-4S cluster is absent in IRP1 during iron-deficiency which allows for subsequent IRE-binding by IRP1[45]. Unlike IRP1, IRP2 is regulated by a different mechanism. In iron-replete conditions, IRP2 is ubiquitinated by FBXL5, an E3 ubiquitin ligase, and undergoes proteasomal degradation[46]. *FBXL5* ablation in mice causes death early in embryogenesis, due to iron accumulation and iron-induced tissue damage[47]. The *FBXL5*-ablation-associated death could be prevented by an additional ablation of IRP2, consistent with the notion of FBXL5 being a repressor of IRP2[47].

IREs are evolutionarily conserved structural motifs present in mRNAs within the untranslated regions (UTRs). IRPs bound to IREs in the 5' UTR obstructs translation while in the 3'UTR stabilizes the mRNA. IREs are stem–loop structures which consist of 25–30 nucleotides[48]. A major regulation of cellular iron status occurs via the IRE-IRP-mediated post-transcriptional regulation of transferrin receptor (TfR1) mRNA which contains multiple IREs within its long 3′ UTR. Ferritin FTH1 and FTL mRNAs contain a single IRE in the 5' UTR and is also regulated by IRP interaction under various cellular iron conditions.

In iron-deficient conditions, IRPs bind to IREs on the *TfR1* mRNA with high affinities (Kd $\approx 10^{-12}$ M). On the *TfR1* mRNA, IRP binding leads to enhanced stability of the mRNA. On the contrary, IRP-IRE interaction on ferritin mRNA leads to translational inhibition of the mRNA. TfR1 protein therefore accumulates, enhancing the cellular uptake of iron from circulating Tfn. Ferritin production decreases, preventing iron storage and accumulation, promoting iron utilization. In iron overload conditions, IRPs do not bind to IREs, resulting in decreased TfR1

production and increased ferritin production. This minimizes cellular iron uptake by TfR1 and induces iron storage by cellular ferritin[45]. Certain mRNAs encoding iron metabolism proteins such as DMT1 and Fpn exists as both IRE and non-IRE isoforms. The expression of the IRE or non-IRE isoform is dependent on tissue and cellular specificity. For example, in duodenal enterocytes and erythroid precursor cells, Fpn exists predominantly as the non-IRE isoform[49]. Expression of the non-IRE isoform reduces the occurrence of IRP-IRE interactions and allows for efficient iron transport in these cell types during iron-deficiency.

Iron-deficiency and inflammation

Iron-deficiency has long been known as a consequence of the inflammatory stress response and used by the body as a strategy to confer resistance to infection. This association is best described by anemia of inflammation, also known as the anemia of chronic disease (ACD). ACD is characterized as hypoferremia, low plasma iron-binding capacity and normal-to-elevated ferritin levels. The reduction in iron availability can be largely attributed to the hepcidin-ferroportin iron regulation axis through upregulation of hepcidin. The response can be reproduced in mice by the overexpression of hepcidin[50]. Hepcidin is produced in the liver in response to the inflammatory cytokine interleukin-6 (IL-6)[51] and can also be produced by immune cells such as macrophages upon stimulation through a toll-like receptor-4 (TLR-4) dependent pathway[52,53]. It has also been shown that other cytokines such as IL-1β can induce hepcidin production[54]. While hepcidin is a major regulator of iron during inflammation, it is noteworthy to mention that other pathways also contribute to the inflammatory response which regulates systemic iron. One example is the cytokine-

mediated effects elicited by tumor necrosis factor-α (TNF-α) and interferon-γ (IFN-γ)[55].

Both TNF-α and IFN-γ are pro-inflammatory cytokines that function to modulate iron status independent of the induction of hepcidin. Increased TNF-α levels promotes hypoferremia[56] and are associated with systemic iron-deficiency in humans[57]. TNF-α treatment in mice leads to a decrease in intestinal iron absorption[58], speculated to hence cause iron-deficiency. IFN-γ modulates the innate immune response through the stimulation of nitric oxide (NO) synthesis, catalyzed by the iron-regulated inducible NO synthase (*iNOS*). Iron inhibits IFN-γ, resulting in an inverse relationship between cellular iron status and *iNOS* expression[59]. *In vivo* studies show that a high-iron diet suppresses IFN-γ production[60], suggesting that iron loading represses the systemic inflammatory response.

Erythroid lineage development

Steady state erythropoiesis

Definitive erythropoiesis in adult mammals occurs predominantly in the bone marrow and arises from hematopoietic stem cells (HSCs) derived from pluripotent stem cells within the tissue. HSCs then give rise to the first erythroid lineage-committed progenitor cells known as the burst-forming unit-erythroid (BFU-E). Slow proliferating BFU-Es then divide and differentiate into colony-forming unit-erythroid (CFU-E). Subsequently, CFU-Es divide rapidly over the span of 2-3 days and undergo major cellular changes to become erythroblasts[61]. The proliferation and differentiation of CFU-Es to erythroblasts is controlled by the cytokine, erythropoietin (EPO). EPO, produced by the kidney and induced under hypoxic

conditions, provides the extracellular stimulus for CFU-E differentiation. EPO binds to the EPO receptor on the surface of erythroblast progenitors, resulting in a signaling cascade that induces differentiation. EPO appears to function during CFU-E differentiation through multiple pathways, including the signal transducer and activator of transcription 5 (Stat5) and phosphoinositide-3 kinase/Akt (PI3K/Akt) pathways[62,63]. Defects in either of the two pathways result in erythroid progenitor cell death and reduction in erythropoietic output. Post-CFU-E differentiation, erythroid maturation continues with erythroblast development within the bone marrow niche. The earliest erythroblast stage is called the proerythroblast, which undergoes proliferation and differentiation to give rise to four consecutive stages of erythroblasts. The order of maturation occurs from proerythroblast to basophilic, polychromatic and orthochromatic erythroblasts. Orthochromatic erythroblasts then undergo nuclear expulsion to become reticulocytes, which are the terminal stage of differentiation before erythrocytes are released into circulation. Each distinct stage of erythroblast maturation is distinguished by cell size and membrane protein composition. The differentiation of erythroblasts is also accompanied by enhanced chromatin condensation and progressive hemoglobinization. Two common cell surface membrane proteins used to distinguish erythroblastic stages are transferrin receptor 1/CD71 and CD44, an adhesion molecule. Both proteins are expressed at high levels in developing erythroblasts but not expressed on mature erythrocytes. As different stages of maturing erythroblasts express different levels of CD71 and CD44, these markers are used in conjunction with Ter-119, an erythroid-specific cell surface glycophorin A expressed by all cells within the erythroid lineage. The maturation of

erythroblasts coincides with the increase in hemoglobin production, and expression of the EPO receptor, TfR1, ALAS2 and globin at varying time points **(Fig. 1.2)**. Using flow cytometry, the combination of Ter-119, CD71 or CD44 and cellular size allows for the identification of specific stages of developing erythroblasts[64].

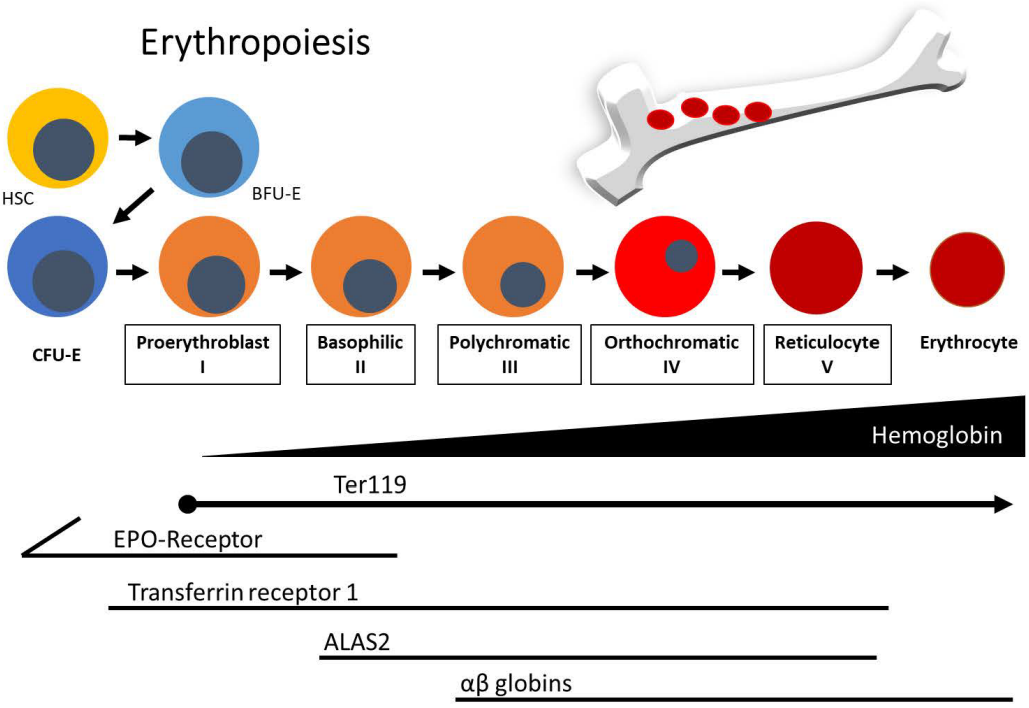

Figure 1.2 Erythroblast maturation

Hematopoietic stem cells (HSCs) give rise to burst-forming unit-erythroid (BFU-E) which matures into colony-forming unit-erythroid (CFU-E). The erythroid lineage continues by maturation into proerythroblast, then basophilic, polychromatic, orthochromatic, reticulocyte and terminal differentiation into erythrocytes. The maturation occurs with hemoglobin formation and expression of Ter119, EPO-receptor, transferrin receptor 1, ALAS2 and globins production.

Extramedullary erythropoiesis

Steady state erythropoiesis, mostly occurring in the bone marrow, produces new erythrocytes at a constant rate. In contrast, stress or extramedullary erythropoiesis, observed in mice spleens and livers, is capable of generating large numbers of erythrocytes rapidly[65]. It was recently observed that erythroblastic islands

(EBIs) also facilitate stress erythropoiesis in the spleens of mice, although the process utilizes stress erythroid progenitor (SEPs) cells that are distinct from the steady state erythroid progenitors in the bone marrow[65,66]. Furthermore, stress-induced EBIs in the spleen contain nurse macrophages derived from recruited circulating monocytes. These monocytes, together with SEPs, develop into stress-induced EBIs to support extramedullary erythropoiesis[66].

Stress erythropoiesis is induced during anemia as anemia induces tissue hypoxia, which in turn causes the transcriptional activation of EPO in the kidney. The 3'-flanking region of the EPO gene contains a hypoxia-inducible enhancer, which is the target of the transcription factor hypoxia-inducible factor 1 (*HIF-1*)[67]. While EPO plays a significant role in the expansion and terminal differentiation of bone marrow erythroid progenitors during stress erythropoiesis[68], the expansion of erythroid progenitors in the spleen also relies on other key signals including *BMP4*, which induces the expansion of BFU-E in the spleen to promote recovery from acute anemia[65]. It is noteworthy that hypoxia also regulates the induction of *BMP4* expression in the spleen[69] and is required for the maximal stress response of SEPs to BMP4[70]. The *BMP4* gene contains two hypoxia responsive elements that regulate gene expression through the transcription factor hypoxia-inducible factor-2α (HIF-2 α)[65].

Iron metabolism during erythropoiesis

Erythroid differentiation is accompanied by high levels of hemoglobin synthesis. This relies on an efficient pathway to uptake extracellular iron to provide iron for heme synthesis. Therefore, erythroblasts express high levels of CD71, or the

transferrin receptor 1 (TfR1), which binds circulating iron-bound transferrin at high affinities. One transferrin molecule binds two ferric iron atoms with an association coefficient of 10^{-20} M at physiological pH and is referred to as holo-Tf[71]. When bound, the holo-Tf-TfR1 complex undergoes receptor-mediated endocytosis, resulting in internalization and subsequent release of ferric iron upon endosomal acidification. Six-transmembrane epithelial antigen of prostate 3 reductase (STEAP3)[72] catalyzes the reduction of Fe^{3+} into Fe^{2+} which is transported out of the endosome by divalent metal transporter 1 (*DMT1/NRAMP2/SLC11A2*)[73]. After iron-release, the apo-Tf-TfR1 complex is transported back to the cell surface, and apo-Tf dissociates from TfR1 and re-enters the circulation. The Tf-TfR1-mediated iron transport cycle ensures that developing erythroblasts optimize iron uptake from the circulation to sustain maximal hemoglobin production.

Iron transport into mitochondria for heme synthesis is mediated by *SLC25A37* (mitoferrin1/*MFRN1*), a protein in the family of mitochondrial solute carrier proteins. *MFRN1* is expressed in the inner mitochondrial membrane and transports iron across mitochondrial membranes[74]. Zebrafish with *MFRN1* defects have significant hypochromic anemia and display erythroid maturation arrest due to insufficient mitochondrial iron uptake in erythroblasts. In yeast, the deletion of two *MFRN* homologs, *Mrs3* and *Mrs4* impairs incorporation of iron into PPIX and formation of Fe-S cluster assembly leading to poor growth under low iron conditions. *MFRN1* deletion in mice causes embryonic lethality and mouse erythroblasts obtained from *MFRN1*-deficient embryonic stem cells are unable to incorporate iron into heme during mitochondrial heme synthesis. Mice with targeted deletion of *MFRN1* in adult

hematopoietic tissues are unable to support erythroblast maturation and are severely anemic[75].

Heme synthesis in erythroid cells

Erythroid heme synthesis contains unique regulatory mechanisms to ensure sufficient production of heme for hemoglobinization of developing erythroblasts. Heme synthesis precedes globin synthesis during erythroblastic differentiation due to the requirement of heme as a signaling factor in activating protein translation initiation. In the presence of sufficient cellular heme, heme binds and inactivates the heme-regulated eukaryotic initiation factor2α kinase (*HRI*), allowing protein synthesis to occur[76]. While the heme biosynthetic pathway in erythroid cells is largely similar as that in other eukaryotic cells, erythroid cells utilize an erythroid-specific isoform of ALAS called ALAS2 to catalyze the rate-limiting step of ALA synthesis[77]. Activation of *ALAS2* is controlled by the erythropoietic regulator and transcription factor GATA1. The gene encoding *ALAS2* contains two *GATA1* binding elements, one in the first and in the eighth intron[78,79]. Removal of the *GATA1* binding elements prevents *ALAS2* expression and inhibits downstream heme biosynthesis, but can be overcome by supplementing cells with ALA, the product of *ALAS2*. *ALAS2* is also regulated post-transcriptionally, via IREs in the 5' UTR[80]. In iron-deficiency, *ALAS2* translation is inhibited by IRP-IRE binding while the converse occurs when iron levels are sufficient. The tight regulation of *ALAS2* expression in erythroid cells is concomitant with cellular iron and heme levels. Due to the erythroid specificity of *ALAS2*, defects in *ALAS2* results in disorders including X-linked sideroblastic anemia

and X-linked protoporphyria[76]. These disorders result in anemia as erythroid cells are poorly hemoglobinized.

The last step of heme biosynthesis catalyzed by *FECH* is also uniquely regulated in erythroid cells. For example, in the promoter region of the gene encoding *FECH*, both housekeeping and distinct erythroid elements exist[81]. Like *ALAS2*, *FECH* transcription is also regulated by *GATA1* and *FECH* is highly induced during terminal erythroid differentiation[82]. It has also been reported that alternate splicing in the 3' noncoding region of *FECH* mRNA occurs specifically in erythroid cells[83]. A deficiency in *FECH* leads to erythropoietic protoporphyria (EPP)[84], where PPIX accumulates in erythrocytes, skin and liver of patients. PPIX accumulation manifests clinically as photocutaneous sensitivity and possibly liver disease[76].

In addition to the regulation of heme synthesis, globin synthesis in erythroid cells is also an important factor during hemoglobinization. Globin synthesis is regulated by heme via the *BACH1* (BTB and CNC homology 1) transcription factor[85]. The coupling of heme synthesis and globin production ensures that sufficient globin is produced to meet the heme levels produced during erythroid differentiation.

Macrophages in erythropoiesis

Terminal erythropoiesis in the bone marrow has been observed to take place in a specialized microenvironment called the erythroblastic island. The erythroblastic island (EBI) was first observed in bone marrow sections using transmission electron microscopy in 1958[86]. EBIs were characterized as a compound structure containing a central macrophage surrounded by developing erythroblasts[86]. Although the interactions between the central "nurse" macrophage and surrounding erythroblasts

are still not well understood, it has been shown that nurse macrophages promote erythropoiesis by supplying iron to developing erythroblasts and stimulating the proliferation and survival of erythroblasts. In the absence of transferrin, *in vitro* cultures of macrophages were observed to secrete ferritin that were subsequently endocytosed by developing erythroblasts and used as a source of iron for heme production[87]. Furthermore, developing erythroblasts co-cultured and adhered to macrophages *in vitro* showed enhanced proliferation compared to erythroblasts cultured alone[88]. In addition to supporting the maturation and growth of developing erythroblasts, nurse macrophages also assist in the terminal maturation of a proerythroblast into a reticulocyte through phagocytosis of the expelled nuclei, known as a pyrenocyte[89]. Prior to phagocytosis, adhesion molecules including Emp[90] and β1 integrin[91] expressed on the pyrenocyte facilitates retention of the pyrenocyte on the nurse macrophage surface. Emp-null mice fetuses die *in utero* and show a significant increase in the number of nucleated erythrocytes in the peripheral blood[90]. Nurse macrophages then degrade the phagocytosed nuclei using DNase II. *DNase II*-deficient fetuses are incapable of supporting definitive erythropoiesis and contain fetal liver macrophages with ingested nuclei. They subsequently suffer from severe anemia leading to death *in utero*[92].

The macrophage-erythroblast interactions within EBIs also potentially involve the transport of heme. While the transfer of heme from erythroblasts to macrophages has not been shown, the cellular heme exporter *FLVCR1a/b* appears to be essential for erythroid maturation. *FLVCR1a*-deficient mice are unable to develop definitive erythropoiesis and develop a severe macrocytic anemia with proerythroblast

maturation arrest[93]. *FLVCR1b*, the mitochondrial isoform, is required for erythropoiesis through mitochondrial heme efflux into the cytoplasm. In the absence of *FLVCR1b*, erythroid differentiation is also terminated[94]. It thus appears that erythroid precursors require heme export at both the mitochondrial and cellular level to regulate erythroid differentiation and to prevent excess intracellular heme accumulation and toxicity.

Macrophage heme-iron recycling and transport

The lifespan of erythrocytes in humans is about 120 days and each day, 20–25 mg of iron flows through the hemoglobin cycle. Hence over 2.5 million erythrocytes are removed and replaced by new ones each day. Macrophages in the spleen, liver and bone marrow are central to the removal of damaged or senescent erythrocytes known as erythrophagocytosis. This process is important for the extraction of heme and eventually iron from erythrocytes[95].

As erythrocytes enter the spleen through blood circulation, they encounter macrophage receptors in the red pulp searching for the display of surface markers or antibodies that stimulate phagocytosis. Cellular changes by erythrocyte senescence must reach a specific threshold that causes recognition by splenic red pulp macrophages (RPMs) and induce erythrophagocytosis (EP) **(Figs. 1.1, 1.2)**.

A variation of cellular alterations on the erythrocyte membrane may lead to RPM erythrophagocytosis. One modification of aging occurs to Band 3, a chloride-bicarbonate exchanger abundantly found on the erythrocyte membrane. As erythrocytes age, Band 3 membrane clustering occurs and is recognized as a marker of senescence by macrophages. Band 3 protein clustering is a consequence of the

binding of denatured hemoglobin to its cytoplasmic domain and may be induced by proteolytic cleavage or covalent modifications as erythrocyte age[96]. Band 3 clusters are recognized by opsonic natural antibodies and complement-triggering conventional antibody leading to complement-mediated phagocytosis by macrophages[97]. Phosphatidylserine (PS), normally found on the inner leaflet of the RBC membrane, is increasingly exposed as RBCs age and PS exposure correlates with RBC clearance[98,99]. Erythrocyte senescence may also be accompanied by increased membrane rigidity and the loss of sialic acid and the CD47 antigen[100].

RPMs in the spleen are the main subtype of resident macrophages that phagocytose RBCs. The development of RPMs, characterized as $F4/80^{hi}TremL4^{+}CD11b^{lo}$ cells, is dependent on the transcription factor *SPIC*. *SPIC* transcription is regulated by the transcriptional repressor *BACH1*, which is inhibited by heme binding on a dipeptide motif of cysteine and proline[101]. *BACH1*, a member of the basic leucine zipper family of transcription factors, forms heterodimers with small Maf proteins to control gene expression[102]. *BACH*–Maf heterodimers bind to Maf recognition elements (MARE) and suppresses gene expression of target genes such as Fpn[102]. When heme binds to BACH1, its DNA binding is altered thus inducing nuclear export of BACH1 and its subsequent ubiquitination and degradation[103-105]. In the splenic red pulp, heme induces degradation of BACH1 protein in monocytes, leading to de-repression of *SPIC* and inducing the maturation of monocytes into RPMs. *SPIC*-deficient mice do not have RPMs but are normal for other resident macrophage subtypes within the spleen. *SPIC*-deficient mice have a

reduced capacity to recycle iron through erythrocyte recycling and accumulate iron in their spleens[106].

When RPMs engulf senescent or damaged RBCs, divalent metal transporter *NRAMP1* (natural resistance-associated macrophage protein 1) and heme transporter *HRG1/SLC48A1* (heme-responsive gene 1) are recruited to the phagosomal membrane[107]**(Fig. 1.2)**. NRAMP1 transports iron out of the erythrophagosome and *NRAMP1*-deficient mice exhibit splenic macrophage iron retention when chronically treated with phenylhydrazine, a hemolytic agent[108]. HRG1 transports heme from the phagosomes into the cytosol of bone marrow-derived macrophages (BMDMs) during EP, where heme is subsequently degraded by heme oxygenase 1 (*HMOX1*) to liberate iron[109] **(Fig. 1.2)**. In addition, it has been suggested that cytosolic heme can be transported out of macrophages by FLVCR1[110]. *FLVCR1*-deficient macrophages have elevated ferritin levels following EP suggesting that FLVCR1 may function to export intact heme out of macrophages post-EP[110] **(Fig. 1.2)**. Heme-derived iron is then either stored by cytoplasmic ferritin or exported across the plasma membrane by ferroportin and transported in circulation by transferrin[111] **(Figs. 1.1, 1.2)**. The tightly regulated processes following EP ensure that 1) RBC heme-iron is efficiently recycled for erythropoiesis, and 2) macrophages are protected from potential heme toxicity.

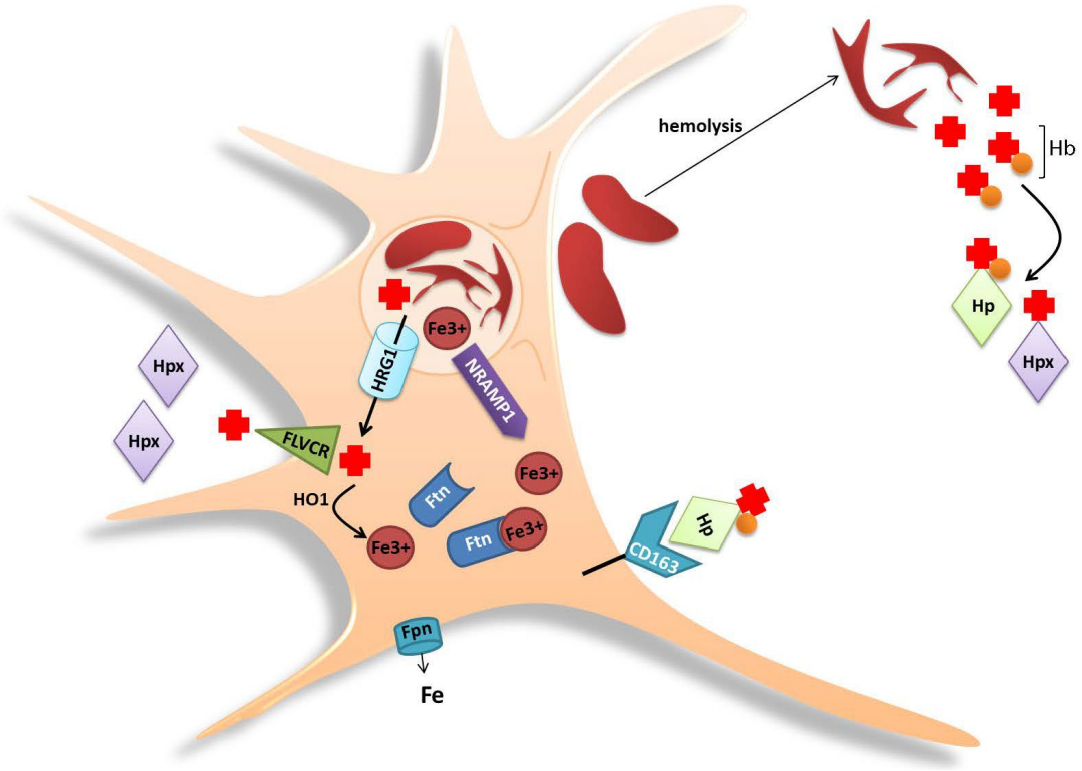

Figure 1.3 Macrophage heme-iron recycling

Reticuloendothelial system (RES) macrophages phagocytose senescent or damaged erythrocytes and recycle heme-iron through an intricate pathway. NRAMP1 transports iron out of the phagolysosome where it can be bound and stored as ferritin iron or exported out of the cell by Fpn. HRG1 transports heme out of the phagolysosome and into the cytosol. Cytosolic heme can be exported by FLVCR1 or catabolized by HMOX1 to release iron. During hemolysis, heme and hemoglobin (Hb) released from erythrocytes are scavenged by hemopexin (Hpx) and haptoglobin (Hp), respectively. RES macrophages express the haptoglobin receptor CD163, which internalizes Hp-Hb complexes.

Secondary systems in mammalian heme handling

In addition to *HMOX1*, which plays a major role in heme catabolism, mammals have also developed secondary systems designed to handle heme and prevent cellular toxicity from exposure to free heme. Haptoglobin (Hp) and hemopexin (Hpx) are two plasma heme scavenging proteins that protect cells from heme-mediated oxidative damage during hemolysis[112].

Hp has the highest binding affinity for hemoglobin (Hb) in plasma and also belongs to the family of acute phase proteins; Hp synthesis is induced by cytokines during inflammation[113]. Haptoglobin (Hp) is synthesized by the liver as a single chain, but subsequently cleaved into an N-terminal light α-chain and a C-terminal heavy β-chain[114]. The two chains associate through an intermolecular disulfide bond between two cysteines[115]. In plasma, Hp binds Hb at a stoichiometric ratio of 1:1 and the complex exists as ferric-Hb-Hp molecules[116]. Hp sequestration of Hb reduces Hb oxidation to release heme and Hp-Hb complexes are endocytosed by tissue resident macrophages in various tissues expressing CD163[117]. Endocytosis of Hp-Hb complexes facilitates the clearance of hemoglobin from the circulation during hemolysis. In addition to macrophages, hepatocytes also endocytose Hp-Hb complexes which subsequently dissociate into Hp and Hb and are individually degraded intracellularly[118].

Hemopexin (Hpx), a 60 kDa glycoprotein found in plasma, consists of a single polypeptide chain (439 aa) with 20% carbohydrate[119]. Hpx, which binds heme non-covalently, has the highest known binding affinity (Kd<1 pM) to heme of any heme-

binding protein[120]. Hpx is made up of two non-disulfide linked, structurally related domains that together bind a single heme molecule. The N-terminal domain can bind heme independently while the C-terminal domain facilitates the binding of Hpx to its receptor[121]. Hpx is mainly produced by liver hepatocytes but has also been observed to be synthesized by neurons of the peripheral nervous system and human retinal photoreceptor and ganglion cells[122-124]. The binding of Hpx to heme in circulation maintains heme in aqueous environments as a soluble monomer[117]. Hpx-heme complexes cause less oxidative damage than free heme and are protective during hemolysis, demonstrating the anti-oxidant properties of Hpx[125]. Hemopexin-deficient mice suffer from severe renal damage and are defective in recovery after acute hemolysis[126]. Hpx-heme complexes are predominantly endocytosed by liver parenchymal cells through the Hpx receptors where heme is released intracellularly from the complex for HMOX-mediated degradation and Hpx is recycled back into the circulation[127].

Heme catabolism and toxicity

Mammals degrade heme into biliverdin, carbon monoxide (CO) and iron via the catalytic activity of heme oxygenases (HMOXs). HMOXs consist of two isozymes, the inducible form *HMOX1* and constitutive form *HMOX2*. *HMOX1* is known to be predominantly expressed in sites such as the liver and spleen[128,129] while *HMOX2* is predominantly expressed in the brain and testis[130]. HMOX1 and HMOX2 are both anchored at their C-termini to the endoplasmic reticulum (ER) by a stretch of ~19 hydrophobic amino acids which forms the transmembrane segment[131]. HMOX1 and HMOX2 are highly homologous in sequence: 45% in total and 59% in the highly

conserved region; the C-terminal membrane anchors contain similarities but are less conserved (~15%)[132]. The degradation of heme by HMOX requires the activity of NADPH-cytochrome P-450 reductase, which is also anchored similarly to the ER membrane[133]. Utilizing three moles of oxygen and seven electrons supplied by NADPH-cytochrome P-450 reductase, HMOX cleaves the alpha-methane bridge of the porphyrin ring of heme to liberate iron and CO with equimolar amounts of biliverdin[134]. Together with NADPH, the cytosolic enzyme biliverdin reductase subsequently converts biliverdin into bilirubin[135]. Intracellular bilirubin is excreted into plasma and transported to the liver by association with serum proteins such as albumin. In the liver, bilirubin undergoes glucuronidation by hepatic phase II UDP-glucuronyltransferases which results in solubilization of bilirubin, preventing its intestinal reuptake. The conjugated bilirubin is then excreted through bile and feces[136].

Heme catabolism by HMOX1 is essential as observed by >90% embryonic lethality of *HMOX1*-deficient mice. Surviving *HMOX1*-null mice suffer from anemia, kidney iron overload and a lack of heme-recycling macrophages[137]. *In vitro*-derived *HMOX1*-null macrophages do not survive the process of erythrophagocytosis, therefore the lack of macrophages *in vivo* is presumed to be an effect of cellular heme toxicity[137]. Free heme is highly toxic and can lead to oxidative stress, hemolytic stress and inflammation[3]. Free heme provides an abundant source of redox-active iron that leads to the production of toxic hydroxyl (•OH) and hydroperoxyl (•OOH) radicals through Fenton reaction[138]. Free heme can also cause protein aggregation, lipid peroxidation, and oxidative DNA damage. For example, hemin has been shown to

increase 13-linoleic acid hydroperoxide-induced lipid oxidation of human erythrocyte ghost, which leads to membrane instability[139]. Hemin also catalyzes the oxidative degradation of proteins[140] and causes DNA damage. Hemin-induced reactive oxygen species (ROS) attacks DNA, causing nicking of supercoiled DNA into open and linear forms and subsequent degradation of the linear DNA[141]. The hydrophobic and lipophilic nature of heme allows it to readily intercalate into cellular membranes and subsequent oxidation of the cell membrane by iron promotes the formation of lipid peroxide leading to cell membrane permeabilization and cell death[3]. The occurrence of this process in RBCs can be highly detrimental and cause hemolysis. Heme intercalation into erythrocyte membranes impairs the maintenance of cellular cation gradients and induces hemolysis by a colloid-osmotic mechanism[142]. Heme-induced hemolysis begins with massive loss of cellular potassium, glutathione and ATP, followed by loss of hemoglobin[142]. Hemin membrane insertion completely disrupts red cell ghosts, impairing lipid and protein associations[143]. Systemically, free hemin promotes inflammation through activation of innate immunity cells and non-hematopoietic cells. Heme induces leukocyte migration along the vasculature by inducing expression of adhesion molecules ICAM-1 (intercellular adhesion molecule 1), VCAM-1 (vascular cell adhesion molecule 1), E-selectin, P-selectin, and von Willebrand factor of endothelial cells[144,145]. Hemin injections into rats caused the activation of neutrophils, resulting in neutrophilic expression of adhesion molecules and subsequent neutrophil migration from intravascular sites to tissue parenchyma[146]. Heme can also act as a chemotactic molecule to cause neutrophil migration[147]. In addition to leukocyte migration, heme also induces pro-inflammatory chemokine IL-8

production by both endothelial cells and neutrophils[146,148]. Heme-induced pro-inflammatory cytokine production is also evident in macrophages. Macrophages are activated by heme and as a result secrete pro-inflammatory molecules such as TNF, KC (keratinocyte-derived chemokine)[149], IL-1β[150] and LTB4 [lipid mediator leukotriene B(4)][151]. These molecules not only activate and attract leukocytes to sites of inflammation, but also regulate cell death and increase vascular endothelial permeability, enhancing the inflammatory response[150].

Heme also induces *HMOX1* expression, which degrades heme and produces anti-oxidants, cytoprotective and anti-inflammatory molecules like CO and bilirubin. HMOX1 is therefore often an acute phase response protein. Bilirubin, an anti-oxidant product of heme degradation, scavenges peroxyl radicals and inhibits lipid peroxidation, conferring protection against inflammation[152]. CO dampens inflammation by inhibiting expression of TNF, IL-1β and macrophage inflammatory protein-1β via a MAPK (mitogen-activated protein kinase) signaling pathway[153]. *HMOX1* induction also stimulates ferritin synthesis, which increases the scavenging of free iron, protecting cells from cytotoxic effects of free iron[154]. As such, HMOX1 is important in mediating anti-inflammatory and protective effects during heme release.

Heme toxicity and detoxification in parasites

Hematophagous parasites (or hemoparasites) such as the malarial parasite *Plasmodium* and digenean *Schistosoma* utilize the host blood as a comprehensive source of nutrients including iron and heme[155]. The adoption of hematophagy to obtain heme is thought to be associated with the evolutionary loss of an endogenous

heme biosynthetic pathway in these parasites[156]. For example, hematophagous nematodes (including *Ancylostoma caninum*, *Haemonchus contortus*, *Ascaris suum*), digenean *Schistosoma mansoni* and the tick *Rhipicephalus microplus* lack enzymatic activities for ALAD, PBGD and FECH, which indicate complete loss of *de novo* heme biosynthesis[156,157]. Other parasites such as the trypanosomatid *Leishmania spp.* have a partially functional heme biosynthetic pathway, with only the last three enzymes of the pathway being present and functional while *Trypanosoma cruzi* and the filariid nematode *Brugia malayi* lack the heme biosynthetic pathway[158,159]. *Plasmodium falciparum* and *Plasmodium berghei*, which live within the host's erythrocytes, have been shown to synthesize heme *de novo* by utilizing host heme biosynthetic enzyme ALAD trafficked from erythrocytes[160]. The trafficked host enzymes contribute to ~80% of the parasite heme biosynthesis, and inhibition of host ALAD trafficking results in the death of intra-erythrocytic *Plasmodium* parasites as it becomes incapable of meeting the requirement for heme-dependent protein synthesis[161]. However, these parasites still largely depend on ingestion of host hemoglobin for heme and iron. Due to the levels of ingested heme, these hemoparasites are constantly exposed to intracellular heme toxicity, necessitating an efficient heme excretion and detoxification pathway. Although some hemoparasites including *Rhodnius prolixus*[163] appear to have *HMOX*-like enzymes that may catabolize ingested heme, some hemoparasites commonly utilize the conversion of heme into an inert crystalline structure called hemozoin to prevent heme toxicity[164]. This detoxification pathway involves the crystallization of α-hematin (ferriprotoporphyrin IX) released during hemoglobin digestion into hemozoin (Hz)

which is chemically identical to β-hematin and has paramagnetic properties[165]. Using multi-frequency high-field electron paramagnetic resonance (HFEPR), Hz was observed to contain five coordinate high spin trivalent Fe^{3+} compounds and within Hz the iron atom is attached by ionic bonds to the four adjacent nitrogen atoms of the porphyrin[166]. While the mechanisms of parasitic *in vivo* Hz formation remain unresolved, it has been shown that heme polymerization into Hz is a chemical process that can occur in the absence of proteins, indicating that it does not have to be an enzyme-mediated process[167]. β-hematin formation in acidic acetate solution is dependent on a moderately low pH (5-6) but spontaneous[168], and the conditions appear to parallel the microenvironment of Hz production *in vivo*. The digestive vacuole of *Plasmodium sp.* in which Hz is formed has a pH ranging from 4.2 to 5.9[169] while the pH of the gut of *Schistoma sp.* where Hz is produced is maintained below pH 5[170].

Although β-hematin can be synthesized *in vitro* to yield the same NMR (nuclear magnetic resonance) and X-ray diffraction as naturally formed Hz, the size and shape of β-hematin crystals are not identical to that of Hz. Natural Hz crystals are typically smaller (50-500 nm) and β-hematin crystals range from 50 nm to 20 μm[164]. The shape and size of Hz crystals also vary between specific *Plasmodium sp*. parasites and other Hz-producing hemoparasites[171], although the basis of this diversity is still unknown.

Problem Statement

Heme-iron recycling by reticuloendothelial macrophages account for ~50% and ~90% of the daily iron requirements in mice and humans[172], respectively, and dietary

heme is more readily absorbed than inorganic iron[11,12]. Consequently, genetic ablations of *HMOX1*, *FLVCR*, *DMT1*, ferroportin, and ferritin in mice have all resulted in partial or complete embryonic lethality, underscoring the importance of heme-iron recycling to systemic iron metabolism. *HRG1* was first identified as a heme transport protein in *C. elegans* and the mammalian homolog was later shown to transport heme across the phagosomal membrane during macrophage heme-iron recycling. Since the *NRAMP1*-deficient mouse does not show any overt deficiencies in heme-iron recycling, the *in vivo* role of *HRG1* and transport of heme derived from erythrophagocytosed RBCs remains an open question. Will the genetic ablation of *HRG1* result in embryonic lethality, similar to the other genes in heme-iron recycling? Does heme transport on the apical surface of enterocytes also mediated by *HRG1*? In this work, we show that a genetic mouse model of *HRG1*-deficiency is incapable of recycling erythrocyte heme-iron and shows high tolerance to heme through the formation of inert crystalline hemozoin. *HRG1*-deficient mice are also abnormal in iron metabolism signaling in response to systemic iron-deficiency, leading to death. Further, we explore whether *HRG1* also functions as an intestinal heme transporter.

Chapter 2 : Materials and Methods

Mouse-related methods

Animals

All mice used were housed in a 12 hour light-dark cycle. Genetic segregation was computed on 21-day old (P21) mice pups. HRG1 mice were genotyped from tail genomic DNA extracts using a custom ordered TaqMan® SNP Genotyping Assays probe (ThermoFisher Scientific) on a Bio-rad CFX Connect system. Mice in all studies were males unless otherwise noted, although initial experiments to exclude gender variation were done using both males and females. All animal protocols were approved by the Institutional Animal Care and Use Committee at the University of Maryland, College Park.

Generation of *HRG1*$^{-/-}$ mice

Guide and Cas9 RNAs: The guide RNA (5'-TAGGGACGGTGGTCTACCGACAACCGG-3') was purchased from Sage Laboratories, St Louis, MO. Cas 9 RNA was purchased from Trilink Biotechnologies, San Diego, CA. The guide RNA and Cas9 RNA were combined at a concentration of 5 ng/µl each in 10 mM Tris, 0.25 mM EDTA (pH 7.5) for injection.

Pronuclear injection was performed using standard procedures[173]. Briefly, fertilized eggs were collected from superovulated C57BL/6J x 129/SvJ F1 females approximately 9 hours after mating with C57BL/6J male mice. Pronuclei were injected with a capillary needle with a 1-2 µm opening pulled with a Sutter P-1000 micropipette puller. The RNAs were injected using a FemtoJet 4i (Eppendorf) with

continuous flow estimated to deposit approximately 2 pl of solution. Injected eggs were surgically transferred to pseudo-pregnant CB6 F1 recipient females. *(The pronuclear injections were conducted by Ms. Lisa Garrett, National Human Genome Research Institute.)*

DNA was obtained from founder (F0) animals by tail biopsy, amplified by PCR (Forward 5'-TGCACCTGTGACTCGGCG-3' Reverse 5'-TAGGTCCCGCCACGTTCATAA-3') and sequenced to determine the mutation. F0 animals carrying mutations were crossed to C57BL/6 animals and the resulting heterozygous F1 animals were either intercrossed to generate homozygous mutant animals or back crossed to C57BL/6 mice for propagation. *(The sequencing of mutants and maintenance of initial colony were conducted by Mr. Will Simmons, National Human Genome Research Institute.)*

Dietary study

HRG1$^{+/+}$ and *HRG1*$^{-/-}$ mice obtained from *HRG1*$^{+/-}$ crosses were weaned at 21 days of age (P21) and placed on their respective diets, supplemented with deionized water. Standard rodent diet was obtained from Envigo and the 2 ppm (TD.09127) Fe diet was custom ordered from Envigo, Madison, WI. Blood was collected by retro-orbital bleeding using microcapillary tubes (Fisher Scientific, cat. number 22-362566). At the end of 5 weeks, mice were sacrificed by cardiac perfusion using Dulbecco's phosphate-buffered saline (DPBS) (Gibco, cat. number 14190250) under anesthesia (10% ketamine, 8% xylazine mix). Prior to perfusion, whole blood was collected into tubes and allowed to clot at room temperature for 45 minutes and serum was separated from the sample by centrifugation at 2,000 g for 10 minutes.

Histology and immunohistochemistry

Paraffin-embedded tissue sections were processed for antigen retrieval by heat-induced epitope retrieval in citrate buffer pH 6 (DAKO, Glostrup, Denmark, cat. number S2367). After epitope retrieval, sections were then incubated with either rat anti-F4/80 (Invitrogen, cat. number MF48000) (1:1000 in blocking buffer TBS with 2% FBS) or rabbit anti-HRG1^{174} (1:500) overnight at 4°C. Polyclonal HRG1 antibody serum was generated in rabbit using the C-terminal 17 amino acid peptide sequence (YAHRYRADFADIILSDF) of human HRG1 as antigen (Epitomics, Inc.). Sections were then incubated with secondary biotinylated anti-rat antibody (Vector labs, cat. number BA-9400) for 30 minutes at room temperature. Signals were detected by DAB substrate incubation and slides were lightly counterstained with hematoxylin.

Crude membrane preps and HRG1 immunoblots

Tissues were snap frozen in liquid nitrogen and ground up using a ceramic pestle and mortar maintained ice-cold. In a dounce homogenizer, ground tissue samples were added to membrane prep buffer (250 mM Sucrose, 1 mM EDTA, 10 mM Tris-HCl pH 7.4, 3X protease inhibitor cocktail). Samples were dounce homogenized until no obvious chunks of tissue were observed and the number of strokes used for homogenization was kept consistent across all samples. Homogenates were centrifuged at 800 g for 10 minutes at 4°C. The supernatant was transferred to ultracentrifugation tubes and spun at 100,000 g for 2 hours at 4°C. The pellet from ultracentrifugation was then resuspended in lysis buffer (150 mM NaCl, 1 mM EDTA, 20 mM Hepes pH 7.4, 2% Triton X-100, 3X protease inhibitor) and

sonicated to ensure complete solubilization. The sample was then centrifuged at 11,000 g for 30 minutes at 4°C and the insoluble pelleted debris was discarded. Protein concentration of the supernatant was determined using the BCA assay (Pierce™ BCA Protein Assay Kit, ThermoFisher Scientific, cat. number 23225). Samples were mixed with Laemmli sample buffer without heating, separated on a 4–20% Criterion™ TGX™ Precast Midi Protein Gel (Bio-rad, cat. number 5671094) and transferred to nitrocellulose membrane. Proteins were cross-linked to membranes by UV treatment and stained by ponceau S before incubation in blocking buffer (5% nonfat dry milk in 0.05% PBS-Tween 20, PBS-T) for 1 hour at room temperature. Blots were then incubated overnight at 4 °C in blocking buffer containing rabbit anti-HRG1 antibody (1:300 dilution). After three washes in PBS-T, blots were incubated 1 hour with horseradish peroxidase (HRP)-conjugated goat anti-rabbit IgG secondary antibody (1:20,000; Invitrogen cat. number 31460) in blocking buffer. Blots were then washed five times with PBS-T and signals were visualized by using enhanced chemiluminescence (SuperSignal West Pico, Pierce) and detected using ChemiDoc™ Imaging Systems (Bio-rad).

RNA extraction and quantitative reverse-transcriptase PCR

Total RNA was isolated from samples using TRIzol™ Reagent (ThermoFisher Scientific). cDNA synthesis was done using RT2 First Strand Kit (Qiagen). The Qiagen iron metabolism RT2 profiler array (cat. number 25204D) was custom built and used with RT2 SYBR Green Fluor qPCR mastermix (Qiagen) on a CFX Connect system (Bio-rad). Analysis of gene expression data was conducted using the online data analysis web portal provided by Qiagen. Briefly, Ct values for

each gene in each group (eg. +/+, Standard diet) were obtained by taking the average across all mice (n=9 per group). ΔCt values were then obtained by the following formula: ΔCt = Ct (target gene) – Ct (housekeeping gene). The housekeeping gene used was Rpl13a. Gene expression was then calculated by the formula 2^(- ΔCt). p-values for gene expression were calculated using ΔCt values, the corresponding standard deviations and n=9. The gene expression heatmap was generated by the Heatmapper software and clustering was performed using Pearson's distance measurement method with average clustering[175].

X-ray fluorescence microscopy

Sample preparation was performed as described previously[176]. Briefly, macrophages were cultured directly onto sterilized silicon nitride membranes (1.5 x 1.5 mm, SiN, Silson Ltd, Northhampton, England) that had been incubated with sterile 0.01% Poly-L-lysine solution (Sigma-Aldrich, St Louis, MO). For the XFM experiments, the cells on the SiN membranes were fixed with 4% paraformaldehyde (PFA), rinsed sequentially with PBS, isotonic 100 mM ammonium acetate, DI water and air-dried.

XFM data were collected on the Bionanoprobe[177], beamline 9-ID-B, at the Advanced Photon Source, Argonne National Laboratory, Argonne, IL. The incident X-ray energy was tuned to 10 keV using a Si-monochromator, the monochromatic beam was focused to 80 x 80 nm using a Fresnel zone plate. The sample was placed at 15˚ to the incident X-ray beam and the resulting X-ray fluorescence was collected at 90º using an energy dispersive 4-element detector (Vortex ME-4, SII Nanotechnology, Northridge, CA). Elemental maps were generated by extracting,

background subtracting, and fitting the fluorescence counts for each element at each point using the program MAPS[178]. The fluorescent photon counts were translated into μg/cm^2 using calibrated X-ray standards (AXO products, Dresden, Germany). *(The XFM experiments were conducted by Dr. Martina Ralle, Oregon Health Sciences University.)*

X-ray powder diffraction analysis

The powder samples were mounted in a 0.4 mmϕ glass capillary. The X-ray powder diffraction data were measured using a large Debye-Scherrer camera with an imaging-plate as a detector installed at SPring-8 BL02B2[179]. The wavelength of incident X-ray was 0.800 Å. The exposure time was 17min. The X-ray powder diffraction patterns were collected in 0.01° steps in 2θ. The data range of the present analysis was from 2.0° to 30.0° in 2θ, which corresponds to more than 1.55 Å in d-spacing range. Peak positions and relative intensities of powder profile were similar to those of β-hematin[180]. The rigid-body Rietveld analysis was carried out as an initial stage of refinement using the program SP[181]. The reliability factors of final Rietveld refinement were R_{wp}=2.6% and R_I=5.7%, respectively. *(The X-ray diffraction analyses were conducted by Dr. Hiroshi Sugimoto, RIKEN, Spring-8, Japan.)*

Inductively coupled plasma mass spectrometry (ICP-MS)

Prior to metal and heme analyses, frozen tissues were added to three volumes of pure water and homogenized in ceramic bead tubes (Qiagen) using an Omni Bead Ruptor 24. For metal analysis, homogenate aliquots were digested overnight in 5:1 HNO_3:H_2O_2, dried, and resuspended in 2% HNO_3 for analysis using an Agilent 7900

ICP-MS. Calibration standard solutions for determination of Fe, Zn, Cu & Mn were prepared from Agilent multi-element calibration standard-2A. Protein concentrations of homogenates were determined by BCA Protein Assay (Thermo Fisher Scientific) for normalization. *(The ICP-MS samples were analyzed by Dr. Laurie Jackson, University of Utah.)*

Porphyrin extraction

Enough tissue homogenate preparation for ICP-MS was adjusted with water to make 50 µL of 5 mg/mL protein. The resulting suspension was extracted with 200 µL of EA (a mixture of four volumes of ethyl acetate to one volume glacial acetic acid), centrifuged at 13.5K rpm for 0.5 minutes, and the supernatant was removed. The residual was re-extracted with 200 µL of water-saturated EA and centrifuged similarly. The two supernatants were combined to make about 400 µL total volume, and 10 µL of which was injected into the UPLC. 20 µL of 2xNES (0.2M NaOH, 4% w/v SDS and 6 mM EDTA) added to the ~20µL residual. The resulting suspension was slowly mixed with 280 µL EA and then centrifuged at 13.5K rpm for 10 minutes. 10 µL of the supernatant was injected into the UPLC. In addition, 25 µL of un-extracted homogenate was mixed with 25 µL 2xNES, then with 350 µL EA, centrifuged at 13.5K rpm for 10 minutes and the supernatant was analyzed by UPLC. *(The porphyrin extraction was conducted by Mr. Hector Bergonia, University of Utah.)*

UPLC

About 10 µL of sample extract was injected into a Waters Acquity UPLC system which included a binary solvent manager, sample manager, photodiode array

detector (PDA), fluorescence detector (FLR), column heater and an Acquity UPLC BEH C18, 1.7 µM, 2.1 x 100 mm column. The PDA was set to measure hemin absorbance at 398 nm and the FLR to measure fluorescence of protoporphyrin IX (PPIX) at 404 nm excitation and 630 nm emission. Solvent A was 0.2% aqueous formic acid while Solvent B was 0.2% formic acid in methanol. The flow rate at 0.40 mL per minute at 60˚C for the total run time of 7 minutes. The following successive gradient settings for run time in minutes versus A: 0.0, 80%; 2.5, 1%; 4.5, 1%; 5, 80%. The solvent composition gradient settings were all linear. For standards, solutions of known concentrations of authentic hemin, PPIX dissolved in NES were extracted and then analyzed by UPLC as the samples. *(The UPLC analyses were conducted by Mr. Hector Bergonia, University of Utah.)*

Serum Iron panel

Serum iron, total iron binding capacity (TIBC) and transferrin saturation were measured using the Stanbio Iron & TIBC kit (VWR, cat. number 10152-550). Serum transferrin and ferritin were quantified using the mouse transferrin ELISA kit (Abcam, cat. number ab157724) and mouse ferritin ELISA kit (Abcam, cat. number ab157713). All kits were used according to the manufacturer's protocol.

Serum EPO and Hepcidin

Serum erythropoietin (EPO) was measured using the mouse erythropoietin quantikine ELISA kit (R&D Systems, cat. number MEP00B). Serum hepcidin was measured using the Hepcidin Murine-Compete™ ELISA Kit (Intrinsic Life Sciences, cat. number HMC-001). All kits were used according to the manufacturer's protocol.

^{59}Fe-labelled erythrocytes preparation

^{59}FeCl3 purchased from Perkin Elmer Life Sciences (cat. number NEZ037001MC) was mixed with sodium citrate (1:50 molar ratio in a total volume of 1 mL) and incubated for 1 hour at room temperature to make ^{59}Fe-citrate. To generate ^{59}Fe-labelled RBCs, adult mice were first injected intraperitoneally once per day for 3 consecutive days with 50 mg/kg of phenylhydrazine (Sigma Aldrich, cat. number 114715) to induce anemia. Thirty minutes after the last phenylhydrazine dose, the mice were injected intraperitoneally with 200 µL of radiolabeled ^{59}Fe-citrate (0.03 µM, ~12 million cpm). Following a 3-day rest, the mice were anesthetized (10% Ketamine with 5% Xylazine) and whole blood was collected by retro-orbital bleeding using heparinized tubes. Whole blood was mixed with an equal volume of Alsever's solution (Sigma Aldrich, cat. number A3551). Mice were then sacrificed by cervical dislocation. ^{59}Fe-RBCs were collected by centrifugation, washed with DPBS before counting, and opsonized with the mouse RBC antibody (Rockland, cat. number 210-4139); 20 µL of antibody was used for approximately 10^9 RBCs. The suspension was diluted to 10 mL with PBS, and incubated at 37°C on a rotating table for 20 minutes. The opsonized cells were washed twice with DPBS and counted again.

^{59}Fe-RBC *in vivo* Recycling

Opsonized ^{59}Fe-RBCs were diluted with DPBS and injected intraperitoneally into iron-deficient *HRG1*$^{+/+}$ and *HRG1*$^{-/-}$ mice (250 µl, 860,000 cpm per mouse). ^{59}Fe-RBCs-injected mice provided with food and water were sacrificed by CO_2 asphyxiation at 24 and 96 hours post-injection. Whole blood was collected retro-orbitally for counting prior to sacrifice. Counts for separate tissues and spleen

homogenates were collected on a Perkin Elmer (Packard) Wizard gamma counter and whole carcass counts were collected using a Model 2200 scalar ratemeter (LUDLUM measurements, Inc, Sweetwater, TX).

To count for ^{59}Fe in different extracts in spleens, spleens from the 96-hour time-point were dounce homogenized in lysis buffer (1% Triton X-100, 1% proteinase K, Tris-HCl pH 8.0, 50 mM NaCl, 5 mM $CaCl_2$) and incubated overnight at 37°C. One-third of the homogenate was centrifuged at 11,000 g for 45 minutes to obtain the insoluble fraction. Ethyl acetate (EA) (1 part glacial acetic acid, 4 parts ethyl acetate) was added to the supernatant (1 part supernatant, 4 parts EA). The suspension was vortexed for 1 minute and centrifuged at 800 g for 2 minutes to separate the organic and aqueous phase. This extraction was repeated once to the aqueous layer and EA extracts were pooled for counting.

^{59}Fe gavage and intravenous injection

Prior to ^{59}Fe gavage experiments, mice were fasted overnight but provided with water. Each mouse was gavaged with (volume ~250 µL) 5 µCi ^{59}Fe in a solution containing 0.5 M ascorbate, 0.15 M NaCl and 5 µg $FeSO_4$. For 7 hours post-gavage, mice were provided with only water, with food being provided after the 7 hours. For intravenous (IV) ^{59}Fe injections, each mouse was injected IV through the retro-orbital sinus under anesthesia. The solution injected contains 5 µCi ^{59}Fe in a citrate buffer (pH 6.6) and either 5 µg or 70 µg iron (non-transferrin bound iron experiment). Mice were sacrificed by CO_2 asphyxiation 24 hours post-gavage or IV injections and organs were dissected for ^{59}Fe counting. For bone marrow, one femur and tibia were flushed for counting. Counts were collected on a Perkin Elmer (Packard) Wizard

gamma counter and whole carcass counts were collected using a Model 2200 scalar ratemeter (LUDLUM measurements, Inc, Sweetwater, TX).

In vivo RBC lifespan measurement

RBC lifespan was determined by labeling RBCs with sulfo-NHS-biotin reagent (Pierce, Rockford, IL). Mice were injected intravenously under anesthesia via the retro-orbital sinus with 1 mg of sulfo-NHS-biotin. At different time points post injection, 5 µL of blood was obtained from the tails and resuspended in 300 µl DPBS. The blood samples were stained with Streptavidin, R-Phycoerythrin Conjugate (Invitrogen, cat. number S866) and allophycocyanin (APC)-conjugated Ter-119 (eBioscience, cat. number 47-5921-82) and analyzed by flow cytometry.

In vivo depletion of macrophages

To deplete macrophages in vivo, control of clodronate liposomes (Liposoma, cat. number CP-005-005) were administered intravenously via the retro orbital sinus of mice under anesthesia. A solution of 5 mg/mL clodronate liposomes was used and 0.01 mL/g body weight of liposomes was injected per mouse. Hematocrit was measured on the indicated dates and mice were sacrificed on the indicated days by cardiac perfusion under anesthesia.

Hemozoin extraction and quantification

Hemozoin extraction was performed according to the method of Deroost et al[182]. Approximately 50 to 100 mg perfused mouse liver or spleen were ground in liquid nitrogen with mortar and pestle. The ground powder was resuspended in five to ten volumes of homogenization buffer (50 mM Tris/ HCl pH 8.0, 5 mM $CaCl_2$, 50

mM NaCl, 1% Triton X-100 and 1% Proteinase K) and incubated overnight at 37°C with gentle shaking. For mice younger than three weeks, a whole liver or spleen was homogenized in minimum five volumes of homogenization buffer using FastPrep-24 (MP Bio) for 30 seconds at the 6.5 m/s setting, followed by overnight incubation at 37°C with gentle shaking. The proteinase K digested homogenate was then sonicated (Heat Systems-Ultrasonics, W350) for 1 minute (20 W, pulse 1 sec) and centrifuged at 11,000 g for 45 minute. The supernatant was collected in a new tube (fraction Supernatant) and the pellet was washed three times in washing buffer (100 mM $NaHCO_3$, pH 9.0 and 2% SDS) with 1 minute sonication and 30 minutes centrifugation at 11,000 g. All the supernatant from three wash steps was collected and combined (fraction Washing). The remaining pellet (Hz, fraction Pellet) was dissolved and sonicated for 1 minute in dissolving buffer (100 mM NaOH, 2% SDS and 3 mM EDTA) and centrifuged at 11,000 g for 30 minutes to discard any insolubles. For X-ray powder diffraction analysis, after the third wash, extracted Hz was washed five more times in distilled H_2O to remove the salts and detergents.

Heme concentrations of all three fractions (Supernatant, Washing and Pellet) were determined by pyridine hemochromogen spectra method[183]. A pyridine reagent mix was prepared by adding 3 mL 1 M NaOH and 6 mL pyridine to 19 mL H_2O in a glass container. For oxidized spectrum, 35 µL sample and 17 µL 15 mM $K_3Fe(CN)_6$ was mixed with 1 mL pyridine reagent in a cuvette and the spectrum at 400-675 nm was recorded (Shimadzu, UV-1601). Few crystals (2 – 5 mg) of powdered $Na_2S_2O_4$ were then added to the mixture and the reduced spectrum was recorded at 400-675 nm. Heme concentrations were calculated by subtracting the absorbance readings at

541, 556 and 575 nm in the oxidized spectrum from the corresponding readings in the reduced spectrum to get ΔA540, ΔA556 and ΔA575, using the extinction coefficients 20.7 / mM for ΔA540 ((ΔA556 - ΔA540) / 20.7) and 32.4 / mM for ΔA575 ((ΔA556-ΔA575) / 32.4), multiplying by the dilution factor of the sample (30.06 or (1000 + 35 + 17) / 35) and averaging the two results. Total heme (nmol / mg tissue) in each fraction was calculated by multiplying heme concentration with corresponding fraction volume, and then divided by the weight of homogenized tissue. Total heme (nmol / organ) in each fraction was calculated by multiplying total heme (nmol / mg tissue) with the total weight of corresponding organ. Total heme in the Supernatant and Washing fractions was summed up as non-Hz heme.

Iron-deficient mice

HRG1$^{+/+}$ and *HRG1*$^{-/-}$ mice were placed on the 2 ppm Fe diet post weaning and hematocrit was monitored weekly. The experiment was conducted when the hematocrits of all mice was within 40-75% of their respective starting hematocrits. These iron-deficient mice were used for ^{59}Fe-gavage, *in vivo* recycling and *in vivo* macrophage depletion experiments.

Spleen and bone marrow cells isolation

Mouse spleens were cut up into 1-3 mm pieces and placed in 5 mL of dissociation buffer (RPMI, 1X collagenase B, 1X DNase I) in tubes with a magnetic stir bar. Tubes were placed on a magnetic plate and spleens were dissociated at 37°C for 45 minutes. Homogenates were passed through 70 μm filters and cells were pelleted by centrifugation at 800 g for 10 minutes. Bone marrow cells were flushed from the femur and tibia of mice using a syringe and 18 G needle with 10 mL of

FACS buffer (DPBS with 2% FBS). Cell aggregates were dissociated by pipetting. Cell suspensions were centrifuged at 800 g for 5 minutes and supernatants were discarded. When RBCs were not needed for analysis, cells were resuspended in 1 mL of RBC lysis buffer (150 mM NH_4Cl, 10 mM $NaHCO_3$, 1.3 mM EDTA) and left at room temperature for 3 minutes. The lysis step was quenched by adding 5 mL of RPMI and cells were collected by centrifugation at 800 g for 10 minutes and resuspended in appropriate buffers for downstream application.

Flow cytometry

Prior to staining for flow cytometry, cells were resuspended in FACS buffer and counted to ensure that appropriate amounts of antibodies would be added. Cells were stained in 500 µl FACS buffer with the respective antibodies on ice for 30 minutes. After staining, cells were centrifuged at 800 g for 5 minutes and washed with FACS buffer before being resuspended in FACS buffer for analysis. For erythroid cell populations in the spleen and bone marrow, T cells, B cells, platelets, megakaryocytes and neutrophils were stained with fluorescein isothiocyanate (FITC)-conjugated-CD4 (eBioscience, cat. number 14-0041-86), CD8a (eBioscience, cat. number 14-0081-86), B220 (eBioscience, cat. number 14-0452-86), CD41 (eBioscience, cat. number 14-0411-85), Gr-1 (eBioscience, cat. number 11-5931-82) and CD11b (eBioscience, cat. number 14-0112-86) and dump gating was used to exclude these cell populations during analysis. In addition, cells were stained with antibodies for allophycocyanin (APC)-conjugated Ter-119 (eBioscience, cat. number 47-5921-82) and eFluor-450-conjugated CD44 (eBioscience, cat. number 48-0441-82). For non-erythroid cell analysis, splenic cells were treated with RBC lysis buffer

and stained with the following antibodies: phycoerythrin (PE)-conjugated Treml4 (Biolegend, San Diego, CA, cat. number 143304), APC-conjugated F4/80 (eBioscience, cat. number 17-4801-80), PE-Cyanine7 (PE-Cy7)-conjugated CD11b (eBioscience, cat. number 25-0112-81), brilliant violet 510 (BV510)-conjugated MHC-II (Biolegend, cat. number 107635) and PerCP-Cyanine5.5 (PerCPCy5.5)-conjugated Gr-1 (eBioscience, cat. number 45-5931-80). For all antibodies, 1 µl was used to stain 1 million cells. Samples were run in a FACS Canto II or FACS Aria system (BD) and analysis was performed using FlowJo software (Tree Star Inc., Ashland, OR).

Gating of erythroid populations

The gating strategy for identifying different erythroid populations was as described elsewhere[64], using CD44 as a marker for different populations. Gating strategies are as shown in **Figs. 3.4, 3.5**.

Primary macrophage isolation and culture

To isolate F4/80$^+$ macrophages from splenic and bone marrow cell suspensions, anti-F4/80 microbeads were used in conjunction with LS columns (Miltenyi Biotech, cat. number 130-110-443 and cat. number 130-042-401) according to the manufacturer's protocol. To isolate monocytes from bone marrow suspension, the mouse monocyte isolation kit was used (Miltenyi Biotech, cat. number 130-100-629). For bone marrow-derived macrophages, differentiation of fresh bone marrow cells was carried out in the presence of L929- conditioned media (LCM) as a source of granulocyte/macrophage colony-stimulating factor. Differentiation media composition is as follows: RPMI 1640 (Invitrogen) supplemented with 30% LCM,

20% heat-inactivated fetal bovine serum (FBS, Atlanta Biologicals), 100 U/mL penicillin, 100 μg/mL streptomycin, and 2 mM L-glutamine (Invitrogen). L-929 cells were purchased from the American Type Culture Collection (ATCC). For production of LCM, L-929 cells were grown in the presence of RPMI 1640 supplemented with 10% heat-inactivated FBS, 100 U/mL penicillin, 100 μg/mL streptomycin, and 2 mM L-glutamine for 30 days. Media was collected by sterile filtration and stored at −20°C for later use in BMDM differentiation and culture media.

Immunofluorescence of LAMP1

Bone marrow isolated F4/80+ macrophages (BMMs) were seeded onto coverslips and fixed with 4% PFA pH 7.4 for 40 minutes on ice, then washed twice with DPBS. Quenching was done using 0.1 M ethanolamine for 5 minutes at room temperature, twice. Coverslips were washed twice with DPBS and incubated in a buffer containing DPBS, 3% BSA, 0.4% saponin for 20 minutes at room temperature. Coverslips were then incubated in a buffer containing DPBS, 1% BSA and 0.15% saponin for 10 minutes before incubation with the LAMP1 primary antibody (Developmental Studies Hybridoma Bank, cat. number 1D4B, 1:100 dilution) for 1 hour at room temperature. Cells were then washed three times with DPBS and incubated with the secondary antibody in the same buffer (Invitrogen, cat. number A-2121, 1:2,000 dilution) for 1 hour at room temperature. Coverslips were then washed three times with DPBS and stained with DAPI (1:30,000 dilution of 5mg/mL) for 1 minute before mounting with Pro-long Antifade (Thermofisher, cat. number P36930). Images were taken using the DeltaVision Elite Deconvolution microscope.

Mammalian cell culture methods

Caco-2 cells and heme treatments

All three clones of Caco-2 cells (TC7, Bbe and HTB-37) were a gift from Dr. James Fleet (Purdue University) and maintained in cell culture media containing DMEM, 10% FBS, 100 U/mL penicillin, 100 µg/mL streptomycin, and 2 mM L-glutamine at 37°C supplemented with 5% CO2. For heme treatments, cells were treated with basal media or heme-depleted (HD) media for 24 hours and the indicated heme concentrations were added to HD media. Cells were harvested 24 hours later and lysed with lysis buffer containing 1% Triton X-100 for immunoblotting protein analysis.

Generation of *HRG1*-knockout Caco-2 cells

To generate *HRG1*-knockout Caco-2 cells by CRISPR-Cas9, plasmids containing the guide RNA target sequences of *HRG1* **(APPENDIX I)** (plasmid pSpCas9(BB)-2A-GFP, Addgene; Plasmid #48138) were transfected into unpolarized Caco-2 cells using PolyJet transfection reagent (Signagen, cat. number SL100688). Cells expressing high GFP levels were sorted out using flow cytometry (BD FACS ARIA II) and individual cells were seeded into 96-well plates. Surviving clones were expanded and screened for loss of HRG1 protein by protein immunoblots. Clones confirmed to have loss of HRG1 protein were then genotyped to identify the genetic mutation in the *HRG1* gene locus **(APPENDIX X)**.

HRG1-GFP lentiviral transduction of Caco-2 cells

For lentiviral production of HRG1-GFP, the protocol published by The Broad Institute was used[184]. HEK293T cells maintained in DMEM, 10% FBS, 100 U/mL penicillin, 100 μg/mL streptomycin, and 2 mM L-glutamine at 37°C supplemented with 5% CO2 were first transfected with the lentiviral plasmid expressing HRG1-GFP (Backbone: pLenti CMV/TO eGFP Puro (w159-1), Addgene, plasmid #17481) and packaging plasmids using standard transfection reagent PolyJet (Signagen, cat. number SL100688). Media containing viral particles were collected for a period of three days and centrifuged at 100,000 g to concentrate viral particles. Polybrene was added to media of Caco-2 cells at a concentration of 8 μg/mL and virus was added for infection.

Caco-2 cells polarization

To generate a monolayer of polarized Caco-2 cells, cells were seeded onto cell cultured inserts (Corning, cat. number CLS3412) and allowed to reach confluency. The Caco-2 cell monolayer integrity was checked by measuring the transepithelial electrical resistance (TER) using a Millicell-ERS device (Millipore, Bedford, MA, USA). Monolayers were considered polarized and used for experiments when TER values were in a range of 300–450 Ωcm^2.

Immunofluoresence of Caco-2 cells

Caco-2 cells were fixed with 4% PFA, pH 7.4 for 45 minutes and quenched with 0.1 M ethanolamine for 5 minutes, twice. Permeabilization was done using 0.1% Triton-X 100 in DPBS solution for 10 minutes at room temperature. Blocking was done using 5% BSA in DPBS for 30 minutes at room temperature and E-cadherin

(Abcam, cat. number ab76055, 1:1,000 dilution) or HRG1 antibody was applied to cells in blocking buffer for 1 hour at room temperature. Cells were then washed three times with DPBS and incubated with the secondary antibody in the same buffer for 1 hour at room temperature. Coverslips or transwell membranes were then washed three times with DPBS and stained with DAPI (1:30,000 of 5mg/mL) for 1 minute before mounting with Pro-long Antifade (Thermofisher, cat. number P36930).

RNA extraction and quantitative reverse-transcriptase PCR array

Total RNA was isolated from samples using TRIzol™ Reagent (ThermoFisher Scientific). cDNA synthesis was done using RT2 First Strand Kit (Qiagen). Primers for -*HMOX1* and *β-ACTIN* listed in **APPENDIX II** were used with the RT2 SYBR Green Fluor qPCR mastermix (Qiagen) on a CFX Connect system (Bio-rad). Technical triplicates were ran for each sample and Ct values were normalized to actin.

Pigs methods

Animals

Weanling 21-day old piglets used in dietary study were obtained from Virginia Tech. University Farms and housed in a 12 hour light-dark cycle. Pig diets (iron-deficient, hemin-supplemented and iron-supplemented) were custom purchased from Envigo, Madison, WI. All animal protocols were approved by the Institutional Animal Care and Use Committee at the University of Maryland, College Park.

Dietary study

21 day old weanling piglets were housed and fed with either of the three diets (Hybrid Fe Deficient Weaning Swine Diet TD.150872.PWD, Hybrid Hemin Weaning Diet (75 ppm Fe) TD.150873.PWD, Hybrid FeSO4 Weaning Diet (75 ppm) TD.150874.PWD) and deionized water. Feed intake was *ad libitum* and blood was drawn via the jugular vein weekly and analyzed using the Procyte Dx hematology analyzer (IDEXX). Pigs were euthanized by a penetrating captive bolt to the brain followed by immediate exsanguination. Tissues were collected and snap frozen in liquid nitrogen. Intestinal tissues were collected by scraping of the epithelial layer. *(The pigs were maintained and monitored by Ms. Elda Kwong and Ms. Abisha Dowla, University of Maryland.)*

Immunoblots of pig tissues

Samples were processed in a similar manner as mouse tissues using crude membrane preparation as mentioned previously.

Statistical analyses

All data are shown as means ± SEM unless otherwise stated. Means of groups were compared by using Student's unpaired t test or the equivalent where applicable. A p value of <0.05 was considered statistically significant. Analyses were performed using PRISM 7 software (GraphPad).

Chapter 3 : *HRG1*-deficiency results in a macrophage heme-iron recycling defect

Summary

Cell biological studies in bone marrow derived macrophages have demonstrated that HRG1 transports heme from the endolysosomal lumen into the cytosol post erythrophagocytosis[109]. Here we show that unlike the ablation of other components of the heme-iron recycling pathway, loss of *HRG1* does not result in embryonic lethality but instead have enlarged spleens and darkened RES tissues (spleen, liver, bone marrow). *HRG1*$^{-/-}$ mice exhibit ineffective bone marrow erythropoiesis resulting in a reduced hematocrit and extramedullary splenic erythropoiesis. *In vivo* erythrophagocytosis experiments using ^{59}Fe-labelled RBCs reveal that *HRG1*$^{-/-}$ mice are defective in heme-recycling, which results in heme accumulation in the form of hemozoin in enlarged lysosomes of RES macrophages. Importantly, this hemozoin is not a bioavailable source of heme or iron because liposome-clodronate mediated depletion of macrophages simply redistributed hemozoin by reducing it in the spleen and concurrently accumulating in the liver. These results indicate that formation of mammalian hemozoin is a mechanism of tolerance to cellular heme sequestered in an inert form within a membrane-enclosed intracellular compartment in RES macrophages.

Results

***HRG1*$^{-/-}$ mice are viable but exhibit darkened RES tissues**

HRG1 mutant mice were generated using guide RNAs targeted to exon 1 of *SLC48A1* **(Fig. 3.1A)**, DNA sequencing revealed the mutation to be a two nucleotide deletion in the first exon of *SLC48A1* gene loci encoding HRG1 protein **(Fig. 3.1B)**. The mutation causes a frameshift in the region coding for the first exoplasmic (E1) loop of HRG1 protein **(Fig. 3.1C)**. Although full length *HRG1* mRNA is still detectable **(Fig. 3.1D)**, no HRG1 protein was observed on immunoblots of tissues **(Fig. 3.1E)**. Intercrossing heterozygous (*HRG1*$^{+/-}$) mice revealed expected Mendelian distribution of their progeny **(Fig. 3.1F)**. In adult *HRG1*$^{-/-}$ mice, the major reticuloendothelial system (RES) organs (spleen, liver and bone marrow) were darker in color compared to *HRG1*$^{+/+}$ littermates **(Fig. 3.2A)** and this discoloration continues into old age **(Fig. 3.2B)**. Immunohistochemistry of *HRG1*$^{-/-}$ tissue sections showed no detectable HRG1 protein **(Fig. 3.2C)** together with dark pigments **(Fig. 3.2D)**.

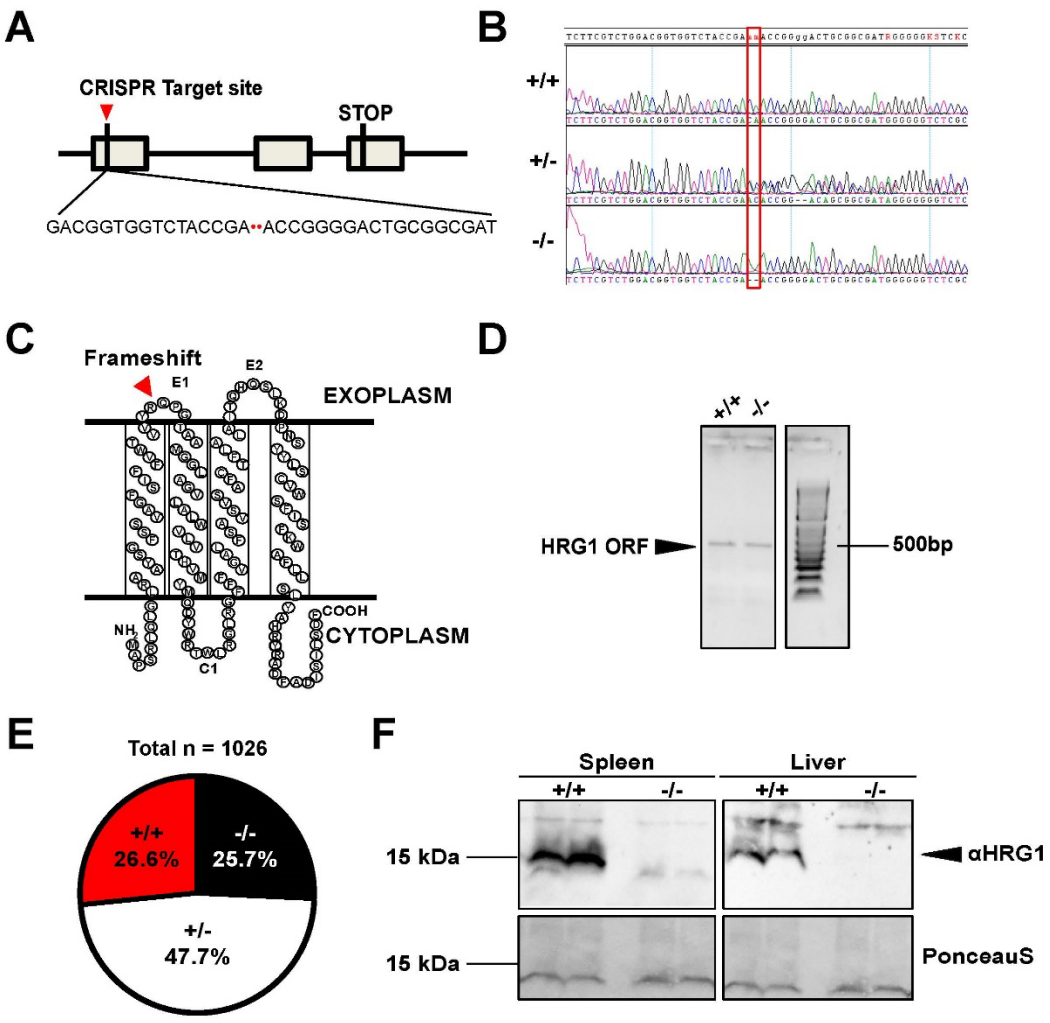

Figure 3.1 Generation of *HRG1*$^{-/-}$ mouse

(A) Gene loci of *HRG1* indicating the CRISPR target site in exon 1 and mutation.

(B) DNA sequence of *HRG1*$^{+/+}$, *HRG1*$^{+/-}$ and *HRG1*$^{-/-}$ mice indicating sequence mutation.

(C) Predicted topology of HRG1 protein; arrow indicates the site of the 2 basepair deletion resulting in frameshift mutation.

(D) Amplification of *HRG1* open reading frame from mouse spleen cDNA.

(E) Mendelian distribution of P21 pups derived from *HRG1*$^{+/-}$ intercrosses.

(F) Immunoblotting analysis of membrane lysates prepared from spleens and livers of mice. Membranes were probed with anti-HRG1 antibody and then incubated with HRP-conjugated anti-rabbit secondary antibody. Each lane represents one animal.

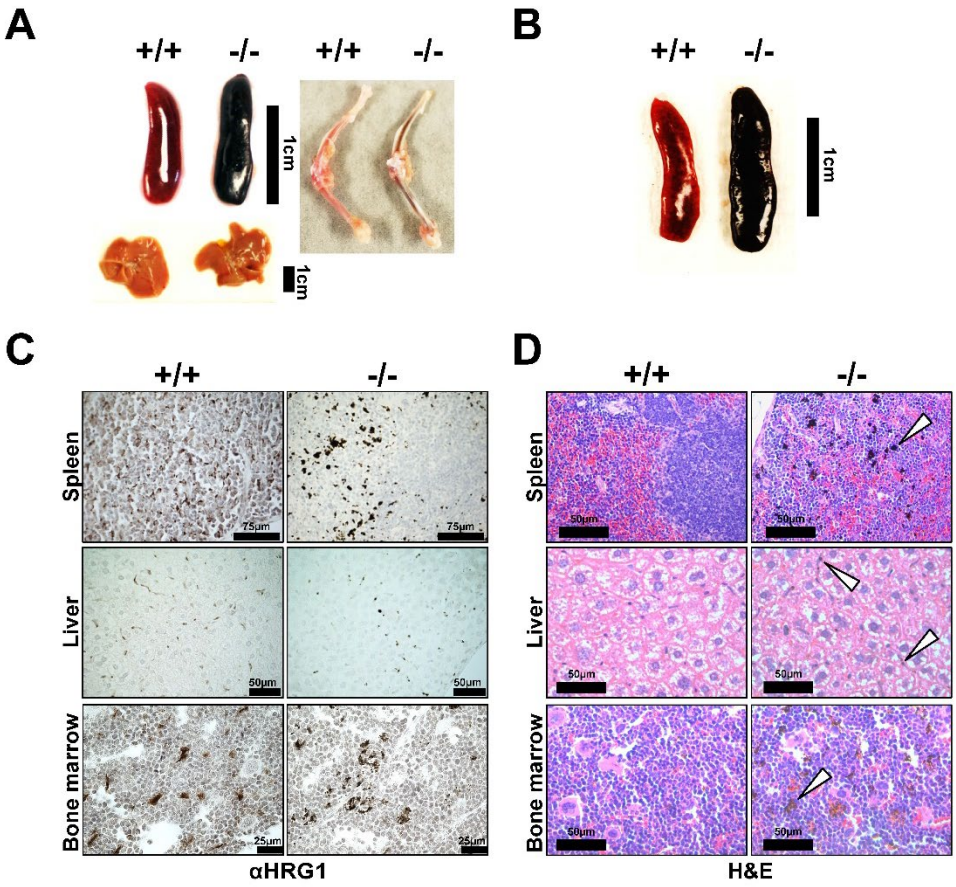

Figure 3.2 *HRG1*$^{-/-}$ RES tissues are discolored and contain dark pigments

(A) Representative images of spleens, livers and bone marrows of 6-week old sex-matched mice.

(B) Representative images of spleens, livers and bone marrows of 12-month old sex-matched mice.

(C) HRG1 immunohistochemistry analysis of paraffin-embedded tissue sections of mice. Tissue sections were probed with affinity-purified anti-HRG1 antibody and then incubated with HRP-conjugated anti-rabbit secondary antibody. Images shown are representative of at least 3 mice.

(D) Histochemical staining of spleen, liver and bone marrow tissue sections of *HRG1*$^{+/+}$ and *HRG1*$^{-/-}$ mice with H&E. Arrows indicate dark pigments in *HRG1*$^{-/-}$ tissues. Images shown are representative of at least 3 mice.

HRG1$^{-/-}$ mice have enlarged spleens and reduced hematocrits

Spleens of adult *HRG1*$^{-/-}$ mice were significantly heavier than *HRG1*$^{+/+}$ spleens with no difference in the total body weights or weights of other organs of these mice **(Fig. 3.3A, B)**. Four-week old *HRG1*$^{-/-}$ mice also exhibited significantly lower whole blood hematocrit levels **(Fig. 3.3C)**. Enlarged spleens and reduced hematocrits were also observed in 24-month old *HRG1*$^{-/-}$ mice but not *HRG1*$^{+/-}$ mice **(Fig. 3.3D-F)**. At nine weeks of age, other hematological parameters of *HRG1*$^{-/-}$ mice were not significantly different from *HRG1*$^{+/+}$ mice **(Table. 3-1)**.

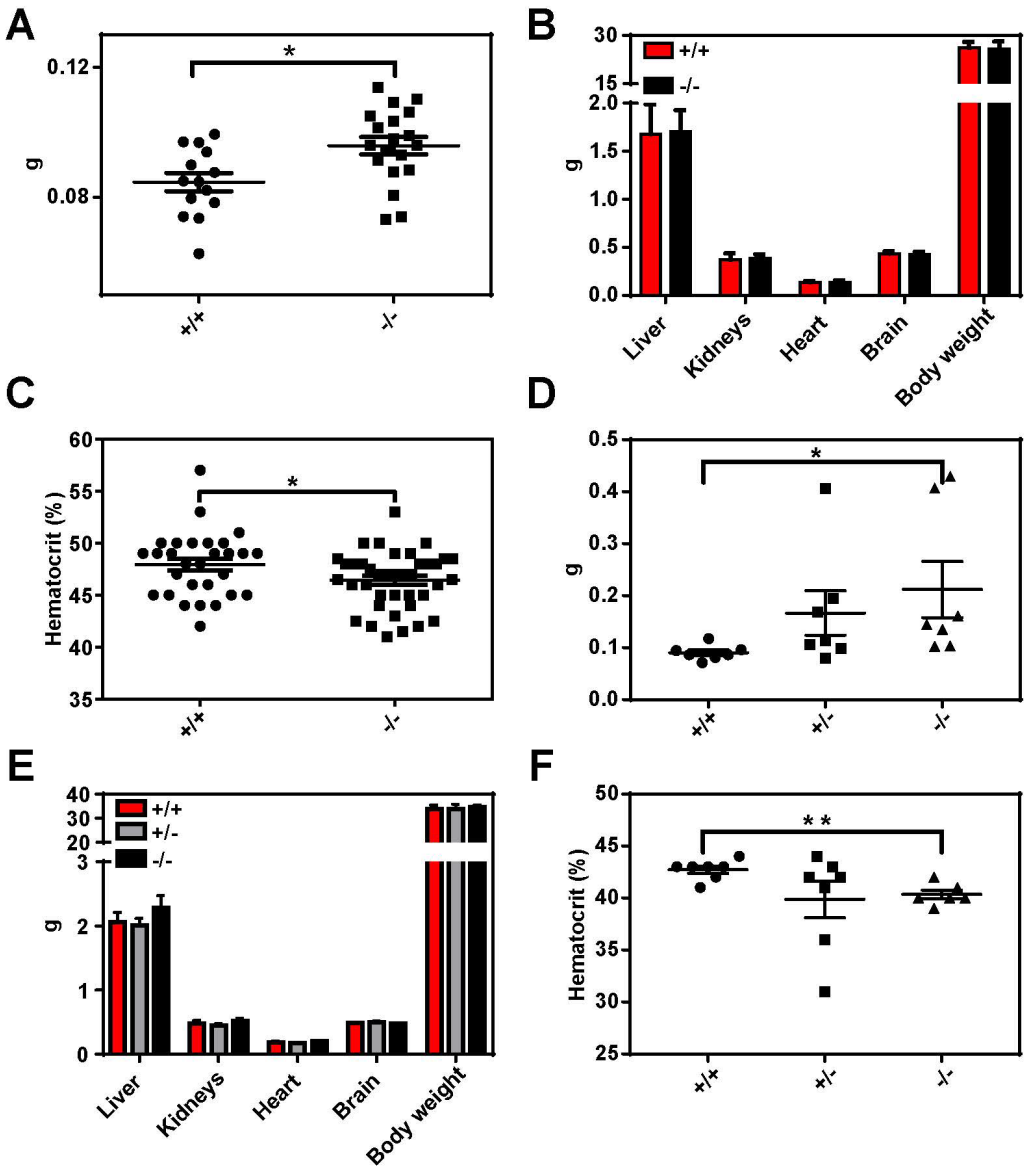

Figure 3.3 *HRG1*$^{-/-}$ mice have enlarged spleens and lower hematocrits

(A) Spleen wet weights from nine-week old *HRG1*$^{+/+}$ and *HRG1*$^{-/-}$ mice.

(B) Wet weights of liver, kidneys, heart, brain and body weights from *HRG1*$^{+/+}$ and *HRG1*$^{-/-}$ mice (n=14-20).

(C) Hematocrits of four-week old *HRG1*$^{+/+}$ and *HRG1*$^{-/-}$ mice.

(D) Spleen wet weights from 24-month old *HRG1*$^{+/+}$, *HRG1*$^{+/-}$ and *HRG1*$^{-/-}$ mice.

(E) Wet weights of liver, kidneys, heart, brain and body weights from *HRG1*$^{+/+}$, *HRG1*$^{+/-}$ and *HRG1*$^{-/-}$ mice (n=6-7).

(F) Hematocrits of 24-month old *HRG1*$^{+/+}$, *HRG1*$^{+/-}$ and *HRG1*$^{-/-}$ mice (n=6). Where applicable, each dot represents one mouse; all mice were age and sex-matched. **p*<0.05; ***p*<0.01.

Table 3-1. Hematological parameters of 10-week old *HRG1*$^{+/+}$ and *HRG1*$^{-/-}$ mice

	Standard diet		**2ppm diet***		**n**
	+/+	-/-	+/+	-/-	
HCT (%)	50.06±1.125[a]	48.81±1.018[a]	32.84±2.227[b]	27.94±2.178[b]	8-15
RBC (M/µL)	10.08±0.2372[a]	9.942±0.1932[a]	8.034±0.5503[b]	6.982±0.557[b]	8-15
MCV (fl)	49.7±0.2252[a]	49.07±0.2831[a]	40.88±0.4719[b]	40.14±0.4421[b]	8-15
RET (%)	4.324±0.2885[a]	4.204±0.1289[a]	3.662±0.7153[b]	4.337±0.6404[b]	8-15
HGB (g/dl)	12.69±0.3232[a]	15.41±1.411[a]	8.52±0.836[b]	8.16±0.9558[b]	8-15
MCH (pg)	14.84±0.1253[a]	14.55±0.08273[a]	13.84±0.4104[b]	14.18±0.475[b]	8-15

*2ppm diet indicates parameters from mice that were fed a low-iron diet for five weeks

Values with different letters are significantly different from each other[a,b]

Ineffective bone marrow erythropoiesis in *HRG1*$^{-/-}$ mice results in extramedullary erythropoiesis

To investigate the erythropoietic compartments, we used Ter-119 and CD44 as erythroblastic cell surface markers[64]. We analyzed the total erythroid compartment as well as different populations of developing erythroblasts via flow cytometry in the bone marrow **(Fig. 3.4A)**. Corresponding to the reduced hematocrits, *HRG1*$^{-/-}$ mice had significantly fewer Ter-119^{+} cells (**Fig. 3.4B)**, and more cells at the basophilic stage **(Fig. 3.4C; population II)**, signifying an impairment in maturation of developing erythroblasts. Similar analyses of erythroid cells in *HRG1*$^{-/-}$ spleens **(Fig. 3.5A)** showed no difference in total Ter-119^{+} population **(Fig. 3.5B)**, but significantly more immature Ter-119^{+} cells present in *HRG1*$^{-/-}$ spleens **(Fig. 3.5C)**, indicating aberrant extramedullary erythropoiesis. This is reminiscent of studies in mice that show ineffective bone marrow erythropoiesis is often accompanied by extramedullary erythropoiesis in the spleen[65] resulting in splenomegaly. The ineffective erythropoiesis is consistent with the lower hematocrit in *HRG1*$^{-/-}$ mice indicative of mild iron-deficiency accompanied by significantly elevated serum transferrin (~1.8 fold; **Table. 3-2**). Full serum iron panel showed comparable levels of serum iron, total iron binding capacity (TIBC), transferrin saturation, EPO, hepcidin, and hemopexin **(Table. 3-2)**, but paradoxically higher levels of serum ferritin (~1.6-fold) in *HRG1*$^{-/-}$ mice.

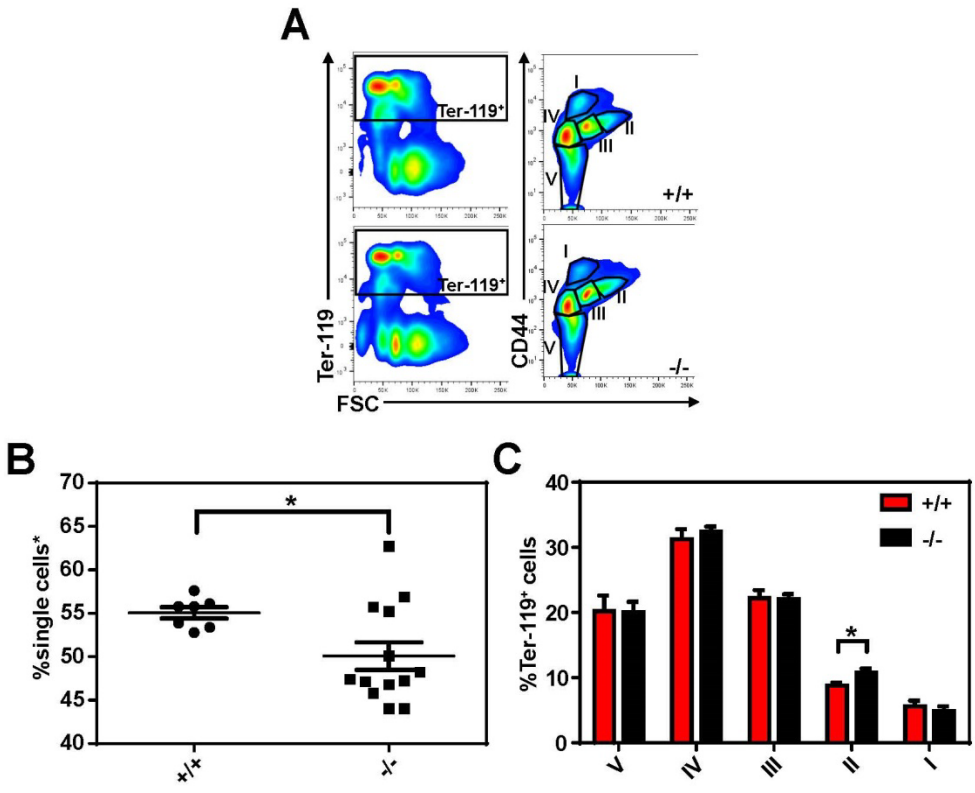

Figure 3.4 Ineffective bone marrow erythropoiesis in *HRG1*$^{-/-}$ mice

(A) Gating strategy of total Ter-119^{+} and Ter-119^{+} subpopulations cells in the bone marrow.

(B) Quantification of total Ter-119^{+} cells represented as a percentage of total single cells* in the bone marrow (n=7-12). The %single cells* on the y-axis denote single cells that are negative for CD4/8/41, B220 and Gr-1.

(C) Quantification of subpopulations of Ter-119^{+} cells represented as a percentage of total Ter-119^{+} cells in the bone marrow (n=7-12). At least 100,000 single cells were analyzed per sample. Where applicable, each dot represents one mouse. *p<0.05.

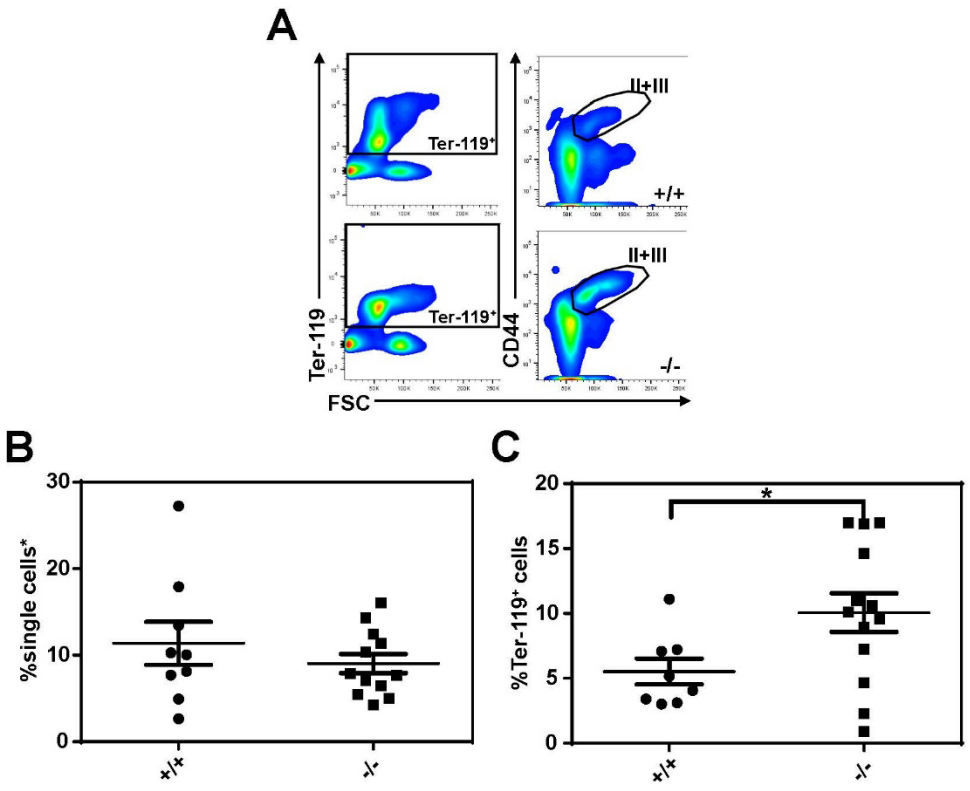

Figure 3.5 *HRG1*$^{-/-}$ mice display extramedullary erythropoiesis

(A) Gating strategy of total Ter-119^{+} and Ter-119^{+} subpopulations cells in the spleen.

(B) Quantification of total Ter-119^{+} cells represented as a percentage of total single cells* in the spleen (n=7-12). The %single cells* on the y-axis denote single cells that are negative for CD4/8/41, B220 and Gr-1.

(C) Quantification of populations II and III of Ter-119^{+} cells represented as a percentage of total Ter-119^{+} cells in the spleen. At least 100,000 single cells were analyzed per sample. Where applicable, each dot represents one mouse. *p<0.05.

Table 3-2. Serum parameters of 10-week old *HRG1*$^{+/+}$ and *HRG1*$^{-/-}$ mice

	Standard diet		n
	+/+	-/-	
Serum Iron (µg/dL)	113.5±11.72	129.3±11.34	8-15
TIBC (µg/dL)	348.4±32.1	341.8±11.62	8-15
Transferrin saturation (%)	36.05±4.452	37.35±2.601	8-15
Ferritin (ng/mL)	369.1±57.02[a]	585.9±58.62[b]	9-15
Transferrin (g/L)	2.796±0.2433[a]	4.996±0.8034[b]	9-15
EPO (pg/mL)	252.8±108.4	168.7±32.05	7-10
Hepcidin (ng/mL)	95.88±6.943	99.79±15.96	5-7
Haptoglobin (mg/mL)	Undetected	Undetected	5-7
Hemopexin (mg/mL)	1.01±0.1317	1.075±0.07541	4-9

Values with different letters are significantly different from each other[a,b]

In vivo* heme-iron recycling is impaired in the absence of *HRG1

Since *HRG1* functions to transports heme from the erythrophagolysosome into the cytosol in macrophages[109] we established an *in vivo* experiment to evaluate red cell recycling defects. We generated ^{59}Fe-labelled erythrocytes that were opsonized and injected intraperitoneally (IP.) into iron-deficient *HRG1*$^{+/+}$ and *HRG1*$^{-/-}$ mice **(Fig. 3.6A)**. The retention and distribution of ^{59}Fe in various tissues were then monitored over time. Injected opsonized erythrocytes enter the circulation and are targeted for erythrophagocytosis in the spleen[108]. Previous reports show that opsonized RBCs are preferentially phagocytosed by RES macrophages and cleared post-i.p. injection[108]. Mice made iron-deficient via dietary iron limitation were used to reduce ferritin-mediated storage of ^{59}Fe within RPMs. At 24 hours post-injection, significantly less ^{59}Fe was detected only in the hearts of *HRG1*$^{-/-}$ mice **(Fig. 3.6B)**, while 48 hours later, there was also no difference in ^{59}Fe retention in all organs measured **(Fig. 3.6C)**. However, 96 hours post-injection, significantly more ^{59}Fe was detected in the spleens of *HRG1*$^{-/-}$ mice while significantly less ^{59}Fe was observed in the carcasses **(Fig. 3.6D)**. Homogenization and high speed centrifugation of splenic tissues followed by differential extraction via organic phase separation revealed a proteinase-resistant insoluble fraction that retained more ^{59}Fe only in *HRG1*$^{-/-}$ samples. Moreover, there was significantly more organic solvent-extractable ^{59}Fe-heme in *HRG1*$^{-/-}$ spleens, but similar levels of inorganic-phase ^{59}Fe in *HRG1*$^{-/-}$ and *HRG1*$^{+/+}$ spleens **(Fig. 3.7A)**. Liver homogenates showed similar trends of ^{59}Fe retention in the various fractions **(Fig. 3.7B)**.

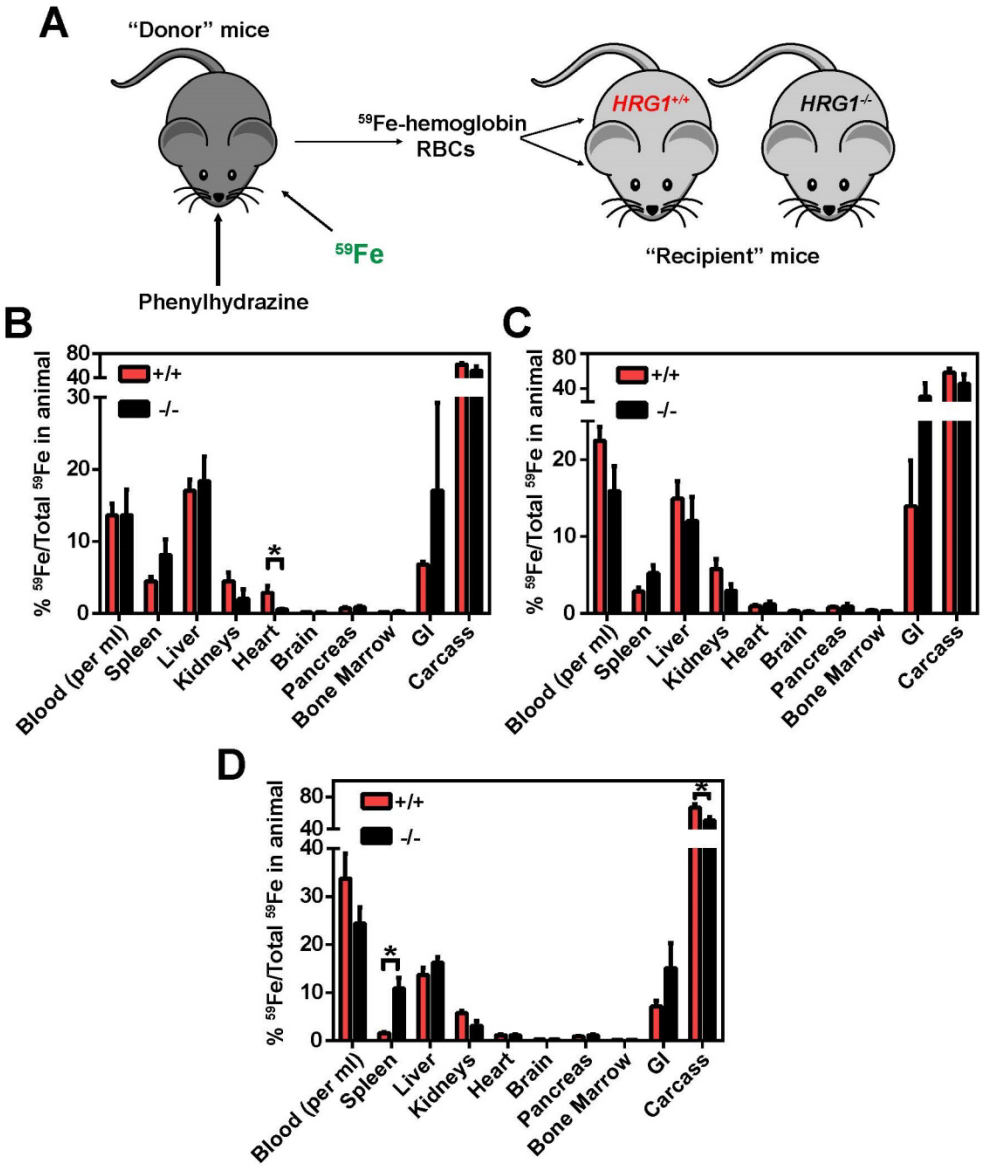

Figure 3.6 *In vivo* recycling of ^{59}Fe-labelled RBCs over 96 hours

(A) Experimental design of ^{59}Fe labeling and in vivo recycling.

(B-D) Quantification of ^{59}Fe retained in tissues, represented as the ratio of the amount of radioactivity within an organ to that of the entire animal at 24, 48 and 96 hours post injection. (n=4-6 across all groups and timepoints). *p<0.05.

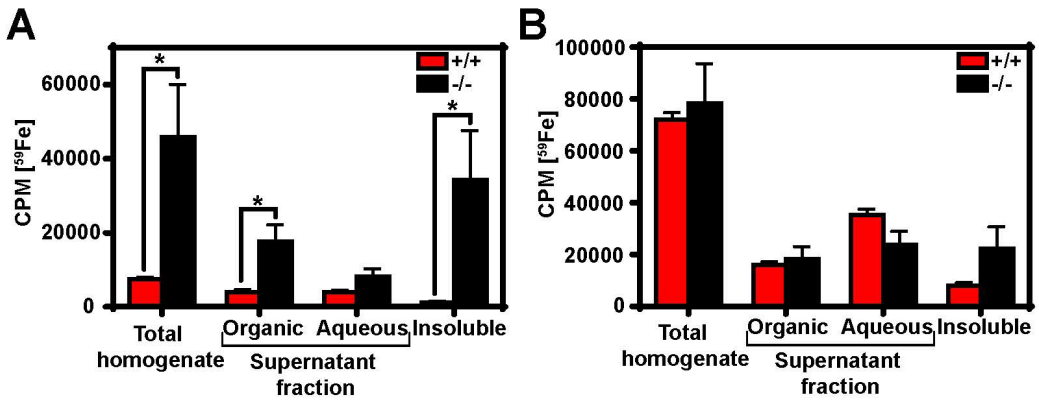

Figure 3.7 Retention of ^{59}Fe in differentially extracted fractions of spleen and liver

(A) Spleen ^{59}Fe retained in differentially extracted fractions at 96 h, represented as counts per minute.

(B) Liver ^{59}Fe retained in differentially extracted fractions at 96 h, represented as counts per minute. Total homogenate: homogenized and proteinase-treated whole spleen; Organic: ethyl acetate extractable ^{59}Fe-heme; Aqueous: ethyl acetate non-extractable ^{59}Fe; Insoluble fraction: proteinase-insoluble fraction containing ^{59}Fe (n=4-6 across all groups and timepoints). *p<0.05.

***HRG1*$^{-/-}$ mice show aberrant tissue metal accumulation**

Although *HRG1*$^{-/-}$ mice had higher serum ferritin levels, an indicator of systemic iron overload **(Table 3-2)**, Perls' Prussian blue staining which detects ferritin-bound iron did not show visible differences between *HRG1*$^{+/+}$ and *HRG1*$^{-/-}$ tissues **(Fig. 3.8)**. As the dark pigments in *HRG1*$^{-/-}$ tissues may mask the blue staining of ferric iron, inductively coupled plasma mass spectrometry (ICP-MS) (in collaboration with Dr. John Phillips, University of Utah) was used to measure total tissue metal content, and ultra-performance liquid chromatography (UPLC) was used to measure heme levels in various tissues of *HRG1*$^{+/+}$ and *HRG1*$^{-/-}$ mice. In RES tissues, *HRG1*$^{-/-}$ mice had consistently more iron (Fe) and heme, with some changes in manganese (Mn) and copper (Cu) levels as well **(Fig. 3.9A-C, E)**. In addition, *HRG1*$^{-/-}$ hearts had dysregulation in the levels of Fe, Cu and zinc (Zn) **(Fig. 3.9A, B, D)**. Surprisingly, *HRG1*$^{-/-}$ mice show significantly lower levels of Fe in the brain **(Fig. 3.9A)**. These analyses were technically performed by Dr. Laurie Jackson and Mr. Hector Bergonia from the University of Utah. In collaboration with Dr. Hiroshi Sugimoto (RIKEN, Spring-8, Japan), dark pigments derived from *HRG1*$^{-/-}$ mice was confirmed to be hemozoin the by powder X-ray diffraction **(APPENDIX III)**. Hemozoin derived from *HRG1*$^{-/-}$ spleen, liver and bone marrow showed differences in morphology when compared to *Plasmodium* hemozoin by scanning electron microscopy (SEM) analysis **(APPENDIX IV).** Extraction of dark insoluble pigments followed by solubilization from *HRG1*$^{-/-}$ RES tissues showed hemozoin accumulation which was not observed in *HRG1*$^{+/+}$ mice **(Fig. 3.10A, B)**.

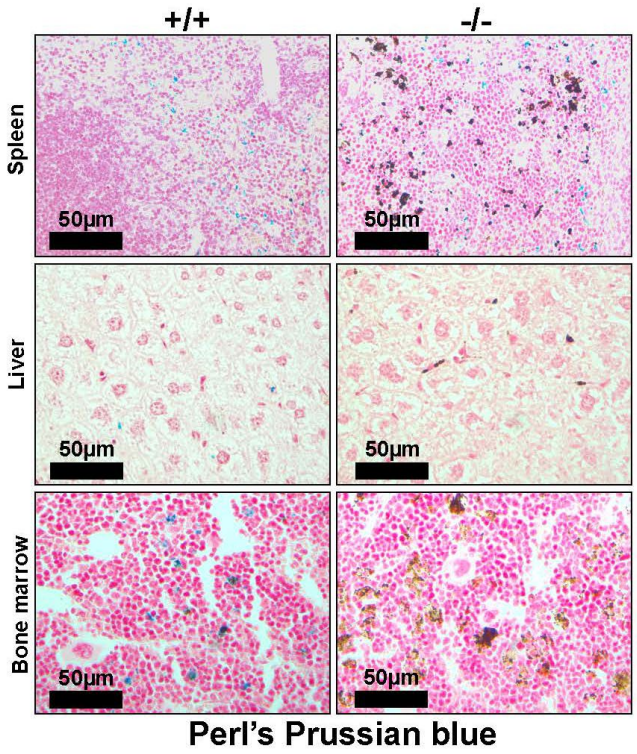

Figure 3.8 Histochemical staining of ferritin-bound iron in RES tissues

Histochemical staining of spleen, liver and bone marrow tissue sections of *HRG1*$^{+/+}$ and *HRG1*$^{-/-}$ mice with Perl's Prussian blue. Images shown are representative of at least 3 mice.

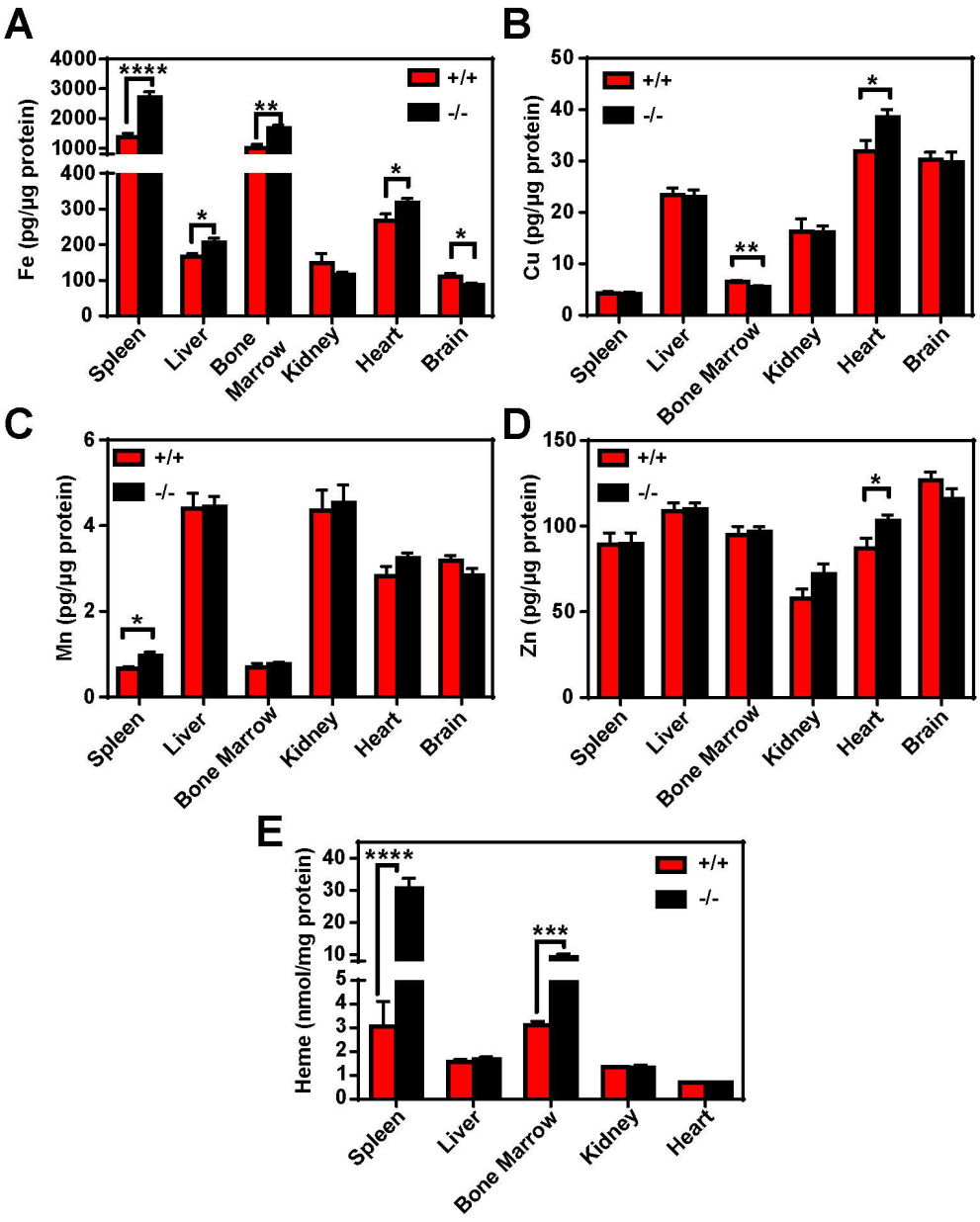

Figure 3.9 Tissue metal and heme concentrations of *HRG1*$^{+/+}$ and *HRG1*$^{-/-}$ mice

(A) Iron (Fe) levels in tissues by ICP-MS.

(B) Copper (Cu) levels in tissues by ICP-MS.

(C) Manganese (Mn) levels in tissues by ICP-MS.

(D) Zinc (Zn) levels in tissues by ICP-MS.

(E) Heme levels in tissues by UPLC.

Mice were fed a standard iron diet (n=6-17). *p<0.05; **p<0.01; ***p<0.001; ****p<0.0001.

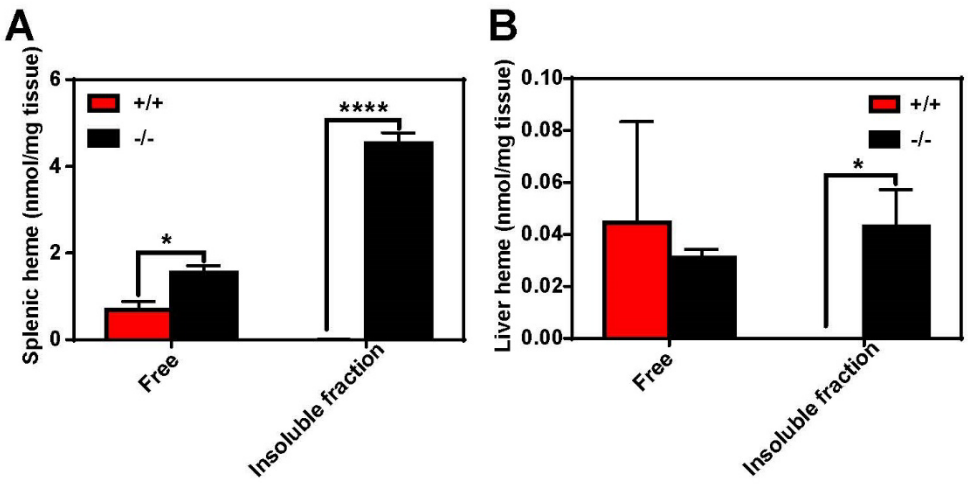

Figure 3.10 Quantification of hemozoin in *HRG1*$^{-/-}$ tissues

(A) Spleen non-hemozoin heme (free) and hemozoin (insoluble fraction) quanitifcations.

(B) Liver non-hemozoin heme (free) and hemozoin (insoluble fraction) quanitifcations.

Quantifications were done by extraction and spectrophotometric measurements (n=3). *p<0.05; ****p<0.0001.

Hemozoin accumulates within enlarged lysosomes of *HRG1*$^{-/-}$ reticuloendothelial macrophages

F4/80 or EMR1 is a cell surface adhesion EGF-GPCR family member restricted to mouse macrophages[185]. Immunohistochemistry with F4/80 antibodies on paraffin-embedded tissue sections revealed the localization of hemozoin to be within F4/80^{+} cells in RES tissues of *HRG1*$^{-/-}$ mice **(Fig. 3.11A)**. We isolated F4/80^{+} bone marrow macrophages (BMMs) by antibody-specific magnetic beads separation and conducted immunofluorescence to determine the intracellular localization of hemozoin. Transmission electron microscopy showed that hemozoin localizes to a membrane-encapsulated compartment within *HRG1*$^{-/-}$ BMMs and spleen macrophages, but is absent in isolated bone marrow monocytes or *in vitro* bone marrow-derived macrophages (**APPENDIX V, VI**). Immunofluorescence with antibodies against LAMP1, a type I transmembrane glycoprotein enriched on endolysosomal membranes[186], confirmed that the hemozoin were confined within LAMP1^{+} vesicles in *HRG1*$^{-/-}$ that were significantly larger in diameter **(Fig. 3.11B, C)**. Isolated F4/80^{+} BMMs also contained significantly more cellular iron, through X-ray fluorescence microscopy where the iron-laden region of interests (ROI) corresponded to hemozoin within the BMMs (In collaboration with Dr. Martina Ralle, Oregon Health Sciences University; **APPENDIX VII-IX**).

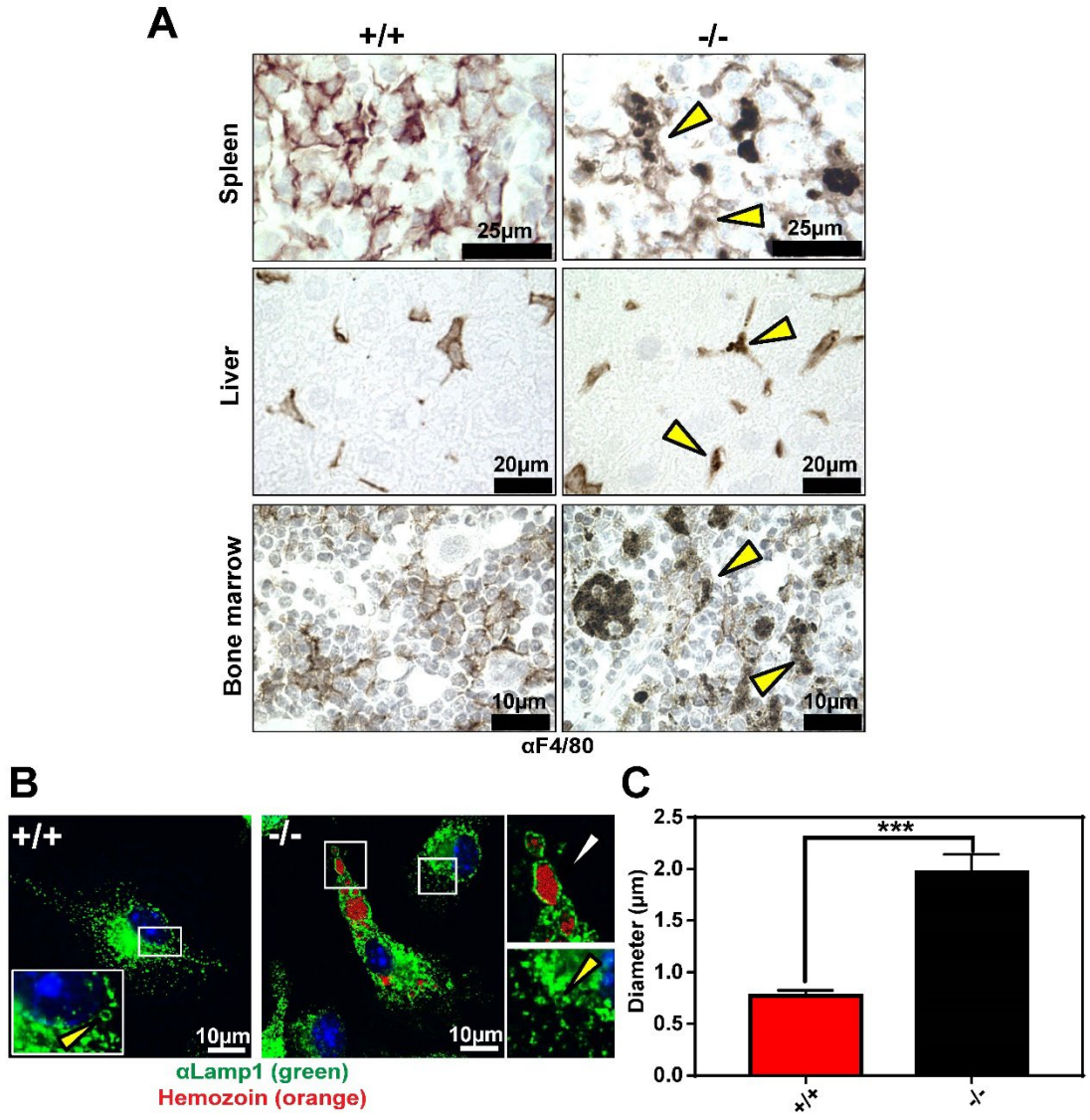

Figure 3.11 Hemozoin accumulates in LAMP1^{+} vesicles in *HRG1*$^{-/-}$ RES macrophages

(A) F4/80 immunohistochemistry analysis of paraffin-embedded tissue sections of mice. Images shown are representative of at least 3 mice per genotype.

(B) Confocal microscopy of bone marrow macrophages from *HRG1*$^{+/+}$ and *HRG1*$^{-/-}$ mice probed with anti-LAMP1 antibody and secondary alexa-488 antibody. Hemozoin is pseudocolored as orange. At least 20 cells were analyzed per genotype.

(C) Diameter of LAMP1^{+} vesicles observed in F4/80^{+} bone marrow macrophages. In both *HRG1*$^{+/+}$ and *HRG1*$^{-/-}$ cells, the diameters of LAMP1^{+} structures with distinguishable boundaries were quantified manually by ImageJ software analysis. *HRG1*$^{+/+}$: 4 cells, 3-5 structures per cell; *HRG1*$^{-/-}$: 11 cells, 3-12 structures per cell. ***p<0.001.

Splenic red pulp macrophages are significantly fewer in *HRG1*$^{-/-}$ mice

Heme accumulation in cells has been reported to be associated with cellular toxicity[137], however the detrimental effects of hemozoin on cell viability are less well understood[187]. As *HRG1*$^{-/-}$ spleens have significantly more non-hemozoin heme **(Fig. 3.10A)**, we wondered if the quantities of splenic red pulp macrophages (RPMs) would be also different in these spleens. Quantification of RPMs in *HRG1*$^{-/-}$ mice by flow cytometry showed significantly fewer splenic red pulp macrophages (F4/80^{hi}Treml4^{+}) than in *HRG1*$^{+/+}$ spleens **(Fig. 3.12A, B)**. This was accompanied by an imbalance in monocyte populations quantified by the ratio of mature to immature monocytes.**(Fig. 3.12C, D)**. In *HRG1*$^{-/-}$ spleens, the ratio of F4/80^{int} to F4/80^{lo} - CD11b^{hi} monocytes was significantly higher than in *HRG1*$^{+/+}$ spleens **(Fig. 3.12C, D)**. There were also fewer neutrophils (Gr-1^{+}CD11b^{hi}) in the spleens of *HRG1*$^{-/-}$ mice **(Fig. 3.12E, F)**.

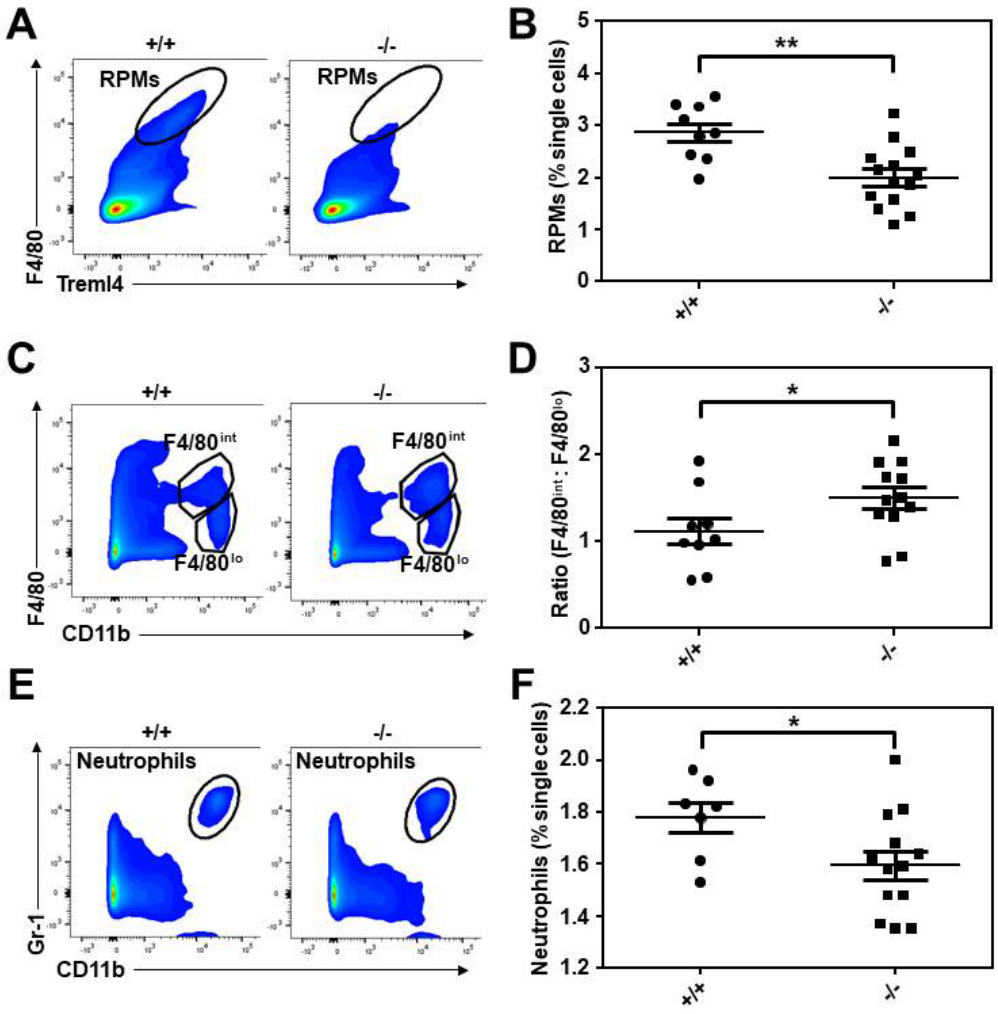

Figure 3.12 *HRG1*$^{-/-}$ mice have fewer splenic red pulp macrophages

(A, C, E) Gating strategies of different splenic populations: splenic F4/80^{hi}Treml4^{+} red pulp macrophages (RPMs), F4/80^{hi}, F4/80^{lo}-CD11b^{hi} splenic monocytes and Gr-1^{+}CD11b^{hi} neutrophils.

(B, D, F) Quantification of RPMs, monocytes and neutrophils. At least 100,000 single cells were analyzed per sample. Each dot represents one mouse. *p<0.05; **p<0.01.

***In vivo* apoptosis of *HRG1*$^{-/-}$ RES macrophages results in liver hemozoin accumulation**

Intracellular hemozoin produced by parasites is typically thought to be inert and human monocytes are able to ingest malarial hemozoin where the ingested Hz remains unmodified for long periods of time[188]. We wondered whether mouse Hz in *HRG1*$^{-/-}$ mice could be used as a source of iron when macrophages are forced to undergo apoptosis. To test this, we administered clodronate liposomes to *HRG1*$^{+/+}$ and *HRG1*$^{-/-}$ iron-deficient mice. When administered intravenously, macrophages in the spleen, liver, lung and peritoneal phagocytose the clodronate-containing liposomes resulting in the accumulation of intracellular clodronate. This leads to irreversible cellular toxicity and apoptosis of macrophages *in vivo*[189]. Using this method, we were able to deplete splenic, liver and bone marrow F4/80^{+} macrophages *in vivo* **(Fig. 3.13A-D)**. Day 3 post-injection, no F4/80 staining could be observed in histological sections of clodronate-treated mice spleen, liver and bone marrow **(Fig. 3.13A-C)**. On day 7 post-injection, partial F4/80 staining could be observed in the spleens, livers and bone marrows of clodronate-treated mice as compared to control liposome injected mice **(Fig. 3.13A-C)**. Despite the loss of RES macrophages, *HRG1*$^{-/-}$ spleens, livers and bone marrows still retained hemozoin, which were now extruded into the interstitial space **(Fig. 3.13A-C, right panel, Fig. 3.14)**. Flow cytometry analysis of clodronate-treated spleens revealed significant depletion of RPMs day 7 post-injection but RPMs were repopulated by day 14 **(Fig. 3.13D)**.

We reasoned that since the mice were anemic from iron-deficiency, if Hz released upon apoptosis of macrophages was reutilized as a bioavailable source of iron, iron-deficiency anemia could be overcome by observable changes in the

hematocrit. There was no difference in hematocrits post-clodronate administration **(Fig. 3.15A)**. Total erythroid cells in the bone marrow decreased significantly in both *HRG1*$^{+/+}$ and *HRG1*$^{-/-}$ mice three days post-clodronate treatment **(Fig. 3.15B)**, consistent with previous reports that *in vivo* depletion of macrophages by clodronate negatively impacts erythropoiesis[190]. Analyses of Ter-119^{+} subpopulations of erythroblasts in the bone marrow show a shift in maturation of erythroblast populations towards later stages after clodronate treatment compared to control **(Fig. 3.15C, 3.16A, B; populations V and IV)**. At days 7 and 14 post-clodronate injection, the erythroblast subpopulations return to levels similar to control mice **(Fig. 3.15C, 3.16A, C, D)** In the spleen, where extramedullary erythropoiesis can occur, total erythroid cells increased significantly after clodronate treatment before returning to normal levels 7 days post-injection **(Fig. 3.17A)**, indicative of stress erythropoiesis caused by clodronate[190]. Similar to the bone marrow, splenic erythroblasts showed a decrease in immature subpopulations **(Fig. 3.17B, populations III+II+I)** but with no corresponding increase in mature subpopulations **(Fig. 3.17B, populations V+IV)**. Splenic erythroblast subpopulations resumed to control levels 14 days post-clodronate injection **(Fig. 3.17)**.

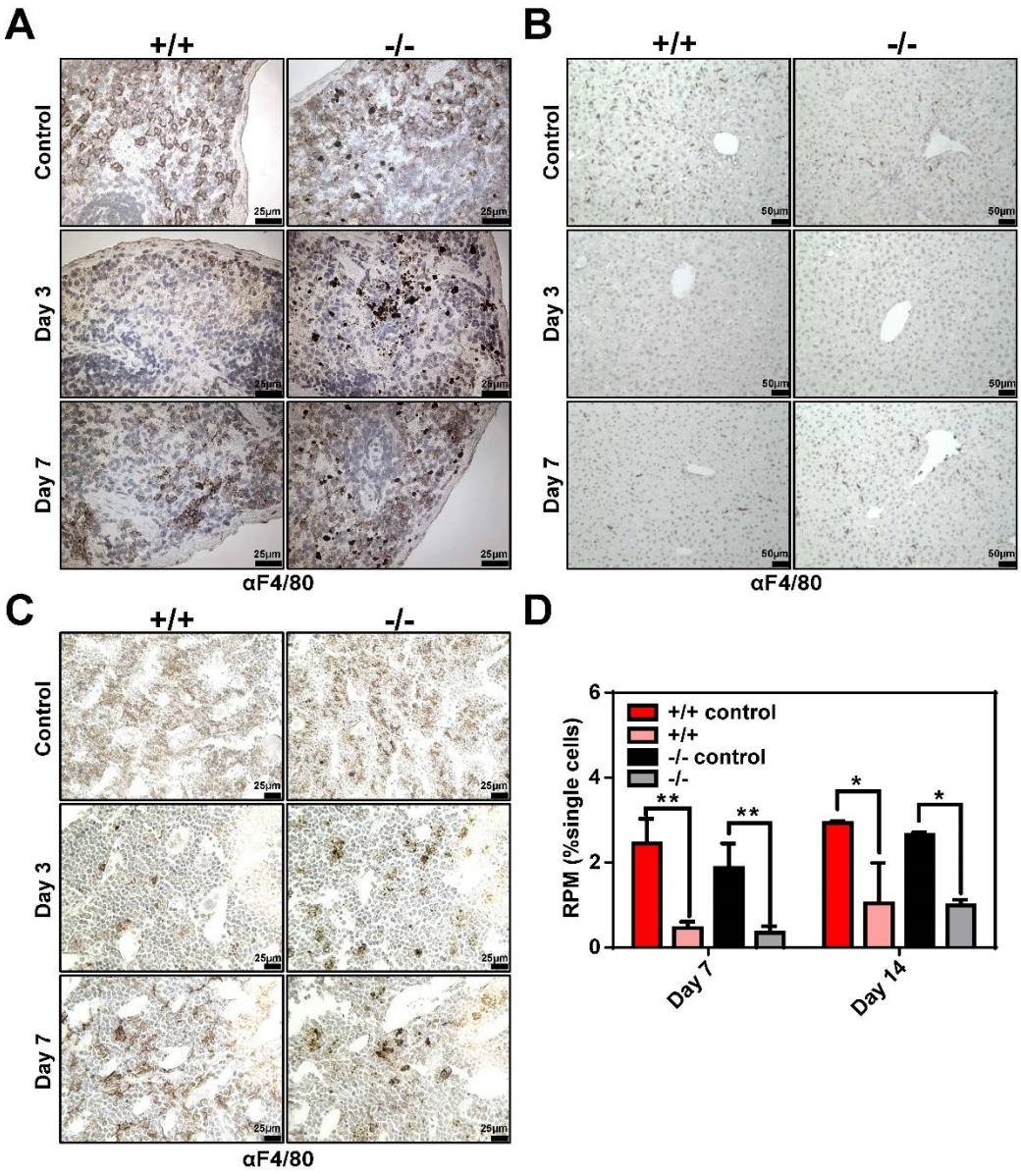

Figure 3.13 Clodronate-liposome injection depletes RES macrophages *in vivo*

(A) Spleen, **(B)** liver and **(C)** bone marrow F4/80 immunohistochemistry analysis of paraffin-embedded tissue sections Control animals were injected with control-liposomes, day 3 and 7 indicates mice which were injected with clodronate-containing liposomes on day 0. Images shown are representative of at least 3 mice per group.

(D) Flow cytometry quantification of F4/80^{hi}Treml4^{+} RPMs in control and clodronate-treated mice (n=2-4) on days 7 and 14 post-injection. *p<0.05; **p<0.01.

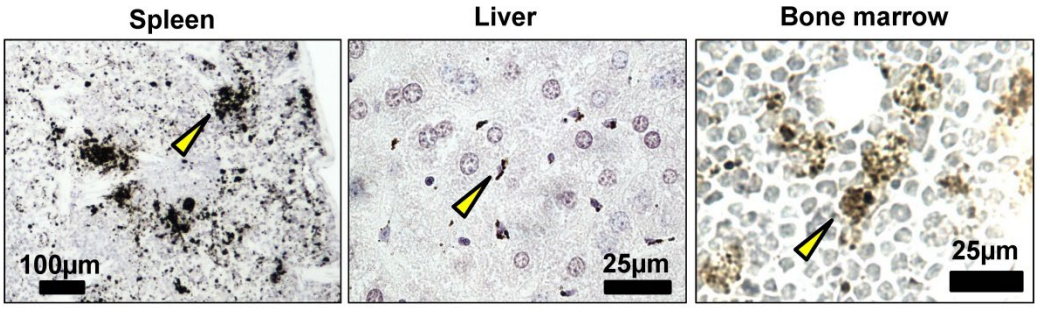

Figure 3.14 Hemozoin remains in interstitial spaces of *HRG1*$^{-/-}$ RES tissues in absence of macrophages

High magnification images of *HRG1*$^{-/-}$ spleen, liver and bone marrow on Day 3 post-clodronate. Tissue sections were lightly stained with hematoxylin. Yellow arrows point to hemozoin in interstitial spaces of tissues.

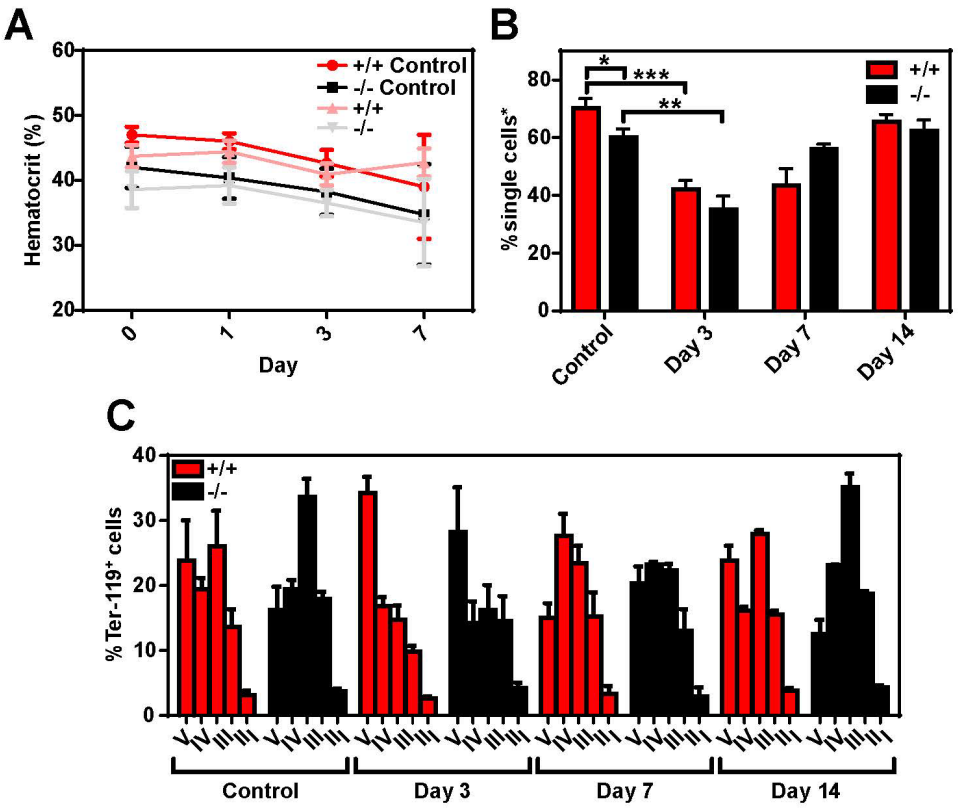

Figure 3.15 Clodronate treatment causes changes in bone marrow erythropoiesis

(A) Hematocrits of mice treated with control or liposome liposomes. n=6-14.

(B) Quantification of total Ter-119$^+$ cells in bone marrows of mice treated with control or liposome liposomes. n=2-6. The %single cells* on the y-axis denote single cells that are negative for CD4/8/41, B220 and Gr-1.

(C) Quantification of subpopulations of Ter-119$^+$ cells represented as a percentage of total Ter-119$^+$ cells in the bone marrow of mice treated with control or liposome liposomes. n=2-6. At least 100,000 single cells were analyzed per sample. *p<0.05; **p<0.01; ***p<0.001.

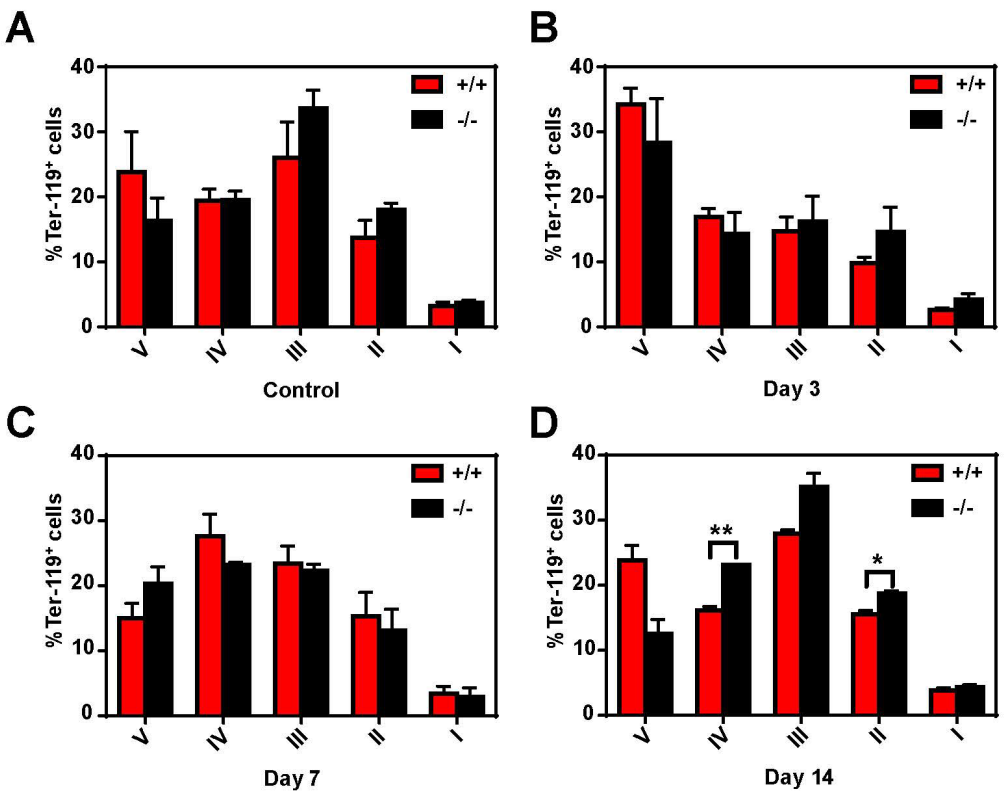

Figure 3.16 Clodronate treatment enhances maturation of erythroblasts in bone marrow

Quantification of subpopulations of Ter-119$^+$ cells represented as a percentage of total Ter-119$^+$ cells in the bone marrow. n=2-6.

(A) Control liposome-treated mice.

(B-D) Clodronate liposome-treated mice on days 3, 7 and 14 post-treatment. At least 100,000 single cells were analyzed per sample. *p<0.05; **p<0.01.

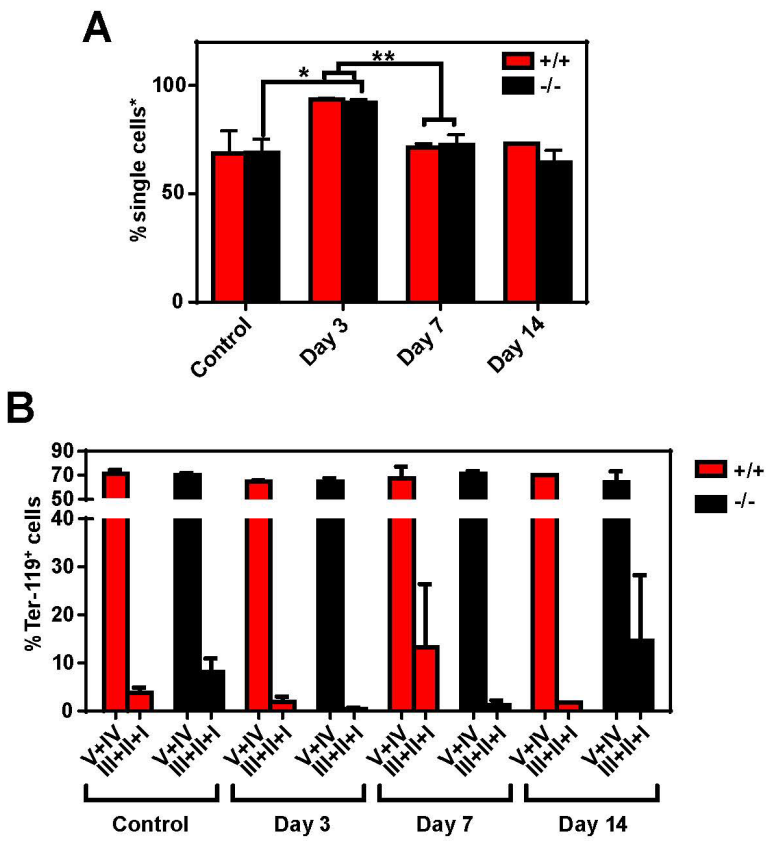

Figure 3.17 Clodronate treatment leads to splenic stress erythropoiesis

(A) Quantification of total Ter-119$^+$ cells in spleens of mice treated with control or liposome liposomes. n=2-6. The %single cells* on the y-axis denote single cells that are negative for CD4/8/41, B220 and Gr-1.

(B) Quantification of subpopulations of Ter-119$^+$ cells represented as a percentage of total Ter-119$^+$ cells in the spleens of mice treated with control or liposome liposomes. n=2-6. At least 100,000 single cells were analyzed per sample. *p<0.05; **p<0.01.

There was no gross difference in the appearances of spleens or livers of *HRG1*$^{+/+}$ mice after clodronate treatment **(Fig. 3.18A-D)** but *HRG1*$^{-/-}$ livers appeared to be darker in color after cloronate treatment **(Fig. 3.18B, D)**. Non-hemozoin heme levels, which were initially higher in *HRG1*$^{-/-}$ spleens, decreased significantly post-clodronate treatment **(Fig. 3.19A)**, with a concomitant increase in the liver post-clodronate**(Fig. 3.19B)**, but no significant changes in the kidneys **(Fig. 3.19A-C)**. Surprisingly, hemozoin levels in *HRG1*$^{-/-}$ spleens decreased significantly after clodronate treatment **(Fig. 3.20A)**, while hemozoin levels in *HRG1*$^{-/-}$ livers increased significantly **(Fig. 3.20B)**; hemozoin was not detected in *HRG1*$^{-/-}$ kidney or *HRG1*$^{+/+}$spleens and livers before and after clodronate treatment **(Fig. 3.19A, B)**.

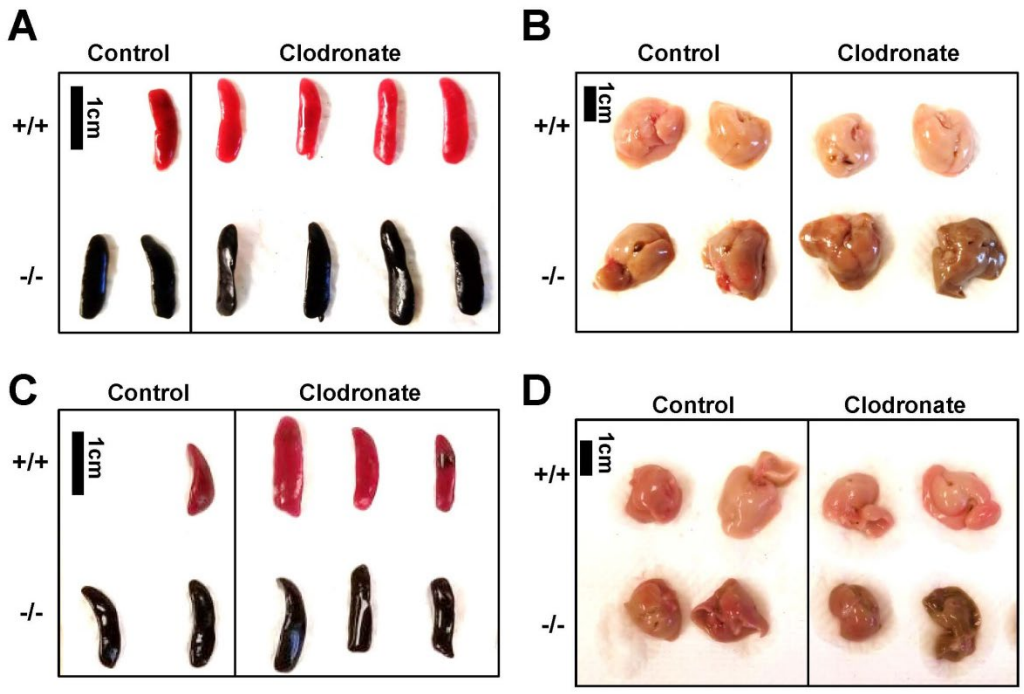

Figure 3.18 *HRG1*$^{-/-}$ livers show darkening post-clodronate treatment

Images of **(A)** spleens and **(B)** livers from control and clodronate liposomes-treated mice on day 3 post-treatment.

Images of **(C)** spleens and **(D)** livers from control and clodronate liposomes-treated mice on day 7 post-treatment.

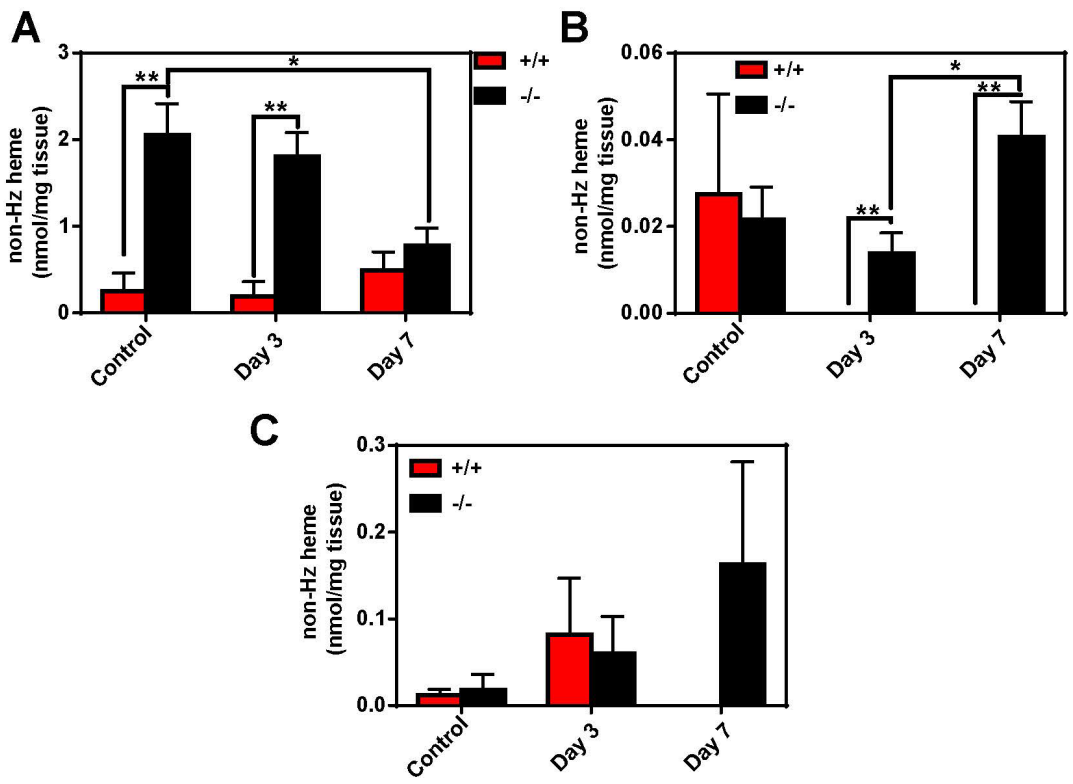

Figure 3.19 Non-hemozoin heme levels decrease in spleens but increase in livers of *HRG1*$^{-/-}$ mice after clodronate treatment

(A) Spleen, **(B)** liver and **(C)** kidney non-hemozoin heme levels of control and clodronate treated mice. n=4-6. *p<0.05; **p<0.01.

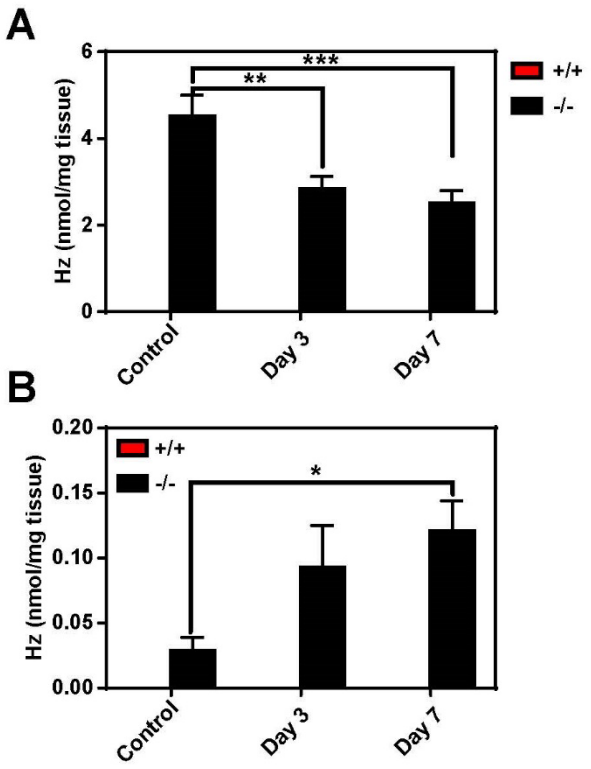

Figure 3.20 Hemozoin levels decrease in spleens but increase in livers of *HRG1*$^{-/-}$ mice after clodronate treatment

(A) Spleen and **(B)** liver hemozoin levels in control and clodronate treated *HRG1*$^{-/-}$ mice. n=4-6. *p<0.05; **p<0.01; ***p<0.001.

While histochemical staining by Perls' Prussian blue did not show differences in iron deposits, *HRG1*$^{-/-}$ liver from mice treated with clodronate appear to contain more hemozoin deposits in the liver, in spaces between hepatocytes **(Fig. 3.21)**, which corresponds to the quantification by extraction and spectrophotometric measurements of hemozoin **(Fig. 3.20B)**.

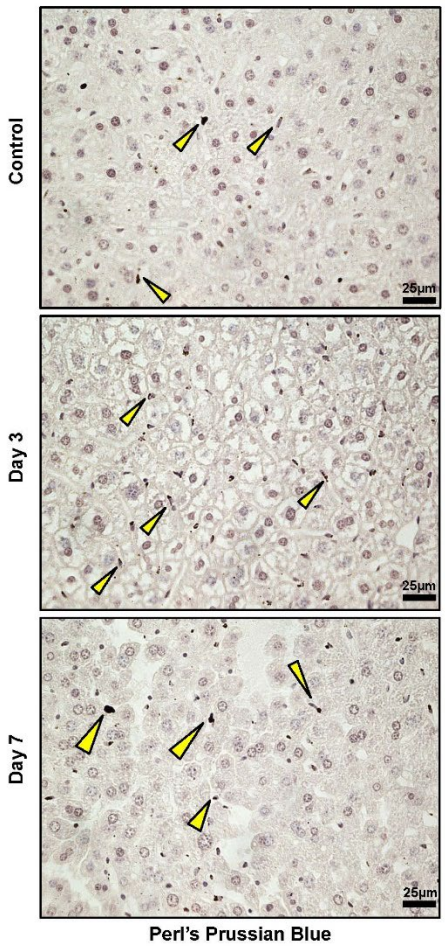

Figure 3.21 Hemozoin accumulates in interstitial spaces of clodronate-treated *HRG1*$^{-/-}$ livers

Histochemical staining of *HRG1*$^{-/-}$ livers by Perls' Prussian blue of control and clodronate treated mice. Images shown are representative of at least 2 mice per group. Yellow arrows indicate hemozoin deposits in liver sections.

Discussion

During erythrophagocytosis in macrophages, heme transporter HRG1 and iron transporter NRAMP1 both localize to the erythrophagosomal membrane, transporting heme and iron into the cytosol for recycling[107,109]. The *NRAMP1*$^{-/-}$ mouse displays modest changes with regards to erythrocyte iron recycling[108], indicating that the major source of recycled iron is derived from heme. Previously, *in cellula* studies using murine bone marrow-derived macrophages revealed that HRG1 transports heme out of the phagolysosome during erythrophagocytosis[109]. The prevailing model would predict that a complete loss of *HRG1* would lead to ineffective heme-recycling and heme accumulation within phagolysosomes of macrophages. Combined with the known toxic properties of heme, cellular heme accumulation could potentially cause macrophage death, as seen in the *HMOX1*-deficient mouse[137]. We observed that *HRG1*$^{-/-}$ mice were indeed incapable of recycling heme-iron efficiently from ingested RBCs, resulting in heme accumulation in RES tissues. Tissue metal concentrations were also aberrant in *HRG1*$^{-/-}$ tissues, suggesting a dysregulation in systemic balance of metal concentrations. *HRG1*$^{-/-}$ macrophages showed heme sequestration within LAMP1^{+} compartments. However, unlike the complete loss of RES macrophages in *HMOX1*-deficient mice, *HRG1*$^{-/-}$ mice retained splenic RPMs, albeit at significantly lower levels as compared to *HRG1*$^{+/+}$ mice. The sequestered heme was identified as an inert, crystalline form of heme, known as hemozoin. Consistent with the function of hemozoin formation in blood-feeding parasites, hemozoin formation in *HRG1*$^{-/-}$ macrophages appears to be a mechanism of heme tolerance, protecting RES macrophages from heme toxicity. *In vivo* apoptosis of *HRG1*$^{-/-}$ macrophages by

clodronate administration released hemozoin into interstitial spaces of RES tissues but did not rescue anemia, suggesting that iron and heme from hemozoin is not bioavailable for erythropoiesis. In addition to ineffective heme recycling, *HRG1*$^{-/-}$ mice also showed ineffective bone marrow erythropoiesis concomitant with reduced hematocrits and splenic extramedullary erythropoiesis. These observations suggest that the cellular location of heme accumulation can dictate the cytotoxicity. We also showed the first incidence of mammalian hemozoin formed *in vivo*, suggesting that mammals have an additional form of heme detoxification mechanism - through hemozoin formation.

Chapter 4 : Iron metabolism is aberrant in *HRG1*-deficient mice

Summary

Mice obtain their daily requirement of iron from both dietary and recycled sources. It has been shown that mice on an iron-rich diet can circumvent a block in heme-iron recycling by relying more on dietary iron for erythropoiesis[172]. To understand the implications that a defective heme-iron recycling pathway has on systemic iron metabolism, we placed *HRG1*$^{-/-}$ mice on a low-iron diet. We observe that under prolonged dietary iron limitation, *HRG1*$^{-/-}$ mice are unable to sustain erythropoiesis and become severely anemic. The stress erythropoiesis response is inefficient and the bone marrow erythropoiesis defect is enhanced under dietary iron limitation. *HRG1*$^{-/-}$ mice also retain tissue hemozoin under iron-deficiency and show aberrant regulation of iron metabolism genes. Under iron-deficiency anemia, *HRG1*$^{-/-}$ mice accumulate more hemozoin in the liver. Despite dysregulation in iron metabolism, *HRG1*$^{-/-}$ mice, surprisingly, do not display altered dietary iron uptake or distribution.

Results

***HRG1*$^{-/-}$ mice are susceptible to extreme anemia under prolonged dietary iron limitation**

The standard rodent diet fed to mice contains 380 ppm of iron, which is more than five times the amount of iron (25 to 100 ppm) required for normal growth and hematopoiesis of laboratory mice[191]. Given that the amount of recycled iron contributes to approximately 50% of the total daily iron needs of mice and the remaining is accounted for by dietary intake[172], limiting dietary iron would increase

the relative contribution of recycled iron to the daily erythropoietic needs. *HRG1*$^{-/-}$ mice are inefficient in recycling heme-iron, but they do not show an overt defect in RBC production under basal conditions. To evaluate the impact of heme-iron recycling, we placed weaned mice on a diet containing 10 ppm iron and observed the effects of limiting dietary iron on erythropoiesis by monitoring hematocrit weekly. Over a period of six weeks post-weaning, we observed that both *HRG1*$^{+/+}$ and *HRG1*$^{-/-}$ mice showed a gradual increase in hematocrit, although *HRG1*$^{-/-}$ mice showed hematocrits that were significantly lower than *HRG1*$^{+/+}$ mice **(Fig. 4.1A)**. This indicates that the defect in heme-iron recycling only manifests into iron-deficiency anemia in *HRG1*$^{-/-}$ mice when dietary iron becomes limiting and body iron stores are lowered.

To further understand changes in iron metabolism and response to iron-deficiency in the *HRG1*$^{-/-}$ mice, we placed the mice on a low-iron diet (2 ppm Fe). Over a period of five weeks, both *HRG1*$^{+/+}$ and *HRG1*$^{-/-}$ mice exhibited similarly-reduced hematocrits, although *HRG1*$^{-/-}$ mice become anemic quicker than *HRG1*$^{+/+}$ mice **(Fig. 4.1B)**. However, over 20 weeks, anemic *HRG1*$^{+/+}$ mice maintained their hematocrit while *HRG1*$^{-/-}$ mice showed a dramatic decline **(Fig. 4.1C)**, eventually leading to death of *HRG1*$^{-/-}$ mice **(Fig. 4.2)**.

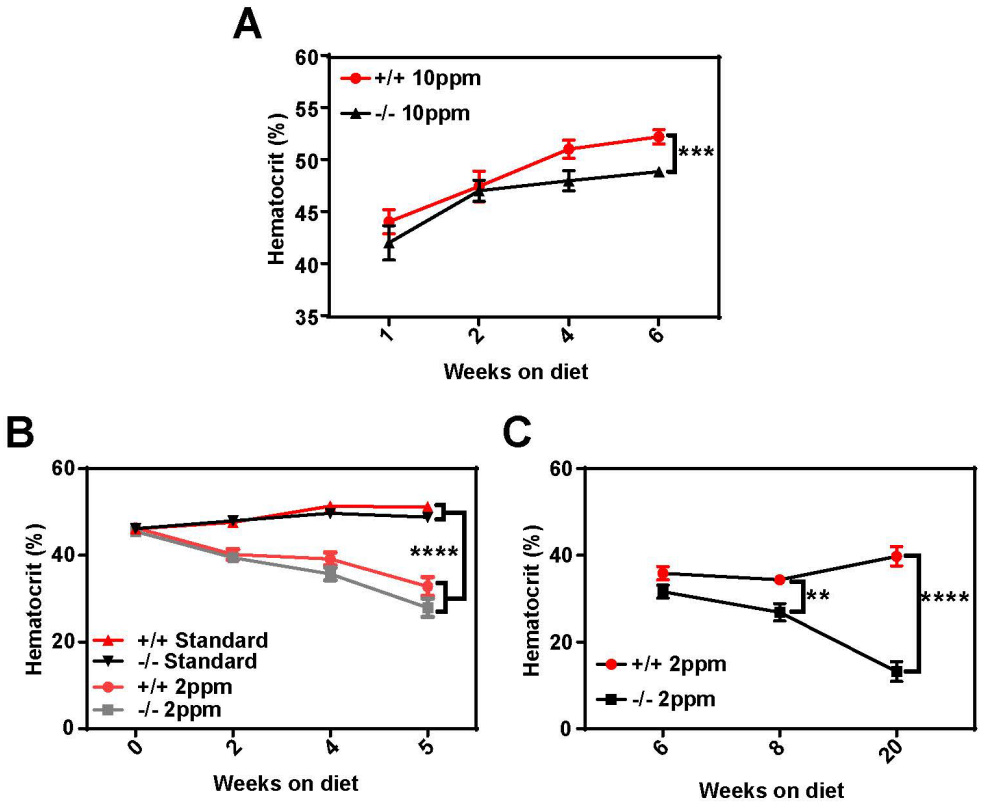

Figure 4.1 *HRG1*$^{-/-}$ mice rely on dietary iron to sustain erythropoietic needs

Hematocrits of *HRG1*$^{+/+}$ and *HRG1*$^{-/-}$ mice placed on a moderate (10 ppm) **(A)**, standard or low (2 ppm) iron diet over 5 **(B)** to 20 **(C)** weeks. Mice were placed on respective diets supplemented with deionized water starting at 21 days of age (week 0) (n=10 for **(A)**; n=9-15 for **(B)**; n=7-11 for **(C)**). *p<0.05; **p<0.01; ***p<0.001; ****p<0.0001.

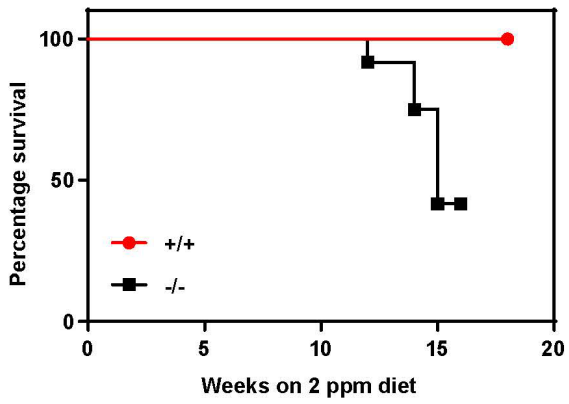

Figure 4.2 A low-iron diet leads to mortality in the absence of heme-iron recycling

Survival curve of *HRG1*$^{+/+}$ and *HRG1*$^{-/-}$ mice placed on a low iron (2 ppm) diet over 20 weeks. The experiment was terminated for *HRG1*$^{-/-}$ mice when less than 50% of *HRG1*$^{-/-}$ mice were surviving (16 weeks), while *HRG1*$^{+/+}$ mice were monitored up to 18 weeks. (n=15-17)

Iron-deficiency-induced stress erythropoiesis response is defective in *HRG1*$^{-/-}$ mice

A major hallmark of iron-deficiency anemia in mice is splenomegaly, as mice are able to compensate for reduced bone marrow erythropoiesis by inducing stress erythropoiesis in the spleen[65]. After five weeks of being fed a low-iron diet (2 ppm Fe), *HRG1*$^{+/+}$ and *HRG1*$^{-/-}$ mice were both anemic with similar hematocrits **(Fig. 4.1B)**. *HRG1*$^{+/+}$ mice showed ~130% increase in splenic weights (or % splenomegaly) when compared to mice on a standard diet, indicating splenic stress erythropoiesis **(Fig. 4.3A)**. However, the % splenomegaly experienced by *HRG1*$^{-/-}$ mice was significantly lower (~45%) **(Fig. 4.3A)**. No significant differences in weights were observed for other organs from mice maintained on a low-iron diet for five weeks **(Fig. 4.3B)**. Flow cytometry analysis of the splenic erythroid compartments revealed that the stress erythropoiesis response in iron-deficient *HRG1*$^{-/-}$ mice was significantly attenuated compared to *HRG1*$^{+/+}$ mice **(Fig. 4.4A, B)**. *HRG1*$^{-/-}$ mice had significantly lower amounts of total Ter-119^{+} cells in the spleen and a concomitant attenuated increase in immature populations. There was also a corresponding block in erythroblast differentiation at an earlier stage (population I) in the bone marrows of iron-deficient *HRG1*$^{-/-}$ mice **(Fig. 4.4C)**. Taken together, these differences suggest that *HRG1*$^{-/-}$ mice are unable to respond effectively to iron-deficiency anemia and are more severely impacted by the low-iron diet despite comparable hematocrit **(Table 3-1)**.

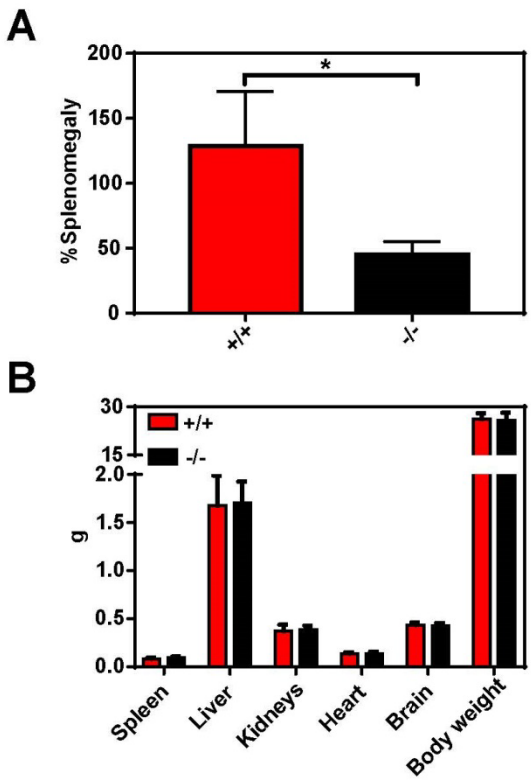

Figure 4.3 *HRG1*$^{-/-}$ mice show attenuated splenomegaly in response to iron-deficiency

(A) %Splenomegaly of *HRG1*$^{+/+}$ and *HRG1*$^{-/-}$ mice calculated by the percentage of increase in average wet weight of spleens between mice on low iron versus standard iron diets (n=9-15). **(B)** Wet weights of liver, kidneys, heart, brain and body weights from iron-deficient *HRG1*$^{+/+}$ and *HRG1*$^{-/-}$ mice (n=9-15). *p<0.05.

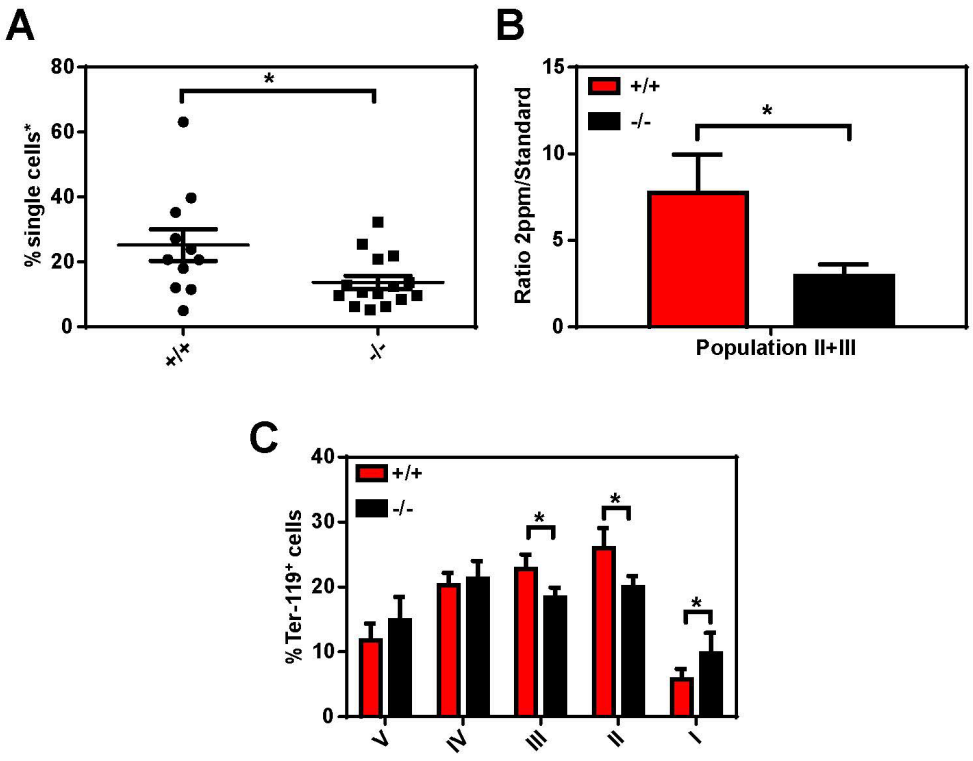

Figure 4.4 *HRG1*$^{-/-}$ mice display attenuated stress erythropoietic response

(A) Quantification of total Ter-119^{+} cells in iron-deficient mice spleens represented as a percentage of all single cells analyzed in the spleen. The %single cells* on the y-axis denote single cells that are negative for CD4/8/41, B220 and Gr-1. **(B)** Ratio of 2ppm splenic Ter-119^{+} population II+III cells to that of standard diet mice (n=8-12). **(C)** Quantification of subpopulations of Ter-119^{+} cells in iron-deficient mice bone marrows represented as a percentage of total Ter-119^{+} cells in the bone marrow (n=7-8). At least 100,000 single cells were analyzed per sample. Where applicable, each dot represents one mouse. *p<0.05.

Although circulating serum iron, TIBC, transferrin, hepcidin, EPO, hemopexin, and haptoglobin did not show significant differences between iron-deficient *HRG1*$^{+/+}$ and *HRG1*$^{-/-}$ mice, serum ferritin remained significantly elevated in *HRG1*$^{-/-}$ mice **(Table 4-1)**. Tissue iron and heme levels in RES organs were also significantly higher in iron-deficient *HRG1*$^{-/-}$ mice compared to *HRG1*$^{+/+}$ mice **(Fig. 4.5A, E)**. *HRG1*$^{-/-}$ iron-deficient spleens and brains were also aberrant in copper, manganese and zinc levels **(Fig. 4.5B-D)**.

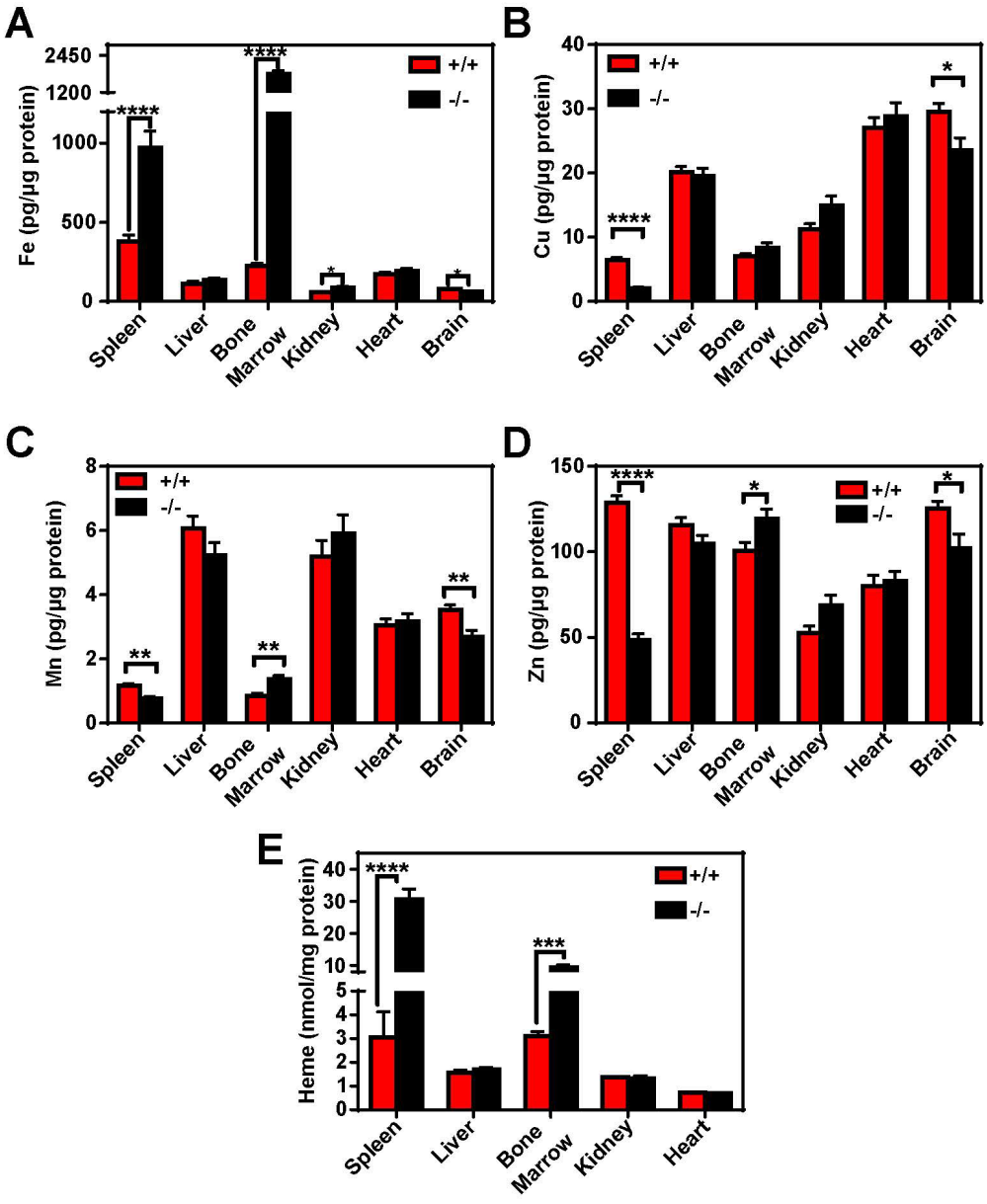

Figure 4.5 Tissue metal and heme concentrations of iron-deficient *HRG1*$^{+/+}$ and *HRG1*$^{-/-}$ mice

Quantification of tissue iron **(A)**, copper **(B)**, manganese **(C)**, zinc **(D)**, and heme **(E)** by ICP-MS and UPLC, respectively in tissues of mice fed a standard diet (n=9-15). **p*<0.05; ***p*<0.01; ****p*<0.001; *****p*<0.0001.

Table 4-1. Serum parameters of iron-deficient 10-week old *HRG1*$^{+/+}$ and *HRG1*$^{-/-}$ mice

	2ppm diet*		n
	+/+	-/-	
Serum Iron (µg/dL)	66.32±13.62	65.63±17.09	8-10
TIBC (µg/dL)	451.8±17.08	459±19.92	8-10
Transferrin saturation (%)	14.3±2.975	14.6±4.034	8-10
Ferritin (ng/mL)	284.7±63.8[a]	492±63.77[b]	11-15
Transferrin (g/L)	6.454±0.8177	6.794±0.941	11-15
EPO (pg/mL)	3217±668.3	3908±1094	9-10
Hepcidin (ng/mL)	34.72±1.025	33.55±0.9522	5-7
Haptoglobin (mg/mL)	0.2259±0.1369	6.237±2.937	5-7
Hemopexin (mg/mL)	1.169±0.1498	1.289±0.1988	4-9

*2ppm diet indicates parameters from mice that were fed a low-iron diet for five weeks

Values with different letters are significantly different from each other[a,b]

***HRG1*$^{-/-}$ mice show aberrant genetic regulation of iron metabolism genes**

To understand the molecular basis for the dampened response to iron-deficiency in *HRG1*$^{-/-}$ mice, we analyzed the genetic profile of iron metabolism genes in the spleen, liver and kidney. A total of 90 genes reported to be involved in iron metabolism (collectively termed iron regulon) were assayed from *HRG1*$^{+/+}$ and *HRG1*$^{-/-}$ mice, either on a standard (380 ppm) or low-iron (2ppm Fe for 5 weeks) rodent diet. The relative expression profiles are represented as heatmaps in **Fig. 4.6** (spleen), **Fig. 4.7** (liver) and **Fig. 4.8** (kidney). When comparing *HRG1*$^{+/+}$ and *HRG1*$^{-/-}$ mice on a standard diet, expression of three genes were significantly different in the spleens and livers. Conversely, the genetic profile of the iron regulon drastically changed under a low-iron diet, resulting in 30% of genes that were significantly dysregulated in the spleens of *HRG1*$^{-/-}$ mice compared to *HRG1*$^{+/+}$ mice **(Fig. 4.6)**. In the liver, 6% of the 90 genes were differently expressed between iron-deficient *HRG1*$^{+/+}$ and *HRG1*$^{-/-}$ mice **(Fig. 4.7)**.

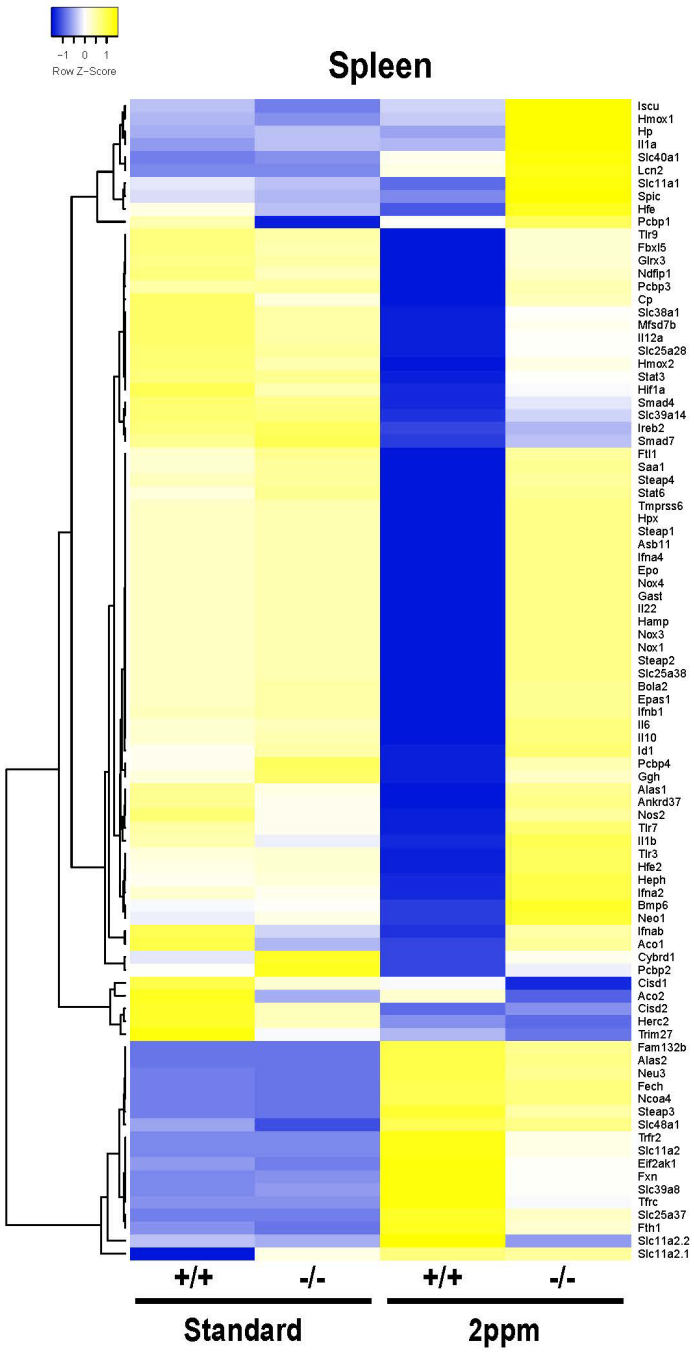

Figure 4.6 Heatmap of iron metabolism gene expression in spleen

Gene expression heat map of 90 iron metabolism genes in spleens from mice on standard or low iron (2ppm) diet. Pearson correlation was used for comparison; average linkage (n=9 per group, per genotype).

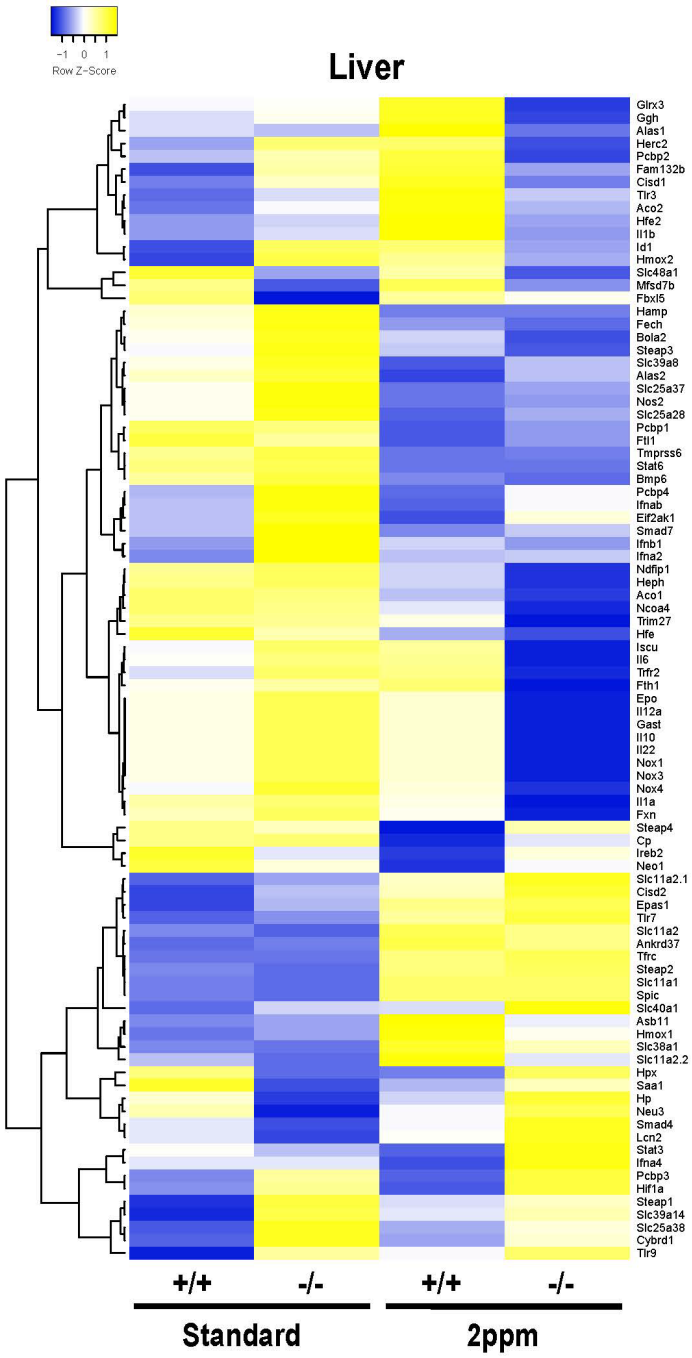

Figure 4.7 Heatmap of iron metabolism gene expression in liver

Gene expression heat map of 90 iron metabolism genes in spleens from mice on standard or low iron (2ppm) diet. Pearson correlation was used for comparison; average linkage (n=9 per group, per genotype).

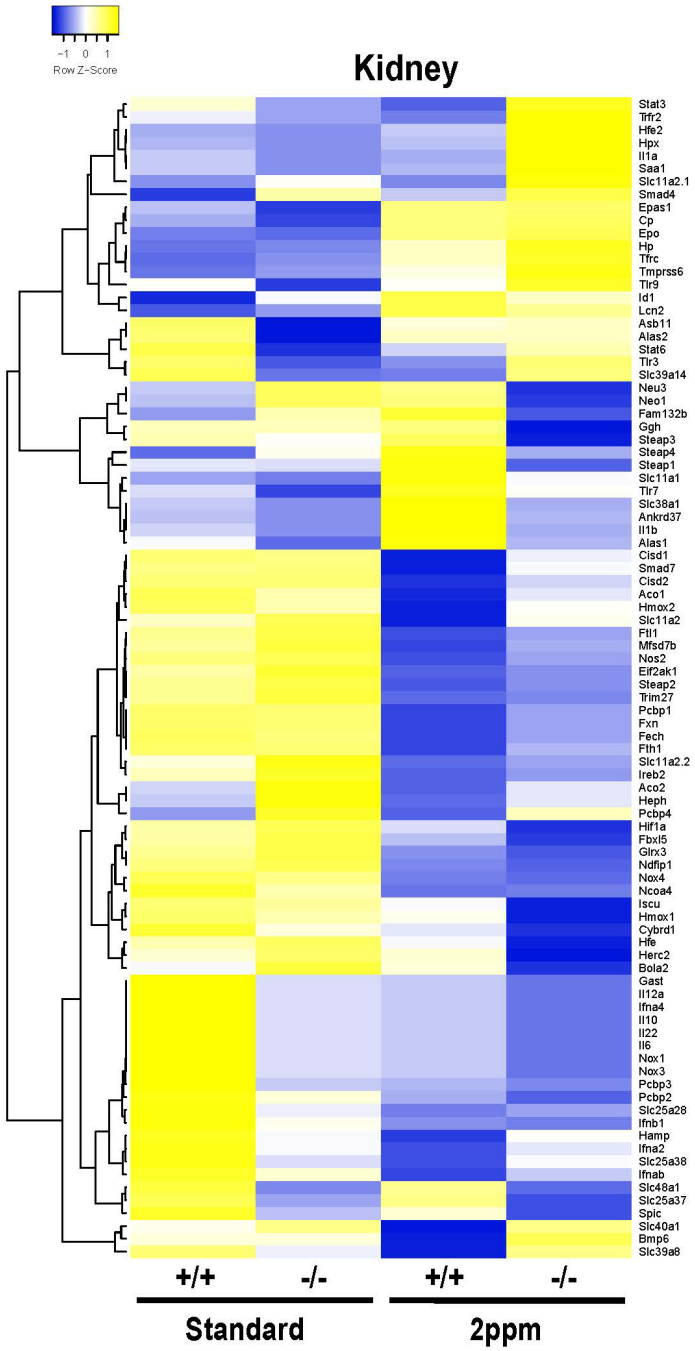

Figure 4.8 Heatmap of iron metabolism gene expression in kidney

Gene expression heat map of 90 iron metabolism genes in spleens from mice on standard or low iron (2ppm) diet. Pearson correlation was used for comparison; average linkage (n=3 per group, per genotype).

Strikingly, splenic *HAMP* was significantly upregulated in iron-deficient *HRG1*$^{-/-}$ mice and of all 36 genes that were significantly upregulated in *HRG1*$^{-/-}$ spleens at least 10 genes are known to be involved in regulation of *HAMP* **(Fig. 4.9)**. One significantly upregulated gene, bone morphogenic protein 6 (*BMP6*), is a key inducer of hepicidin[41] as BMP6-null animals display reduced liver hepcidin expression and iron overload[40]. Other genes involved in the BMP6-hepcidin regulatory pathway that were significantly upregulated include *TMPRSS6*[192] and *HFE*[193,194]. Hepcidin may also be induced independently by *IL-6*[195], *Il-22*[196] and *NOX4*[197], which were all significantly upregulated in *HRG1*$^{-/-}$ spleens. qPCR analysis of iron-deficient *HRG1*$^{-/-}$ spleens also revealed significant differences in the inflammatory status of these animals. Expression of toll-like receptor TLR3 involved in the signaling leading to pro-inflammatory cytokine IL-6[150] production was significantly higher in *HRG1*$^{-/-}$ spleens. *SAA1* and *HMOX1*, two common inflammatory status markers, were also significantly upregulated. SAA1 is an acute-phase protein typically used as a sensitive marker of inflammation in mice[198] and HMOX1 is usually produced by cells undergoing stress as a mediator to promote inflammatory modulation[199,200]. Taken together, there appears to be a general trend of inflammation in *HRG1*$^{-/-}$ spleens under iron-deficiency. However, despite the significant difference between *HRG*$^{+/+}$ and *HRG1*$^{-/-}$ spleens, only few genes were significantly disrupted in the livers **(Fig. 4.10)** and kidneys **(Fig. 4.11)**. This suggests that the major differences between *HRG*$^{+/+}$ and *HRG1*$^{-/-}$ mice originate from the spleen and its inability to cope with iron-deficiency for stress erythropoiesis induction. This is mainly because the spleen is a major site of extramedullary

erythropoiesis as well as for recycling, although the liver has been shown to undergo erythropoiesis in splenectomized animals[201].

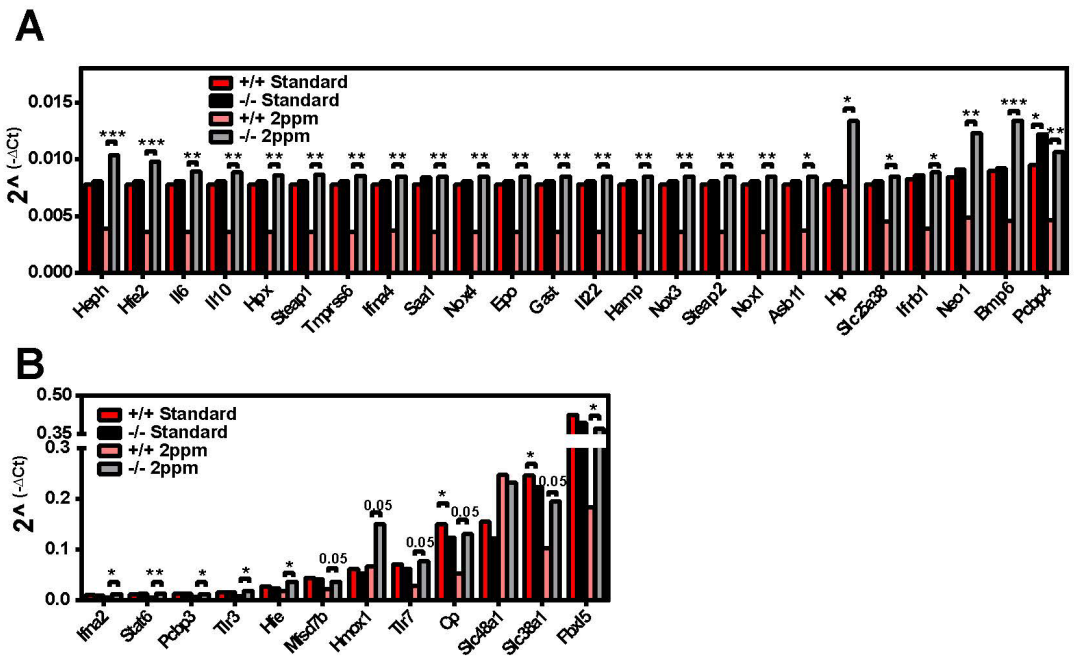

Figure 4.9 Significant dysregulation of genes in *HRG1*$^{-/-}$ spleens

(A-B) Gene expression by qPCR of iron metabolism genes in the spleens of *HRG*$^{+/+}$ and *HRG1*$^{-/-}$ mice on indicated diets (n=9 mice per group). Gene expression values were calculated as described in the methods section. **p*<0.05; ***p*<0.01; ****p*<0.001.

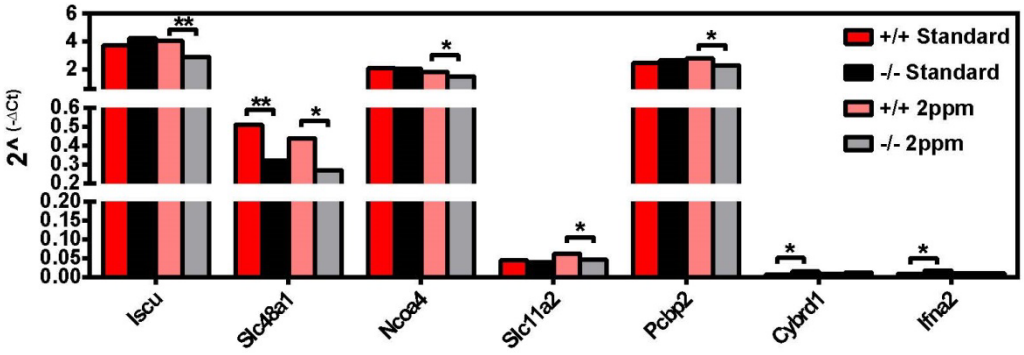

Figure 4.10 Significant dysregulation of genes in *HRG1*$^{-/-}$ livers

Gene expression by qPCR of iron metabolism genes in the livers of *HRG*$^{+/+}$ and *HRG1*$^{-/-}$ mice on indicated diets (n=9 mice per group). Gene expression values were calculated as described in the methods section. **p*<0.05; ***p*<0.01.

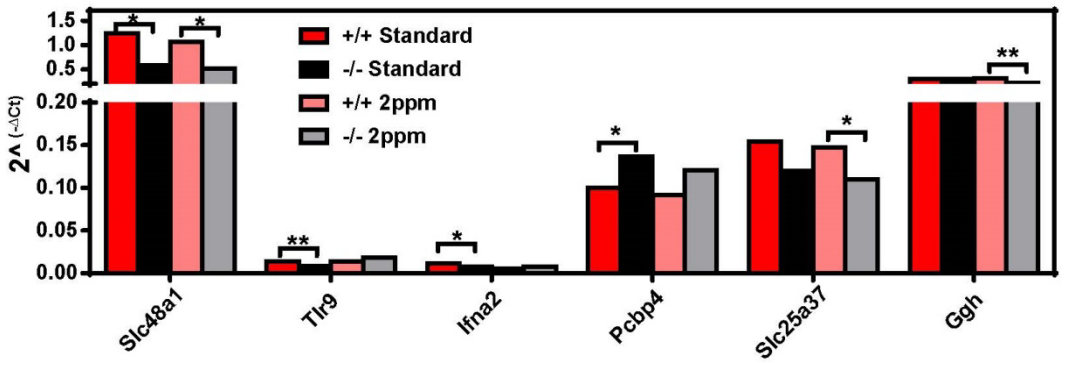

Figure 4.11 Significant dysregulation of genes in *HRG1*$^{-/-}$ kidneys

Gene expression by qPCR of iron metabolism genes in the kidneys of *HRG*$^{+/+}$ and *HRG1*$^{-/-}$ mice on indicated diets (n=3 mice per group). Gene expression values were calculated as described in the methods section. *p<0.05; **p<0.01.

***HRG1*$^{-/-}$ mice accumulate hemozoin despite severe iron-deficiency anemia**

Liver macrophages, known as Kupffer cells, have also been shown to be involved in iron-recycling by erythrophagocytosis[202]. Hence, we observed accumulation of hemozoin in liver macrophages. Quantification of non-hemozoin heme **(Fig. 4.12A, C, E)** and hemozoin **(Fig. 4.12B, D, F)** appears to suggest that there is a negative correlation of tissue heme with hematocrit values in the spleen and liver **(Fig. 4.12A-D)** but not bone marrow hemozoin **(Fig. 4.12E, F).** The increase in liver hemozoin could be a consequence of increased erythrophagocytosis of senescent circulating erythrocytes by Kupffer cells as a compensatory pathway. This hypothesis would correlate with an increased turnover of circulating erythrocytes and can be evidenced by a decreased erythrocyte lifespan. However, *in vivo* biotin-labelling of circulating erythrocytes did not show differences in RBC life span in *HRG1*$^{-/-}$ mice whether on a standard **(Fig. 4.13A)** or low-iron **(Fig. 4.13B)** diet.

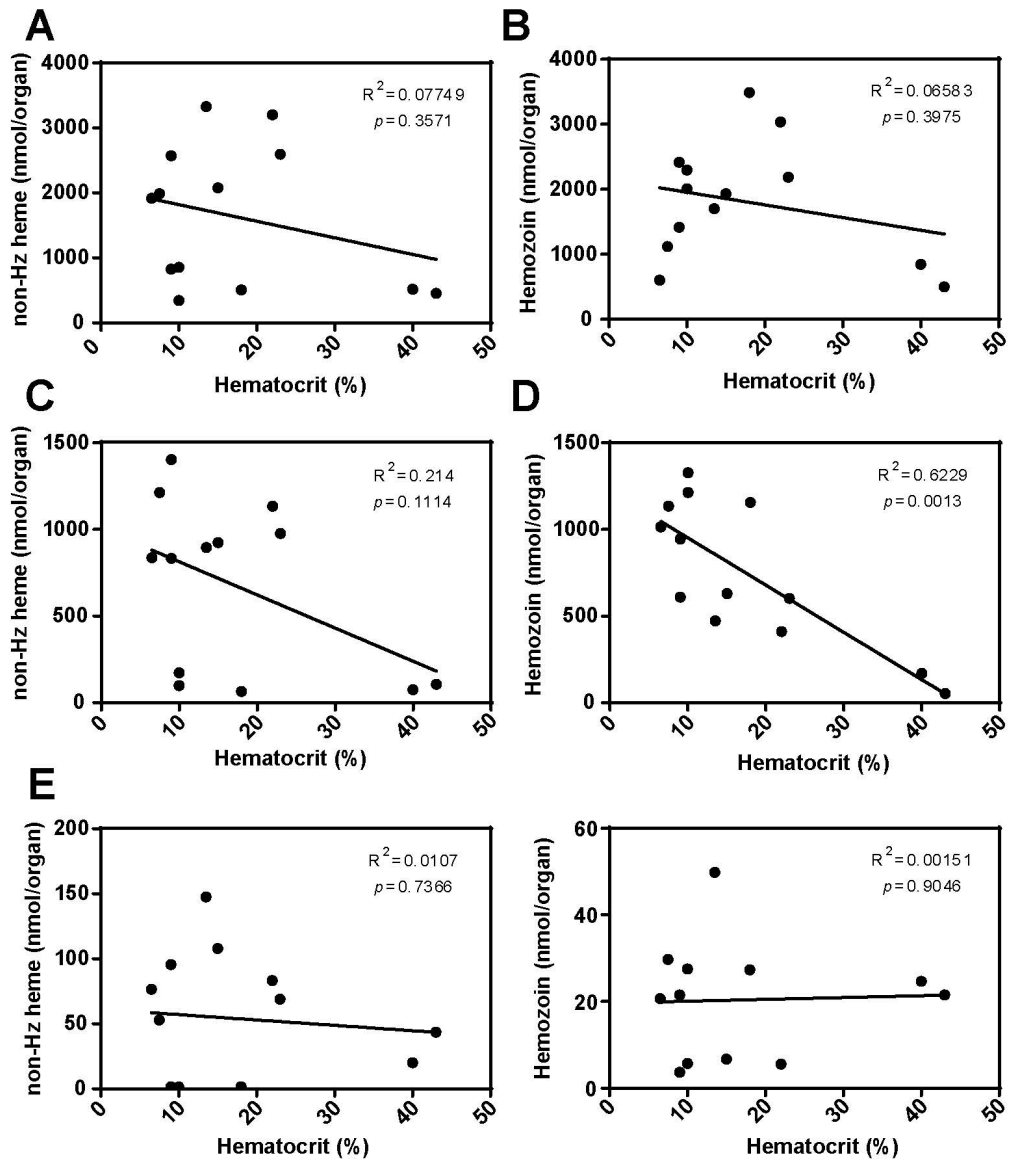

Figure 4.12 Tissue heme and hemozoin quantifications from *HRG1*$^{-/-}$ mice of varying hematocrits

Quantifications of **(A, C, E)** non-hemozoin heme and **(B, D, F)** hemozoin in the **(A, B)** spleens, **(C, D)** livers, and **(E, F)** bone marrows of *HRG1*$^{-/-}$ mice plotted against the hematocrit of each mouse. One point represents a single mouse. For bone marrow, each organ includes one femur and tibia.

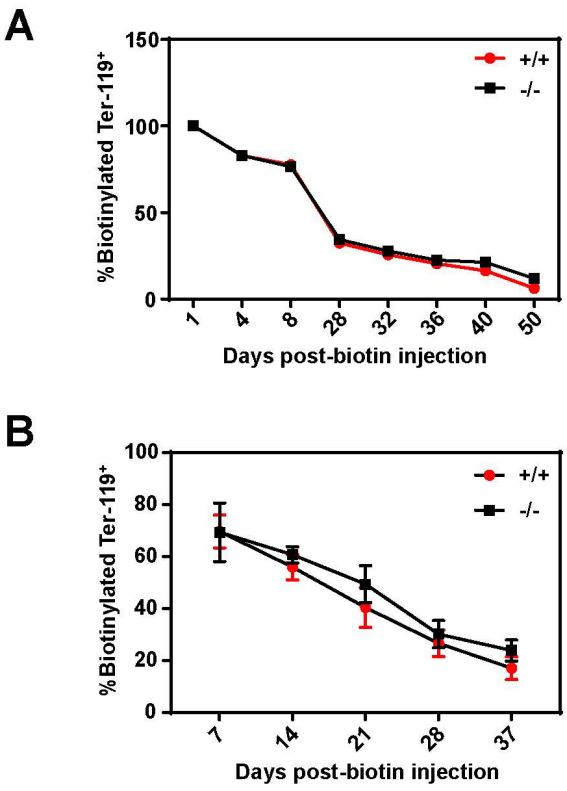

Figure 4.13 Circulating erythrocyte lifespan in *HRG*$^{+/+}$ and *HRG1*$^{-/-}$ mice

Percentage of biotinylated erythrocytes in the circulations of *HRG*$^{+/+}$ and *HRG1*$^{-/-}$ mice on a **(A)** standard or **(B)** low-iron (2ppm) diet. Biotin injections were made on day 0. **(A)** n=10 per genotype; **(B)** n=4-8 per genotype.

***HRG1*$^{-/-}$ mice do not display altered dietary iron uptake or distribution**

While *HRG1*$^{-/-}$ mice experience ineffective erythropoiesis in the bone marrow and extramedullary erythropoiesis in the spleen, they do not exhibit iron-deficiency symptoms under standard conditions. Their serum hepcidin and EPO are not significantly different from *HRG1*$^{+/+}$ mice **(Table 3-2)**. Using radiolabeled ^{59}Fe, we were able to measure any differences in dietary iron uptake and distribution by oral gavage. Under both basal and iron-deficient conditions, *HRG1*$^{+/+}$ and *HRG1*$^{-/-}$ mice did not show differences in total intestinal iron absorption or distribution to various tissues **(Fig. 4.14A-D)**, although intestinal absorption was enhanced under iron-deficiency **(Fig. 4.14E)**. Likewise, when ^{59}Fe was administered intravenously (IV) with 5 μg of $FeSO_4$ to measure transferrin-bound iron (TBI) uptake, tissue iron distribution were similar between *HRG1*$^{+/+}$ and *HRG1*$^{-/-}$ mice **(Fig. 4.15A, B)**. However, when ^{59}Fe was administered IV with excess $FeSO_4$ (70 μg), which saturates circulating transferrin, to measure non-transferrin-bound iron (NTBI) uptake, the ^{59}Fe distribution pattern to various tissues differed between *HRG1*$^{+/+}$ and *HRG1*$^{-/-}$ mice **(Fig. 4.15C, D)**. We observed that significantly more ^{59}Fe-NTBI was distributed to the spleens of *HRG1*$^{-/-}$ mice than *HRG1*$^{+/+}$ mice **(Fig. 4.15C)**.

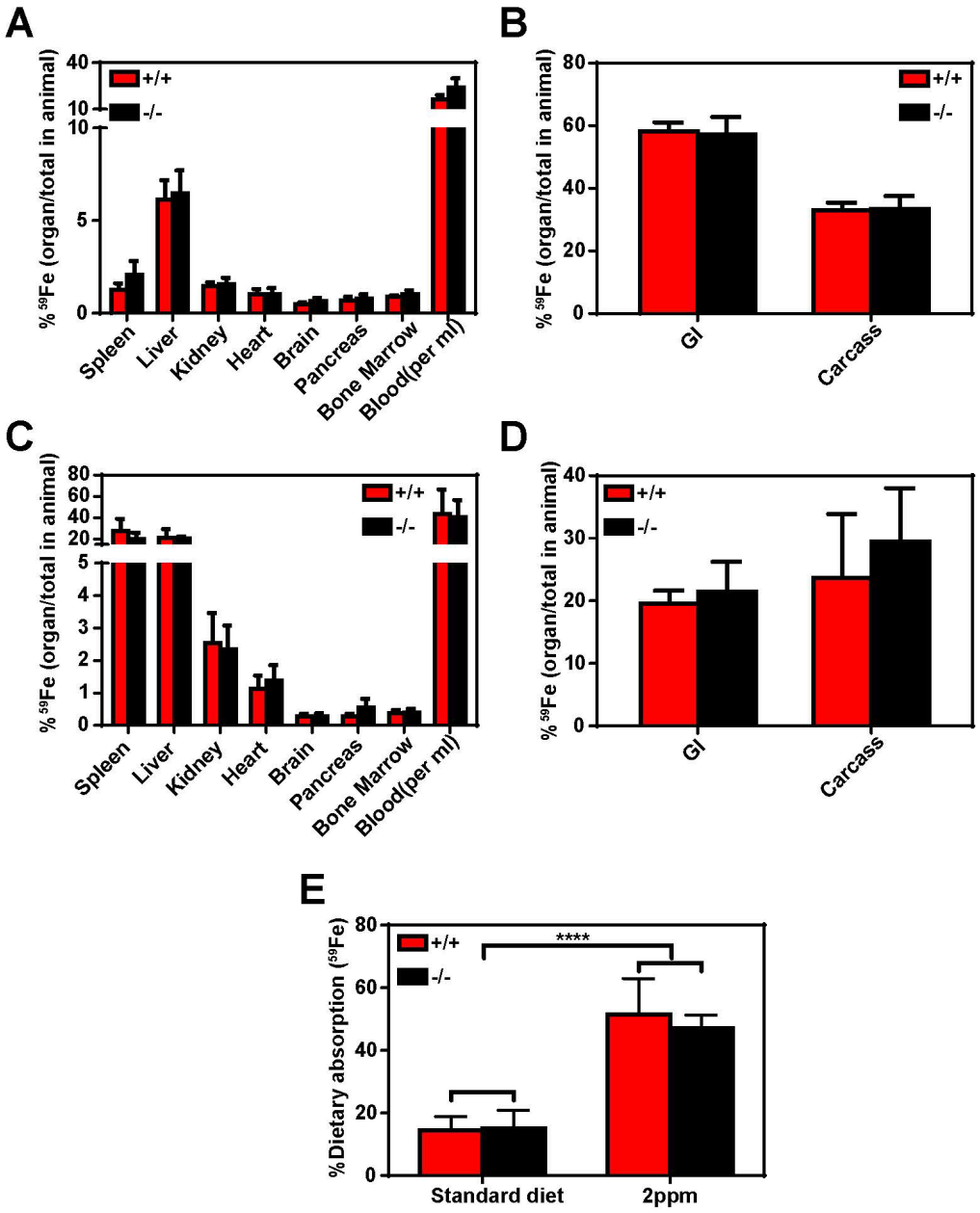

Figure 4.14 Intestinal iron absorption and distribution is not significantly altered in the absence of HRG1

Distribution of dietary ^{59}Fe in the spleen, liver, kidney, heart, brain, pancreas, bone marrow, blood, gastrointestinal (GI) tract, and carcass of mice on a **(A, B)** standard or **(C, D)** low-iron diet. Counts were measured 24 h post gavage of ^{59}Fe. **(A, B)** n=6 per

genotype; **(C, D)** n=3 per genotype. **(E)** Percentage dietary iron absorption calculated by the ^{59}Fe retained within the entire animal over the amount of ^{59}Fe gavaged. ****p<0.0001.

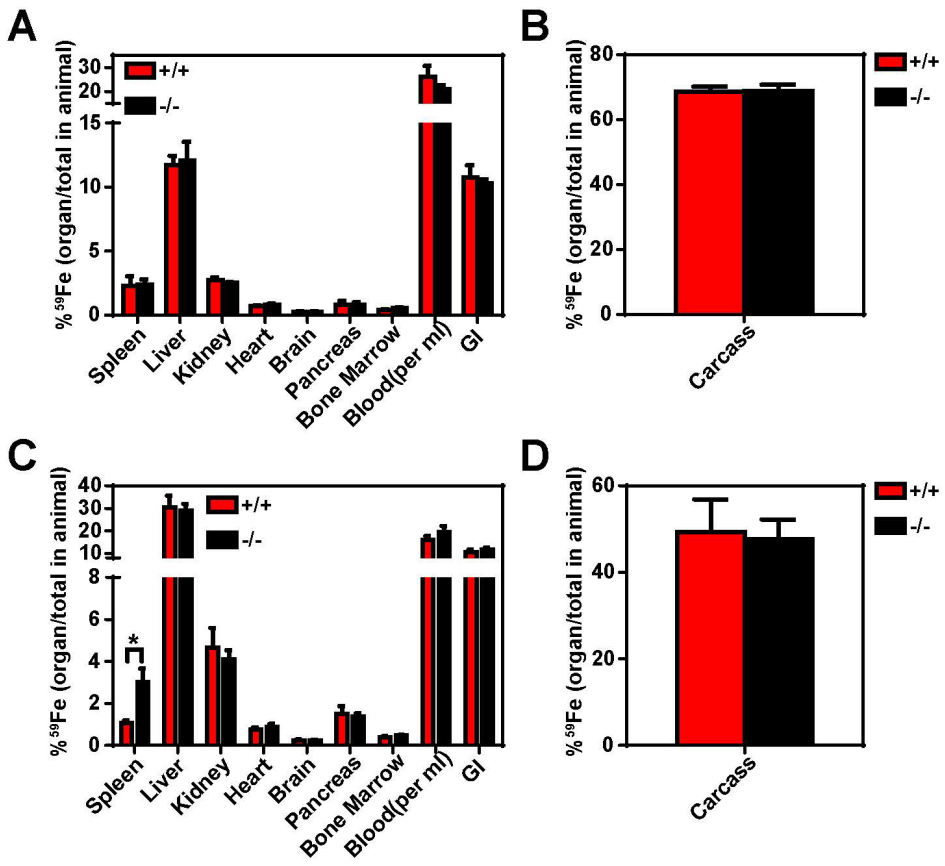

Figure 4.15 Serum iron distribution is altered in *HRG1*$^{-/-}$ mice

Distribution of intravenously (IV) administered ^{59}Fe in the spleen, liver, kidney, heart, brain, pancreas, bone marrow, blood, gastrointestinal (GI) tract, and carcass of mice on a standard diet through **(A, B)** transferrin-bound iron or **(C, D)** non-transferrin-bound iron. **(A, B)** n=3 per genotype; **(C, D)** n=6 per genotype. Counts were measured 24 h post IV administration of 59Fe.

*p<0.05.

Discussion

Since daily iron requirement is composed of both dietary and recycled iron, we hypothesized that the impacts of ineffective heme-iron recycling in *HRG1*$^{-/-}$ mice were compensated by greater absorption of dietary iron. Through ^{59}Fe metabolic uptake studies, we observed no differences in dietary iron absorption in *HRG1*$^{+/+}$ and *HRG1*$^{-/-}$ mice. To further understand the potential severity of ineffective heme-iron recycling by HRG1, we placed *HRG1*$^{+/+}$ and *HRG1*$^{-/-}$ mice on a moderate (10 ppm) and low-iron (2 ppm) diet. Both diets led to *HRG1*$^{-/-}$ mice having significantly reduced hematocrits and when placed on the low-iron diet for long-term, *HRG1*$^{-/-}$ mice were unable to sustain erythropoiesis, resulting in death. Analyses of iron-deficient mice with similar hematocrits at week 5 revealed that *HRG1*$^{-/-}$ mice were unable to induce stress erythropoiesis effectively. Gene expression analyses suggested that the pathways that allow for an iron-deficiency stress response were aberrantly regulated in *HRG1*$^{-/-}$ mice, as these mice continued to experience tissue iron overload through hemozoin accumulation. It therefore appears that in the absence of *HRG1*, there is disconnect between the tissue iron status and systemic iron status, resulting in a contradictory genetic response to iron-deficiency. *HRG1*$^{-/-}$ mice also appeared to accumulate more hemozoin during iron-deficiency, despite having no observable differences in erythrocyte lifespan. Unexpectedly, *HRG1*$^{-/-}$ mice on a standard diet showed enhanced partitioning of NTBI but not TBI to the spleen. As there is stress erythropoiesis occurring in the spleens of *HRG1*$^{-/-}$ mice under normal conditions showing an increase in immature erythroid population of cells, this could suggest that NTBI could be the preferred source of iron during early stages of splenic

erythropoiesis. NTBI is a chelatable pool of iron in the plasma that believed to be a major contributor to tissue iron loading and related pathologies in iron overload disorders[8,203]. Studies have shown that the main organs of NTBI clearance are the liver, followed by the pancreas and kidney. NTBI uptake is mediated by NTBI transporters including ZIP14, ZIP8, T-type calcium channels, DMT1, and TRPC6[10,204]. While there is evidence of a ZIP14-independent NTBI uptake by the spleen, the exact mechanism of splenic NTBI transport is not well understood.

Chapter 5 : Role of *HRG1* in intestinal heme transport

Summary

Iron-deficiency affects more than two billion people in the world and manifests as anemia[205]. It is one of the most common diet-related disorder and can be remedied in most cases by iron supplementation[206]. Heme is a major dietary source of iron as it is more readily absorbed than inorganic iron in the human intestine[11,12]. As mentioned previously, the intestinal heme transporter remains elusive. While a mouse model lacking intestinal HRG1 appears to be a suitable model, studies in mice reveal no significant dietary heme uptake, indicating that mice may be an inappropriate model to evaluate intestinal heme absorption[207]. Some potential caveats are strain differences in mice as most genetic mutations are in the C57BL/6J background which contains a genetic variant in *MON1a*, resulting in a defect in endosomal protein trafficking[208], and *NRAMP1*, the phagosomal divalent metal transporter; and that heme is imported by murine enterocytes but not exported from the basolateral surface, a concept recently underscored by the observation that *HMOX1* expression is upregulated when mice are fed heme-rich diet but they remain anemic[207]. Here, we present preliminary results for two alternate model systems - Caco-2 cells, a human intestinal cell line, and piglets to study intestinal heme absorption. Using Caco-2 cells, we show that *HRG1* expression is regulated by heme and localizes to subapical or apical compartments in polarized cells. *HRG1*-knockout Caco-2 cells, generated using CRISPR-Cas9, are unable to upregulate *HMOX1* induction upon heme exposure. Furthermore, we show that heme-supplemented diet is unable to rescue anemia in iron-deficient 21-day old piglets while diet supplemented with RBCs

reverse anemia. Together, these results suggest that there is a mechanism for intestinal heme absorption and HRG1 may play a role in intestinal heme absorption.

Results

Generation of *HRG1*-knockout Caco-2 cells

As observed in macrophages, HRG1 expression is upregulated by exogenous heme in the colonic adenocarcinoma cell line Caco-2 TC7 clone **(Fig. 5.1A)** but not in the Bbe or HTB-37 clones **(Fig. 5.1B, C)**. Hence, we decided to focus on the TC7 clone to generate *HRG1*-knockout cells by CRISPR-Cas9. Using guide RNAs targeted to exon 1 (E1), exon 2 (E2) and exon 3 (E3) of *SLC48A1* (encoding HRG1) **(Fig. 5.2A)**, we obtained four clones that showed no detectable HRG1 protein **(Fig. 5.2B)**, and DNA sequencing revealed the precise genetic lesion in *SLC48A1* within each clone (**Table 5-1**, **APPENDIX X**). Subsequent characterization of *HRG1*-knockout Caco-2 cells was conducted using the E1 and E1+E3 #1 clones. When wildtype and *HRG1*-knockout Caco-2 cells transduced with lentiviral *HRG1-GFP* were polarized, HRG1 intracellular localization changed from vesicular membranes **(Fig. 5.3C)** to an apical or sub-apical localization **(Fig. 5.3A, B, D)**.

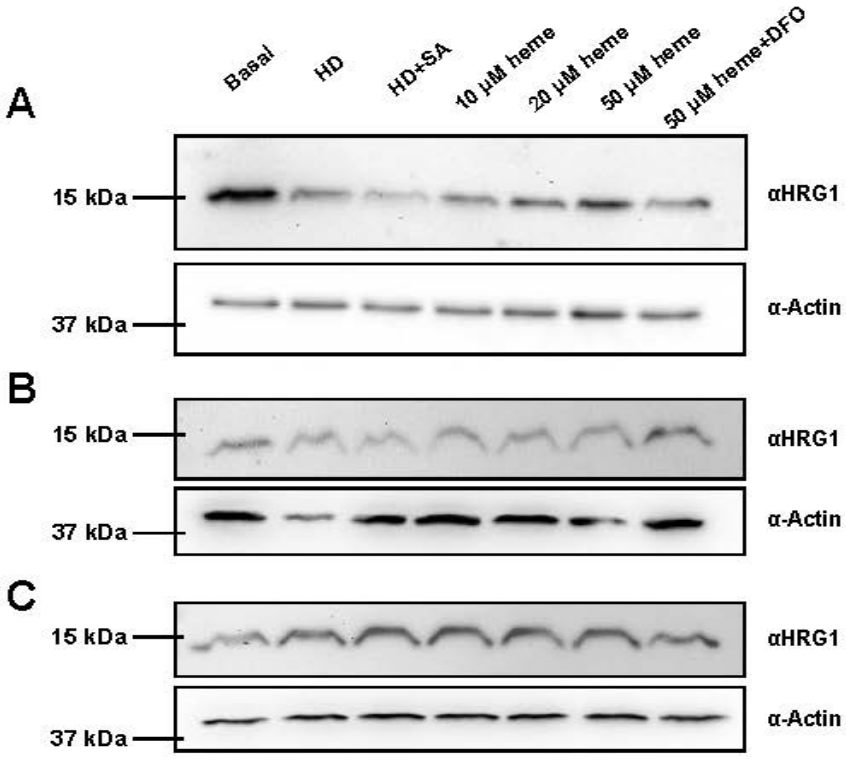

Figure 5.1 HRG1 expression changes to heme treatment in different Caco-2 cell clones

HRG1 expression in **(A)** TC7, **(B)** Bbe and **(C)** HTB-37 Caco-2 cells via immunoblotting.Cells were treated with basal, heme depleted (HD), HD with succinyl acetone (SA), and different concentrations of heme with deferroxamine (DFO) for 24 hours prior to the analyses.

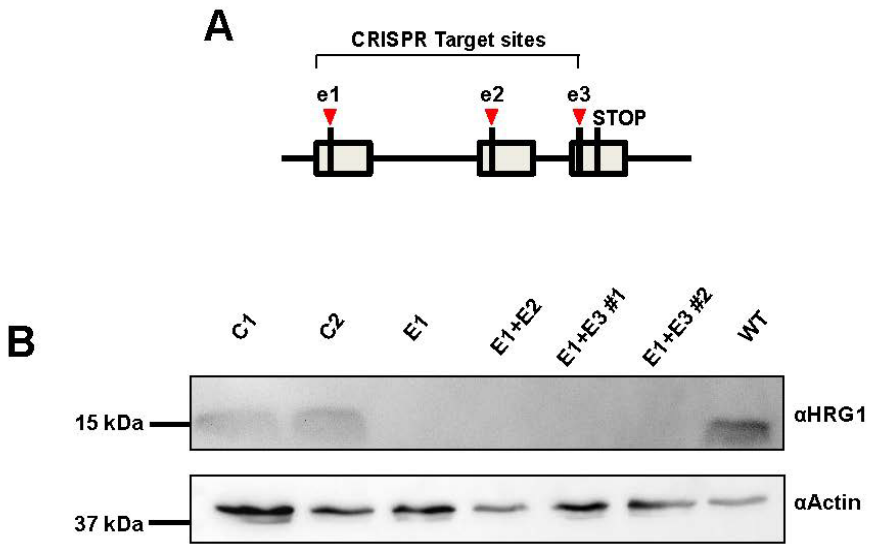

Figure 5.2 Generation of *HRG1*-knockout Caco-2 cells

(A) Gene loci of *HRG1* indicating the CRISPR target sites in exon 1, 2 and 3.

(B) Immunoblots of *HRG1*-knockout Caco-2 clones.

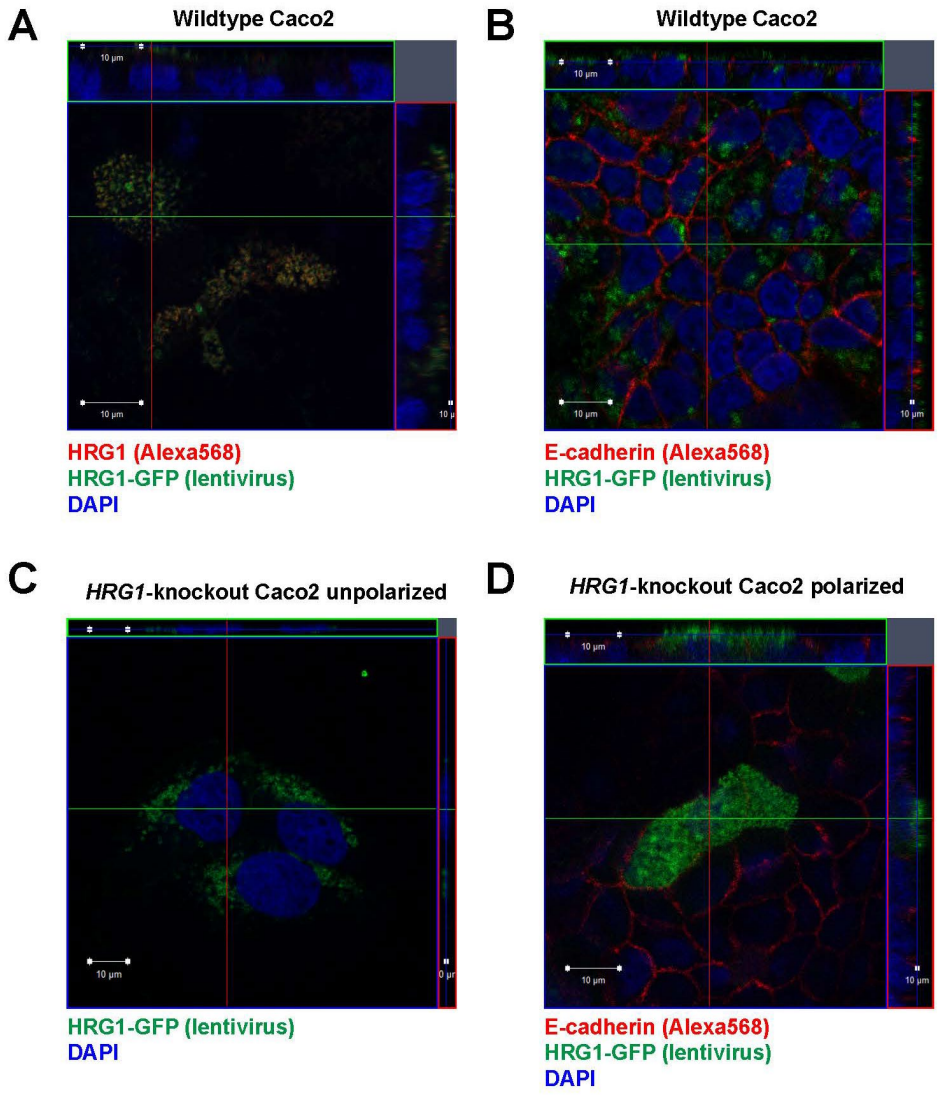

Figure 5.3 HRG1 localization in polarized and unpolarized wildtype and *HRG1*-knockout Caco-2 cells

(A, B) Confocal images of polarized wildtype Caco-2 cells transduced with HRG1-GFP lentivirus and with immunofluorescence of HRG1 or E-cadherin.

(C) Confocal image of unpolarized *HRG1*-knockout Caco-2 cells transduced with HRG1-GFP lentivirus.

(D) Confocal image of polarized *HRG1*-knockout Caco-2 cells transduced with HRG1-GFP and with immunofluorescence of E-cadherin.

Table 5-1. Summary of *HRG1*-knockout Caco-2 clones

Clone	**Genotype**	**Protein**
C1 (Control)	WT	Present
C2 (Control)	WT	Present
E1	1 nucleotide indel	Absent
E1+E2	Deletion (E1 to E2)	Absent
E1+E3 #1	Deletion (E1 to E3)	Absent
E1+E3 #2	Deletion (E1 to E3)	Absent

HRG1$^{-/-}$ Caco-2 cells show lower induction of *HMOX1* by heme

In non-polarized cells, *HMOX1* is reduced in the absence of *HRG1* when compared to wildtype cells **(Figure 5.4A, B)**. A similar result was observed in polarized cells when heme was added to the basolateral side of the growth medium **(Fig. 5.5A, B)**. Although this is surprising, this result is consistent with previous studies in which polarized Caco-2 cells induce *HMOX1* by basolateral heme supplementation[209].

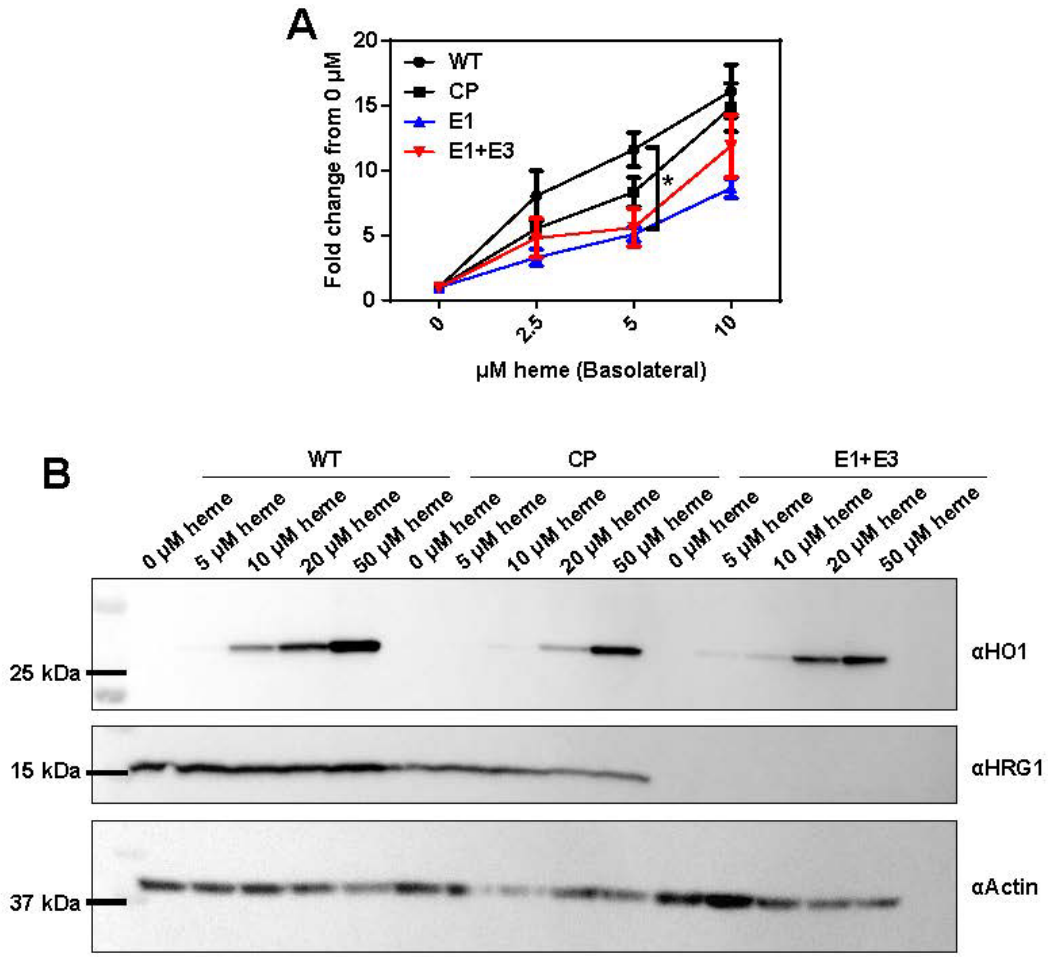

Figure 5.4 *HMOX1* induction by heme treatment is suppressed in unpolarized *HRG1*-knockout Caco-2 cells

(A) *HMOX1* gene expression (normalized to housekeeping gene actin) by qPCR

(B) *HMOX1* protein expression by immunoblotting in wildtype (WT), control-pooled(CP), E1 *HRG1*-knockout and E1+E3 *HRG1*-knockout unpolarized Caco-2 cells treated with heme for 24 hours. CP cells were cells that were transfected with Cas9 but no guideRNA; i.e. they retain wildtype levels of HRG1 protein and no mutations in *HRG1* gene loci.

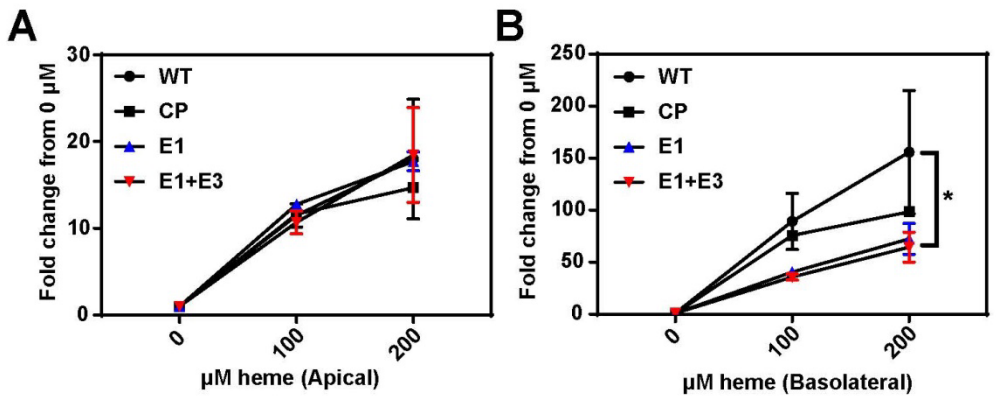

Figure 5.5 *HMOX1* gene expression induction by heme is suppressed in polarized *HRG1*-knockout Caco-2 cells

(A, B) *HMOX1* gene expression by qPCR in wildtype (WT), control-pooled(CP), E1 *HRG1*-knockout and E1+E3 *HRG1*-knockout polarized Caco-2 cells treated with heme from the apical or basolateral surface for 24 hours. *p<0.05.

Pigs express HRG1 throughout intestinal tract

Pigs appear to be a good model to study dietary heme absorption for various reasons. Firstly, studies have shown that pigs absorb heme via a specific mechanism[210]. The gastrointestinal (GI) tract of pigs also most closely resembles that of humans as compared to other non-primate models[211]. More importantly, nursing pigs reared in confinement suffer from iron-deficiency anemia. Piglets are born with a total body iron concentration of about 20 ppm, but as the sow's milk is extremely low in iron (3 ppm), body iron stores cannot sustain the growth needs of piglets[212]. By three-weeks of age, piglets typically experience a growth spurt, quadrupling their birth weight. The anemia of piglets therefore provides a natural biomarker of dietary heme-iron absorption and utilization. Finally, the knowledge that pigs express HRG1 throughout their GI tract was pivotal in choosing this animal model[213].

Hematocrits of iron-deficient pigs are partially rescued by hemoglobin-containing diet

To observe the effects of a purified hemin-supplemented diet on iron-deficient piglets, we conducted a study with 21-day old iron-deficient piglets that were fed either an iron-deficient diet, hemin-supplemented diet, or an iron-supplemented diet. From our first study with 21-day old piglets, over a four-week period, a diet containing purified hemin was unable to rescue iron-deficiency anemia in contrast to iron-sulfate **(Fig. 5.6A, B)**. Hemoglobin and hematocrit were used as measures of anemia. However, when the hemin-fed anemic piglets were switched to a porcine RBC-supplemented diet, anemia was rescued within two weeks **(Fig. 5.6C, D)**. (The hematological parameters were collected by Ms. Elda Kwong in the Hamza Lab). By hemin extraction and ICP analysis, we now know that 87% of the total iron in RBCs

was contained in hemin. Subsequent analyses of HRG1 protein expression in pig intestinal tissues did not show obvious patterns of regulation by diet, possibly due to the switching of diets after four-weeks, even though HRG1 was found to be expressed in pig spleen, liver and throughout the intestinal tract **(Fig. 5.7)**. Furthermore, immunolocalization studies in duodenal enterocytes of piglets have shown that HRG1 localization changed to mostly apical membranes in response to hemoglobin-enriched diet[213], raising the possibility that changes in HRG1 protein localization may be more relevant than total steady-state levels.

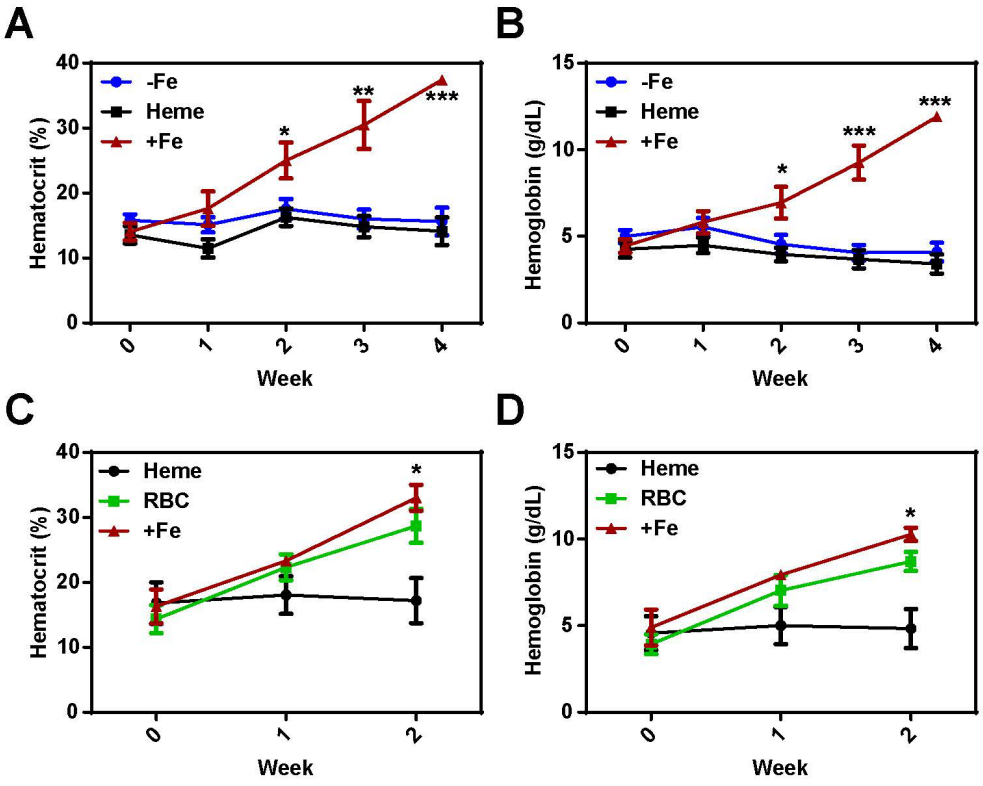

Figure 5.6 Dietary hemin does not rescue iron-deficiency anemia in pigs

(A, B) Hematocrit and hemoglobin levels in 21-day old piglets that were fed an iron-deficient (-Fe), iron-sufficient (+Fe) or hemin-supplemented (heme) diet. n=5 per group. At the end of 4 weeks, the (n=3) iron-deficient pigs were transferred to a RBC-supplemented diet.

(C, D) Hematocrit and hemoglobin levels in pigs fed with RBC-supplemented diets over 2 weeks. Statistical significance represent differences in treatment groups versus +Fe group. *p<0.05; **p<0.01; ***p<0.001.

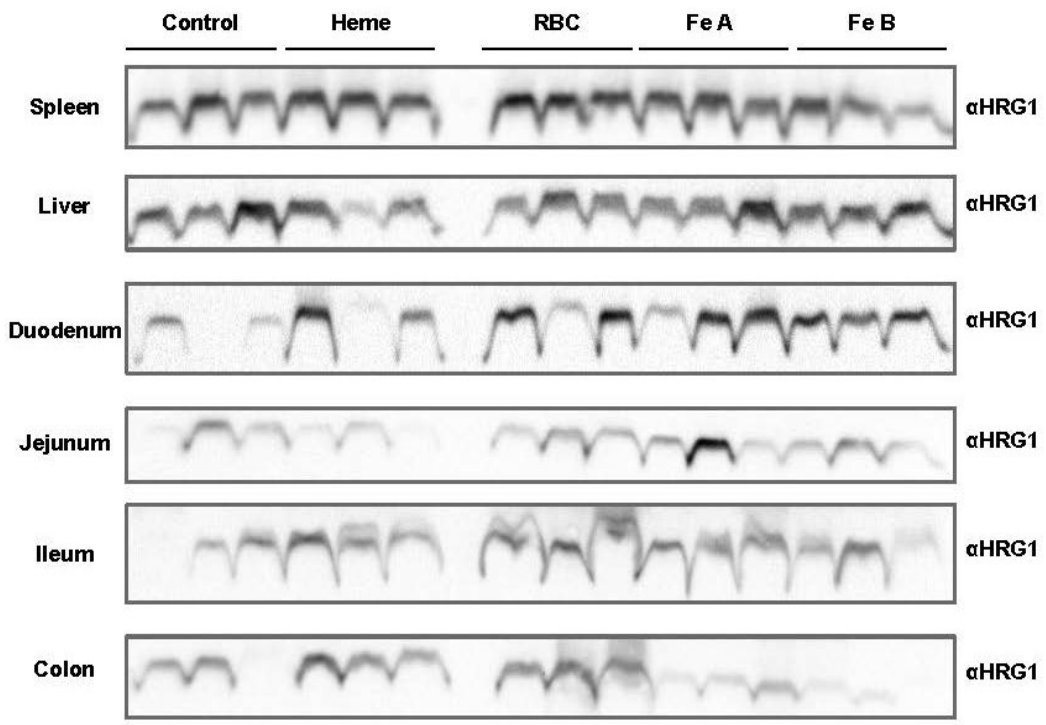

Figure 5.7 Expression of HRG1 in different piglet tissues corresponding to diets fed

Immunoblots of HRG1 in crude membrane preparations from spleens, liver, duodenum, jejunum, ileum and colon of piglets fed different diets. Fe A indicates piglets that were fed an iron-deficient diet and sacrificed at week 4, while Fe B represents piglets that were sacrificed at the end of the 6 week study. Ponceau stainings of each immunoblotting membrane can be found in **APPENDIX XI**.

Discussion

Multiple reports have alluded to a potential "receptor-mediated" mechanism for intestinal heme absorption in mammals[15]. However, the laboratory mouse, which is highly genetically tractable, has been proven to be unsuitable for the investigation of dietary heme absorption as they do not appear to utilize heme as a dietary source of

iron[207]. Our attempts to study the role of *HRG1* as an intestinal heme transporter utilizing human intestinal cell lines and piglets as a whole-animal model show promising preliminary results. Consistent with the subcellular locations of the duodenal iron importer DMT1[214], HRG1 was observed to localize to the apical side of polarized Caco-2 cells, which suggests a function for HRG1 and heme transport from the lumen via the apical surface of intestinal epithelial cells. Although *HRG1*-knockout Caco-2 cells also showed attenuated induction of *HMOX1* with hemin treatments, the hemin application was from the basolateral surface. This is unexpected as heme uptake should occur from the apical side facing the lumen. Potential explanations for this result is the use of hemin instead of a dietary-form of heme or that *HMOX1* induction is dictated by systemic/circulatory levels of heme and that in the absence of *HRG1*, *HMOX1* function is attenuated. Therefore, further studies using bioavailable forms of heme, such as hemoglobin or heme complexed to smaller peptides, has to be conducted with polarized *HRG1*-knockout Caco-2 cells to evaluate the impact of *HRG1*-deficiency. Fluorescent heme analogs such as zinc mesoporphyrin may also be applied to the apical surface of polarized wildtype and *HRG1*-knockout Caco-2 cells and imaged using confocal microscopy to observe differences in intracellular heme absorption. Iron-deficient weanling piglets appeared to be a suitable model for dietary heme absorption studies and it is concluded that dietary heme absorption requires a form of bioavailable heme such as hemoglobin found in RBCs even though intestinal epithelial HRG1 steady-state abundance did not change in response to diets or anemia. Future studies are required to elucidate the mechanisms for intestinal heme absorption in iron-deficient piglets.

Chapter 6 : Conclusions and future directions

Conclusions

HRG1 was first identified in the heme auxotroph *Caenorhabditis elegans* [215] and later shown to play a role in mammalian heme transport in bone marrow-derived macrophages during erythrophagocytosis. *HRG1* has also been implicated in erythropoiesis and heme-iron recycling in zebrafish[174]. The goal of this project was to understand the physiological impact(s) of *HRG1* loss in a mammalian *in vivo* model and to investigate if *HRG1* plays a role in intestinal heme transport. The major findings of this project are summarized below:

1) Loss of *HRG1* in mice results in systemic heme-iron overload, particularly in reticuloendothelial tissues (spleen, liver, bone marrow). Using differential extraction of heme, ICP-MS and UPLC, we observed tissue iron accumulation in the form of heme. Corresponding to heme-iron overload, serum ferritin levels are also elevated in *HRG1*$^{-/-}$ mice.
2) *HRG1*-deficiency in mice results in ineffective heme-iron recycling by splenic and liver erythrophagocytic macrophages. *In vivo* recycling of ^{59}Fe-labelled RBCs show increased retention of ^{59}Fe in the form of heme and an insoluble heme pigment in *HRG1*$^{-/-}$ spleens and livers, indicating a defect in heme transport in the recycling process.
3) Sequestered heme from phagocytosed RBCs accumulates in the form of hemozoin within lysosomes of *HRG1*$^{-/-}$ macrophages. Hemozoin, an inert crystalline heme molecule, localizes within enlarged LAMP1^{+} vesicles in macrophages of the spleen, liver and bone marrow.

4) *In vivo* macrophage depletion by inducing apoptosis with clodronate releases hemozoin, which accumulates within interstitial spaces in the liver. Released hemozoin does not translocate to the kidney but is instead released from the spleen and accumulates in the liver.
5) *HRG1*$^{-/-}$ mice contain fewer splenic red pulp macrophages and greater numbers of maturating monocytes. The decrease in red pulp macrophages could be due to heme toxicity as *HRG1*$^{-/-}$ mice contain significantly more heme in the spleen.
6) Ineffective erythroblast maturation from basophilic to polychromatic stage in *HRG1*$^{-/-}$ mice results in reduced RBC production and significantly lower hematocrits. While other hematological parameters of the *HRG1*$^{-/-}$ mice are normal, the reduction in RBC production suggests a role for HRG1 in erythropoiesis.
7) *HRG1*$^{-/-}$ mice experience extramedullary erythropoiesis in the spleen, corresponding to ineffective bone marrow erythropoiesis. This is accompanied by significantly higher serum transferrin levels, which are typically indicative of systemic iron-deficiency.
8) Under prolonged dietary iron limitation, *HRG1*$^{-/-}$ mice are unable to maintain erythropoiesis and experience severe iron-deficiency anemia. This is a consequence of restricted dietary iron compounded by a block in recycling of heme-iron due to *HRG1*-deficiency. In addition, *HRG1*$^{-/-}$ mice are unable to induce a splenic stress erythropoiesis response to iron-deficiency and suffer from severe ineffective bone marrow erythroblastic maturation.

9) *HRG1*-deficiency results in an aberrant response to iron-deficiency. Spleen hepcidin, a potential regulator of systemic iron metabolism, was insufficiently suppressed in *HRG1*$^{-/-}$ mice during iron-deficiency. Moreover, 30% of the 90 iron metabolism genes assessed was significantly different in *HRG1*$^{-/-}$ spleens with more than 10 genes that were involved in the hepcidin regulation pathway.

10) Despite tissue heme-iron overload and signs of iron-deficiency, *HRG1*$^{-/-}$ mice have similar overall tissue distribution of dietary iron and TBI. However, non-transferrin bound-iron (NTBI) was observed to accumulate in *HRG1*$^{-/-}$ spleens, suggesting the preference of NTBI as a source of iron for extramedullary erythropoiesis.

11) *HRG1* may also function as an intestinal heme transporter. In polarized Caco-2 human intestinal cell lines, HRG1 localizes to the subapical region in vesicles. This is in contrast to the punctate vesicular localization of HRG1 in macrophages and non-polarized Caco-2 cells. It suggests that membrane trafficking of HRG1 is dictated by cell polarization, and that heme transport by HRG1 in macrophages after digestion of senescent RBCs may share common molecular mechanisms with heme transport by HRG1 in enterocytes after digestion of dietary hemoproteins.

12) Iron-deficiency anemia is rescued by hemoglobin-supplemented diet in piglets but not by purified hemin. These results indicate that there exists a mechanism for intestinal heme-absorption through hemoglobin and the absorbed heme-iron is bioavailable for erythropoiesis.

Future directions

Systemic consequences of hemozoin accumulation

Superficially, the accumulation of hemozoin in *HRG1*$^{-/-}$ mice appears to have no physiological impacts. However, several studies have shown that hemozoin from *Plasmodium* or β-hematin causes inflammatory responses[187]. Therefore, it is possible that hemozoin in *HRG1*$^{-/-}$ mice are causing systemic inflammatory responses that have not been analyzed. To address this, we could measure the levels of inflammatory cytokines in the serum or lymph nodes. It is possible that *HRG1*$^{-/-}$ mice have adapted to hemozoin accumulation and needed to be challenged. We could accomplish this by infecting them with parasites or bacteria and study the efficacy of immune responses to pathogens in the absence of *HRG1* and presence of hemozoin.

Mechanism of mammalian hemozoin formation

As this is the first instance of mammalian hemozoin formation, whether the formation is an active enzymatic process or a chemical process is not known. To gain insights into possible target proteins that may be involved in hemozoin formation (if any), we could conduct protein analyses via mass spectrometry and compare *HRG1*$^{+/+}$, *HRG1*$^{-/-}$ hemozoin-containing and *HRG1*$^{-/-}$ non-hemozoin containing lysosomes extracted from the respective macrophages. Identifying differentially expressed proteins would provide a list of genes that we could genetically manipulate *in vivo* to determine whether hemozoin formation is altered in *HRG1*$^{-/-}$ mice. These analyses can be conducted concurrently with RNA-sequencing of the same samples to identify potential genes for hemozoin-formation.

Lysosomal integrity in *HRG1*$^{-/-}$ macrophages

We observed that *HRG1*$^{-/-}$ macrophages contain hemozoin-laden LAMP1^{+}-vesicles which are significantly larger than the previously reported sizes of lysosomes. With the enlargement of these membrane compartments, it is possible that the lysosomal membrane is compromised and prone to leakage or breakage, as reported in lysosomal storage diseases. It is also possible that HRG1, a lysosomal membrane protein, aids in maintaining membrane integrity. Hence, we could investigate the impacts of 1) loss of *HRG1* and 2) hemozoin accumulation or the combination of both on lysosomal membrane integrity. Through *in vitro* studies involving either naïve BMDMs or mature hemozoin-laden macrophages, we can measure lysosomal leakage through pH sensitive probes or recruitment of lysosomal damage proteins known to repair lysosomes. This can be done in both unperturbed conditions or under erythrophagocytosis where reorganization of the membranes and cytoskeleton is involved.

Oxidative status in response to *HRG1*-deficiency

Our preliminary analyses suggest that there is more heme in the non-hemozoin form in *HRG1*$^{-/-}$ tissues. We can confirm the location of this heme at the cellular level, by using heme-sensors[1] that are targeted to various intracellular compartments in *HRG1*-deficient macrophages after EP. If it is indeed true that *HRG1*$^{-/-}$ cells are exposed to more labile heme, the impacts of this labile heme should be investigated. Heme and iron are both known to cause oxidative stress through reactive oxygen species. To investigate this, we can analyze the oxidative status of *HRG1*$^{-/-}$ tissues or specific cell types through measurements of oxidative stress

markers such as gluthathione disulfide (GSSG) and gluthathione (GSH) levels or Nrf2, a signaling molecule which can induce oxidative stress responses. These measurements can also be done using *in vitro* cultured bone marrow macrophages and treating them with opsonized RBCs, to determine whether macrophages are exposed to more oxidative stress during erythrophagocytosis and in the absence of *HRG1*. A similar approach could be performed with phagocytosis of purified mammalian hemozoin or intracellular pathogens such as *mycobacterium tuberculosis*.

Role of *HRG1* in erythropoiesis

HRG1$^{-/-}$ mice show ineffective erythropoiesis with more immature erythroblasts at the basophilic stage than *HRG1*$^{+/+}$ mice. From the mouse cell atlas[216], HRG1 expression is found in both erythroblasts and macrophages within the bone marrow. This suggests a role for *HRG1* not only in erythrophagocytic macrophages, but potentially nurse macrophages and erythroblasts for erythroblast maturation. To delineate the roles of *HRG1* in erythropoiesis, we could utilize cell-specific ablation of *HRG1* in mice. The first potential model would be a macrophage-specific *HRG1*-deletion and the second is a RBC-specific *HRG1*-deletion. The combination of these two mouse models would be able to give us insights into the relative contribution of cell-specific *HRG1* on the ineffective erythropoiesis we observe in our current model of *HRG1*-deficiency. In addition, we could conduct erythroblast maturation analyses *in vitro* by isolating either entire erythroblastic islands or hematopoietic stem cells and differentiating them into RBCs in the presence or absence of nurse macrophages.

Protein interactions of HRG1 for heme transport

The current model for erythrophagocytosis follows the fate of heme as it is transported out of the phagolysosome by HRG1 into the cytosol where HMOX1 can catabolize heme to liberate iron. Since HMOX1 was not observed to localize to the phagolysosomal membrane[107], the interacting proteins required for heme transport in this process is not known. To identify potential interactors of HRG1, which may act as a chaperone for heme, we can conduct an immunoprecipitation of HRG1 followed by mass spectrometry such as the Multidimensional Protein Identification Technology (MudPIT)[217]. This can be conducted using *in vitro* cultured macrophages before, during and after erythrophagocytosis. By comparing the three time-points, we will be able to identify proteins whose interactions with HRG1 are enhanced by erythrophagocytosis. By shRNA-knockdown of these potential interactors *in vitro* and observing if heme metabolism is altered, we can identify targets that are required for heme recycling post-erythrophagocytosis.

Role of *HRG1* in intestinal heme absorption

While laboratory strains of mice may be an inappropriate animal model to study *in vivo* heme absorption, we can exploit *HRG1*-knockout Caco-2 cells to perform cell biological studies and heme-uptake assays with ^{59}Fe-heme. In addition, we can utilize 3D cell culture of intestinal organoids derived from either human induced pluripotent stem cells (iPSCs) or duodenal crypt cells from piglets[218]. We can generate *HRG1*-knockout cells through CRISPR-Cas9, which provides a 3D intestinal model to study heme absorption. We can use these models to conduct heme uptake assays and measure downstream target genes of heme such as *HMOX1*, or

immunofluorescence using fluorescent heme analogs like zinc-mesoporphyrin (ZnMP).

Significance

As previously mentioned, most genetic ablations of proteins involved in the heme-iron metabolism has proven to result in embryonic lethality thus far. Only approximately 10% of *HMOX1*-null animals survive and the surviving animals do not have reticuloendothelial macrophages in their spleen, liver, bone marrow, and develop iron-deficiency anemia in old age with kidney iron overload[137]. *In vitro* differentiated *HMOX1*$^{-/-}$ bone marrow macrophages die with erythrophagocytosis due to heme toxicity. *Ferroportin*-null mice are embryonic lethal due to developmental defects and selective inactivation of *FPN* in the embryo resulted in iron accumulation in macrophages, hepatocytes and enterocytes[219]. *FLVCR*-null animals lack definitive erythropoiesis and die *in utero*, while neonatal deletion of *FLVCR* results in a development of macrocytic anemia and iron overload in macrophages[18,93]. *Ferritin*-null mice are also lethal during embryonic development due to the lack of ferroxidase activity by the H subunit[220]. Our studies described herein show that *HRG1*-deficiency is not embryonic lethal, but results in ineffective heme recycling by macrophages. This inability to transport heme out of the phagolysosome leads to the formation of hemozoin, which to our knowledge, is the first instance of mammalian hemozoin. This discovery highlights an important aspect of mammalian cells - that they do have a heme tolerance mechanism by polymerizing heme into inert hemozoin in the phagolysosome. The conditions of lysosomes also appear to be similar to the conditions of the food vacuole of *Plasmodium* in which hemozoin forms. The

formation of hemozoin in the absence of *HRG1* makes *HRG1* a potential therapeutic target in hemolytic diseases in which the macrophages are overwhelmed with high levels of intracellular toxic heme. Thus, selective inhibition of *HRG1* during a hemolytic crisis, as in sickle cell disease, could be beneficial to overcome cellular cytotoxicity.

Our nutritional studies in *HRG1*$^{-/-}$ mice combined with the genetic analysis of iron metabolism genes in the spleen, liver and kidney also highlights a few ideas:

1) Tissue iron levels affect gene expression profiles which dictate the overall responses to systemic iron levels

HRG1$^{-/-}$ iron-deficient mice were unable to suppress iron-regulated genes unlike *HRG1*$^{+/+}$ mice. This inability to appropriately regulate iron metabolism genes corresponded to their inability to enhance splenic erythropoiesis to increase erythrocyte production under iron-deficient conditions. Therefore, *HRG1*$^{-/-}$ mice maintained on a low-iron diet were susceptible to severe iron-deficiency anemia which led to death. We postulate that the accumulation of heme-iron resulted in the misperception of systemic iron overload, corresponding to elevated serum ferritin in *HRG1*$^{-/-}$ mice.

2) Recycled iron as a sole source of iron can sustain life in mice

HRG1$^{+/+}$ mice developed iron-deficiency anemia on an iron-limiting diet but continued to maintain their hematocrit up to 20-weeks with no lethality. These anemic animals appeared to be able to adapt to a systemic iron-deficient condition and sustain erythropoiesis relying solely on recycled iron as a source.

Finally, our combined preliminary results using Caco-2 cells and piglets suggest that

1) There is an active mechanism for dietary heme absorption, and

2) HRG1 localizes to the apical/sub-apical surface in polarized intestinal epithelial cells and HRG1 may be involved in regulating intracellular heme levels in enterocytes.

Chapter 7 Appendices

APPENDIX I

APPENDIX I. Guide RNA sequences for human HRG1 (*Slc48a1*)

gRNA name	Target	Notes	fwd (extra G) CACC	rev AAAC
hSLC48e1	GGTAGACCACCGTCCAGACGAGG	reverse	CACCGGTAGACCACCGTCCAGACG	AAACCGTCTGGACGGTGGTCTACC
hSLC48e2	TGTACATCACGTGCGTCACCAGG	reverse	CACCGTGTACATCACGTGCGTCACC	AAACGGTGACGCACGTGATGTACAC
hSLC48e3	AAAGTCAGCCCGGTAGCGGTGGG	reverse	CACCGAAAGTCAGCCCGGTAGCGGT	AAACACCGCTACCGGGCTGACTTTC

APPENDIX II

APPENDIX II. List of primers used for qPCR of Caco-2 cells

Primer	Sequence
hActin forward	GGCATGGGTCAGAAGGATT
hActin reverse	AGGTGTGGTGCCAGATTTTC
hHO1 forward	AGACGGCTTCAAGCTGGTGAT
hHO1 reverse	CCTTGTTGCGCTCAATCTCCT
hHO2 forward	GAAGGAAGGGACCAAGGAAG
hHO2 reverse	CTCCTCGAGGGCTGAGTATG

APPENDIX III

APPENDIX III. X-ray diffraction pattern of purified hemozoin from *HRG1*$^{-/-}$ mice

Top: Powder x-ray diffraction of purified insoluble fraction from *HRG1*$^{-/-}$ spleens (red: measured data; dark blue: calculated pattern; light blue: background; green: structural plot).

Bottom: Chemical structure of hemozoin from *HRG1*$^{-/-}$ mice

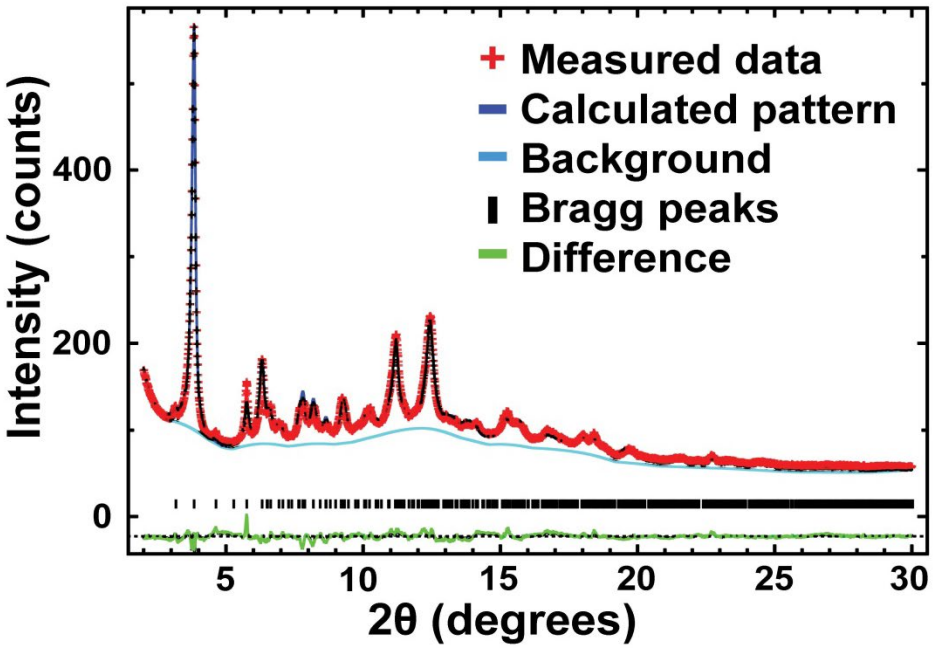

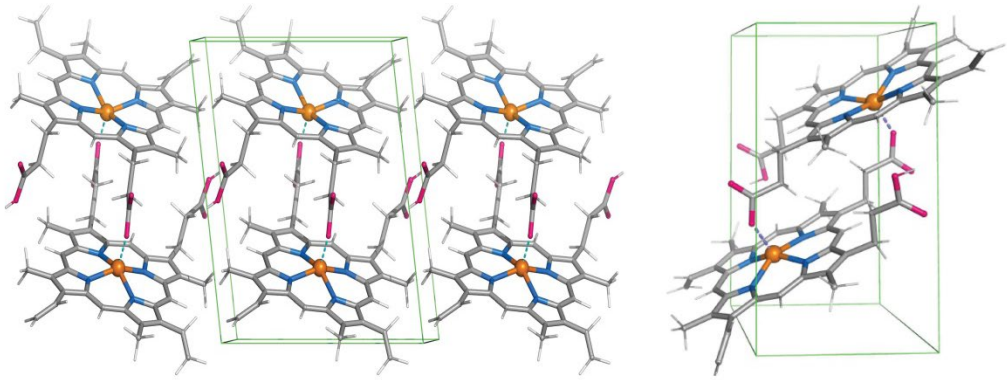

APPENDIX IV

APPENDIX IV. Scanning electron microscopy (SEM) images of *Plasmodium* hemozoin and hemozoin derived from *HRG1*$^{-/-}$ reticuloendothelial tissues.

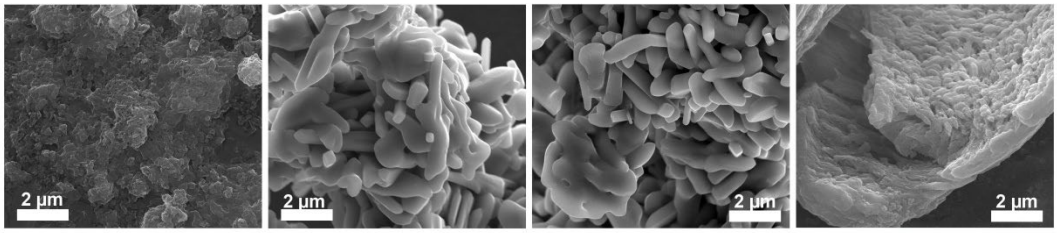

APPENDIX V

APPENDIX V. Transmission electron microscopy images of *HRG1*$^{+/+}$ and *HRG1*$^{-/-}$ isolated bone marrow and splenic macrophages

Transmission electron microscopy (TEM) of F4/80^{+} bone marrow and splenic macrophages from *HRG1*$^{+/+}$ and *HRG1*$^{-/-}$ mice. At least 3 cells were imaged per genotype. Yellow arrows point to membranes surrounding hemozoin particles.

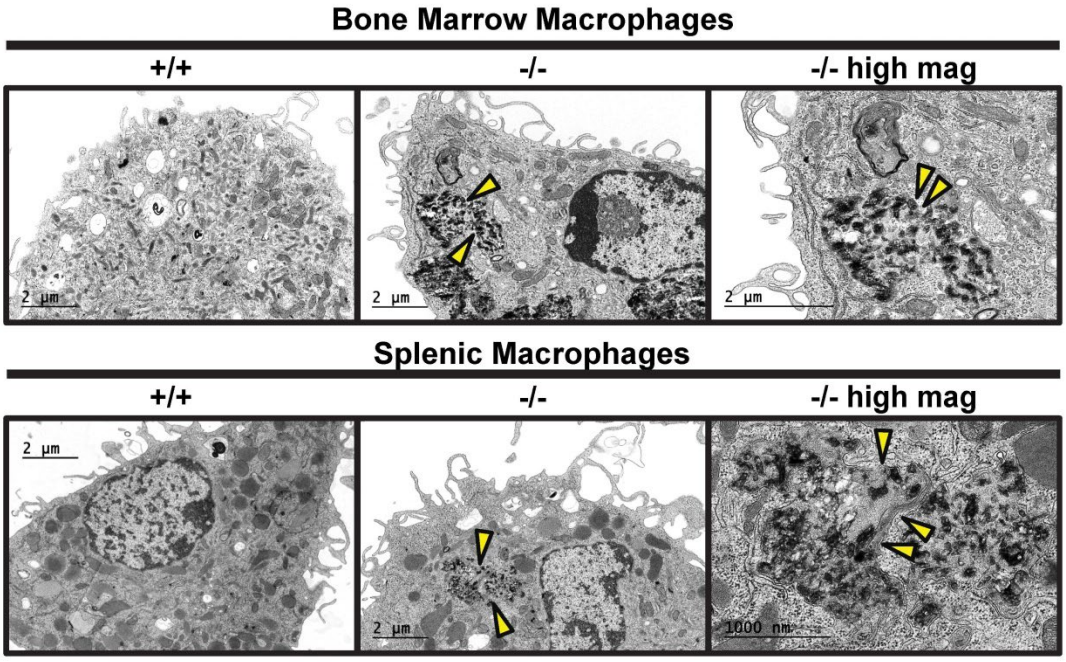

APPENDIX VI

APPENDIX VI. Transmission electron microscopy images of *HRG1*$^{+/+}$ and *HRG1*$^{-/-}$ *in vitro* differentiated macrophages and isolated monocytes

TEM of *in vitro*-differentiated bone marrow macrophages and isolated bone marrow monocytes. At least 3 cells were imaged per genotype.

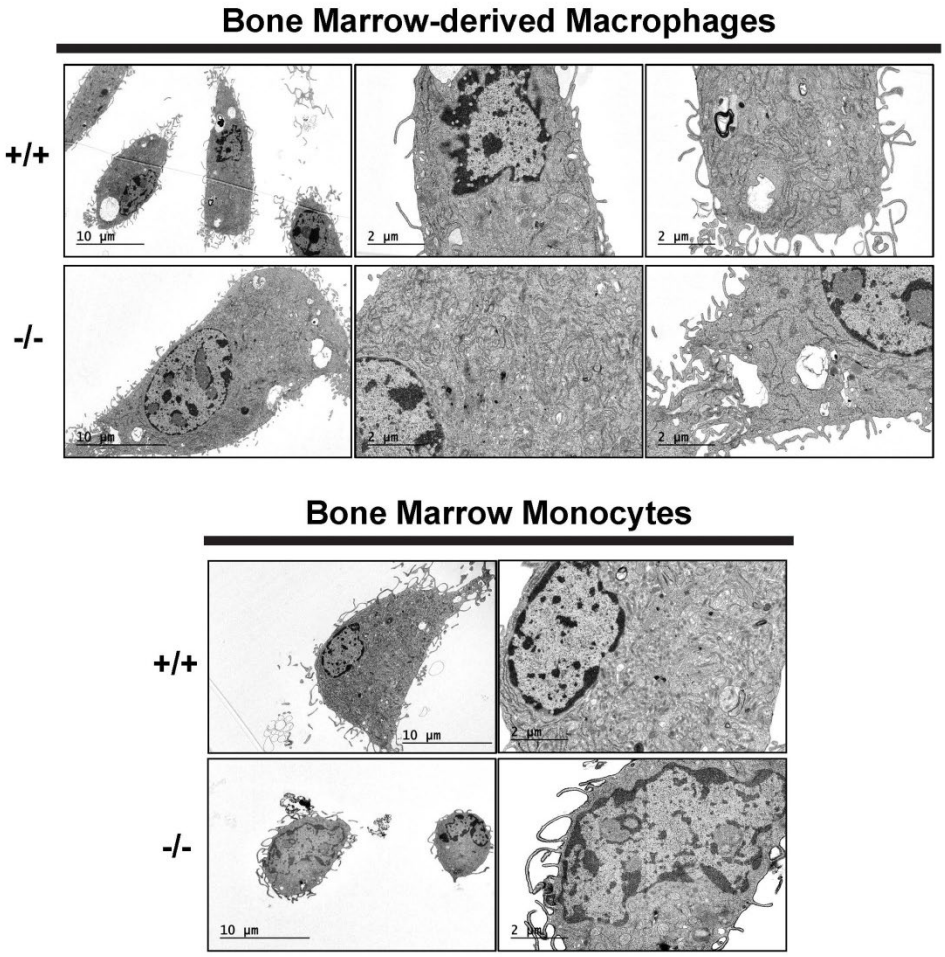

APPENDIX VII

APPENDIX VII. X-ray fluorescence microscopy of F4/80^{+} bone marrow macrophages from *HRG1*$^{+/+}$ and *HRG1*$^{-/-}$ mice.

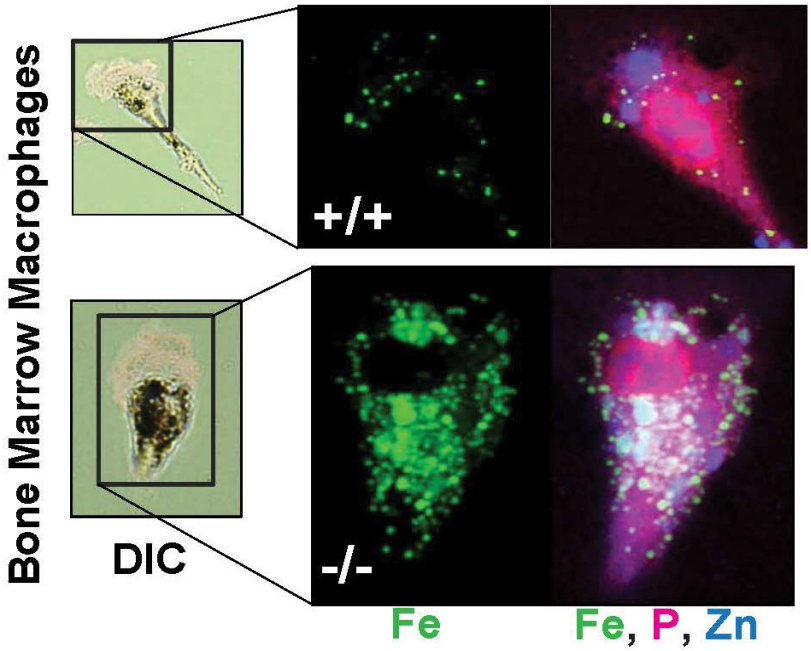

APPENDIX VIII

APPENDIX VIII. Quantification of total cellular concentrations of indicated elements.

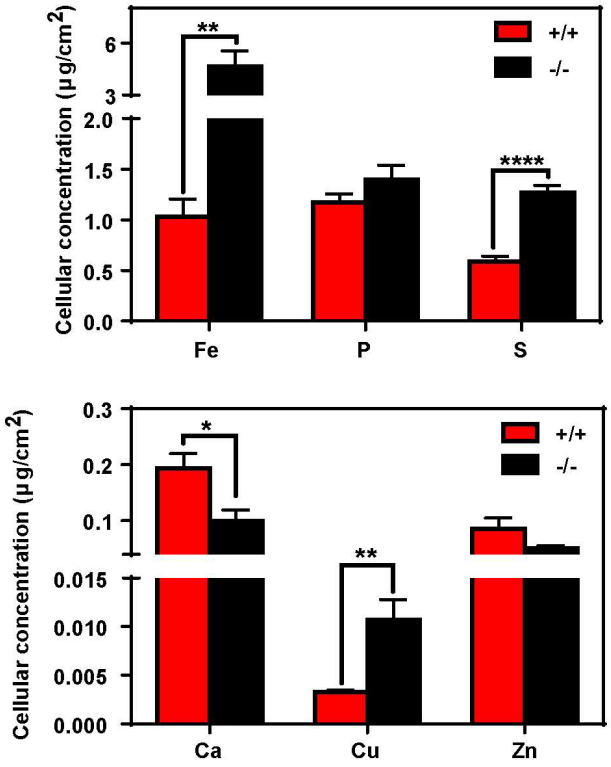

APPENDIX IX

APPENDIX IX. ROI concentration within hemozoin-laden areas in *HRG1*$^{-/-}$ BMMs.

Quantifications were measured for n=5 cells per genotype. *p<0.05; **p<0.01; ***p<0.001; ****p<0.0001

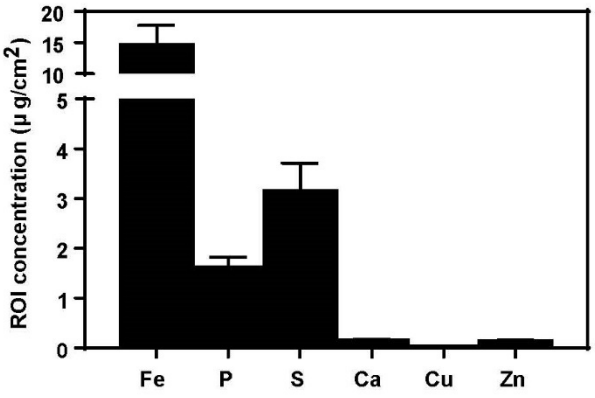

APPENDIX X

APPENDIX X. Sequencing of *HRG1*-knockout Caco-2 clones

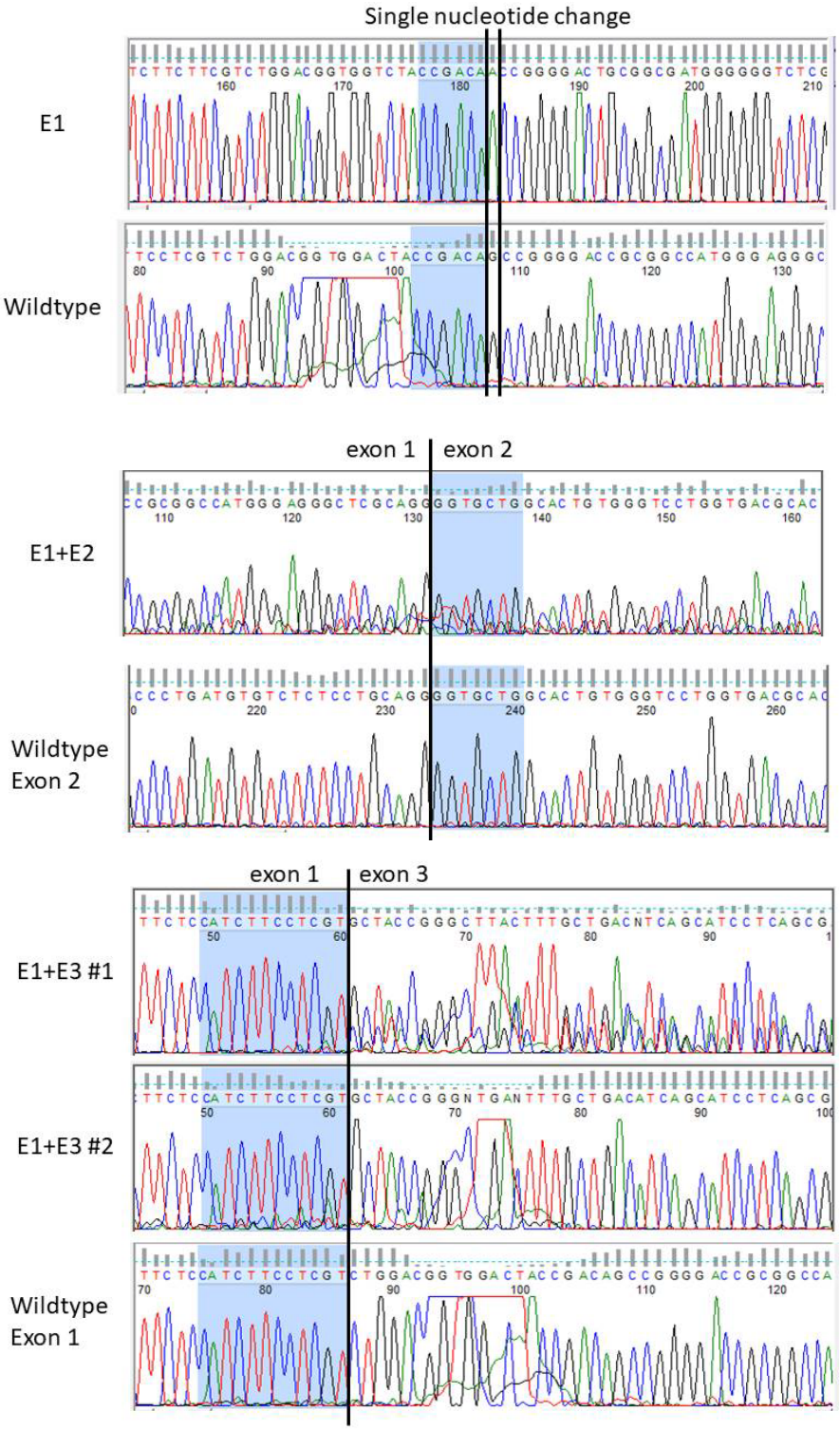

APPENDIX XI

APPENDIX XI. Ponceau stainings of immunoblotting membranes of pig tissues (membrane prep)

Spleen

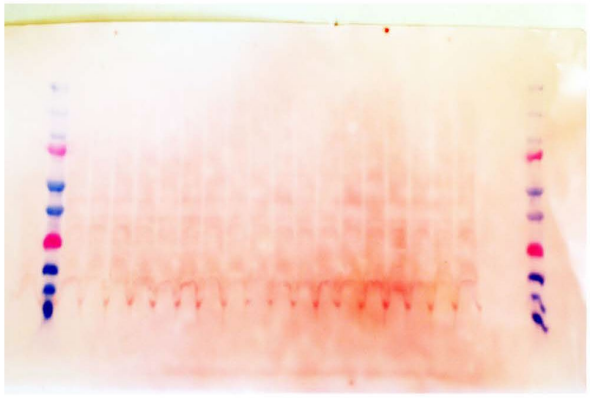

Duodenum

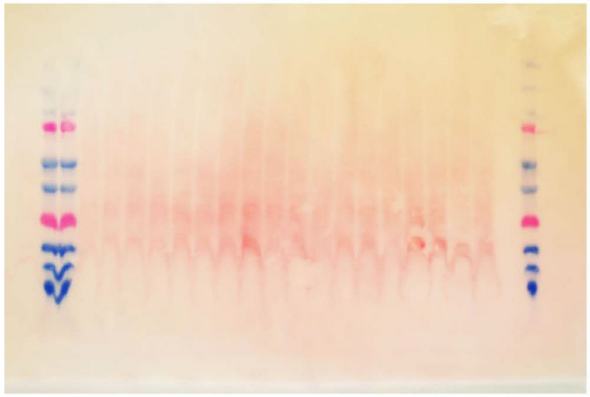

Jejunum

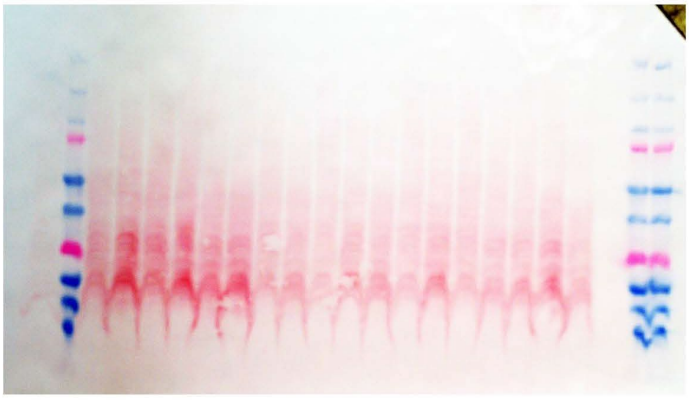

ileum

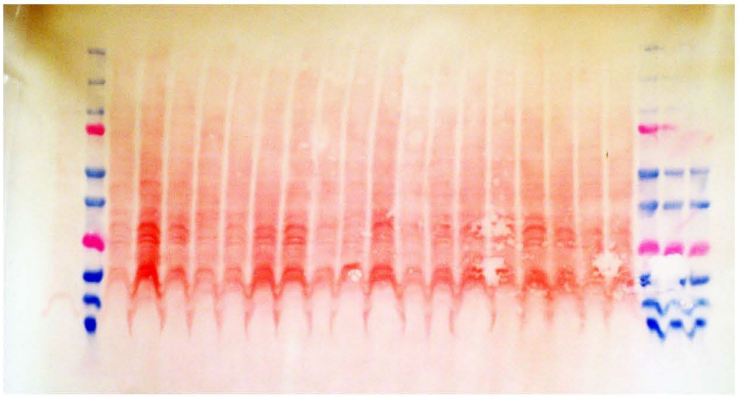

Colon

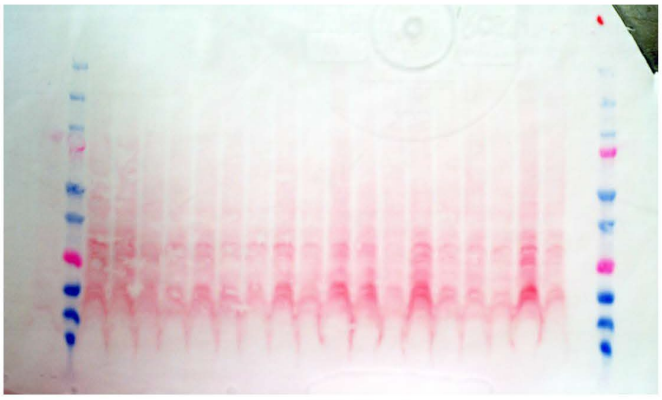

APPENDIX XII

APPENDIX XII. Expression profile of 90 iron metabolism genes in spleen

Spleen							
	Gene name	Gene expression (2^(-ΔCt))				p-value	
		HRG1+/+ Standard	HRG1-/- Standard	HRG1+/+ 2ppm	HRG1-/- 2ppm	+/+ vs -/- Standard	+/+ vs -/- 2ppm
1	Ncoa4	0.460228	0.45156	0.677581	0.654086	0.785908	0.910494
2	Ankrd37	0.077148	0.06764	0.042022	0.078109	0.203337	0.082088
3	Smad7	0.076842	0.086016	0.021828	0.046165	0.274171	0.11449
4	Neo1	0.008445	0.00909	0.004881	0.012302	0.65851	0.001396
5	Mfsd7b	0.04416	0.040798	0.021812	0.036406	0.446136	0.056827
6	Steap3	0.009364	0.008803	0.043108	0.03235	0.683205	0.675788
7	Alas2	0.015192	0.013973	0.137159	0.114733	0.606314	0.844622
8	Steap2	0.007771	0.008065	0.003611	0.008499	0.860607	0.00879
9	Pcbp2	1.44205	1.489302	1.396467	1.437742	0.673885	0.83502
10	Slc39a8	0.008971	0.010366	0.034527	0.018045	0.338525	0.259762
11	Slc39a14	0.023129	0.022927	0.007918	0.015392	0.938729	0.086934
12	Hmox2	0.132777	0.122484	0.067796	0.112948	0.353423	0.074152
13	Slc11a2	0.07238	0.071503	0.132895	0.097686	0.856884	0.317352
14	Il12a	0.054078	0.047771	0.017265	0.040463	0.315652	0.100251
15	Heph	0.007771	0.008065	0.003892	0.010382	0.860607	0.00032
16	Fbxl5	0.424975	0.393218	0.183384	0.370833	0.223873	0.020012
17	Slc38a1	0.245817	0.22301	0.103132	0.195156	0.23564	0.054551
18	Cp	0.149606	0.123381	0.053151	0.130496	0.040584	0.050688
19	Nox4	0.007771	0.008065	0.003604	0.008499	0.860607	0.008779
20	Trfr2	0.008191	0.008065	0.015932	0.011385	0.937299	0.431137
21	Tlr7	0.070707	0.06133	0.027631	0.076642	0.329741	0.05663
22	Alas1	0.051966	0.047865	0.034113	0.051883	0.41855	0.087581
23	Aco1	0.034538	0.029939	0.027705	0.033004	0.104746	0.164952
24	Bmp6	0.008986	0.009215	0.004589	0.013405	0.867165	0.00041
25	Epo	0.007771	0.008065	0.003604	0.008499	0.860607	0.008779
26	Fech	0.073222	0.061787	0.355397	0.316257	0.257168	0.85321
27	Fxn	0.039113	0.040464	0.082965	0.055555	0.666486	0.159952
28	Ifnab	0.02035	0.013281	0.007811	0.017754	0.258808	0.110244
29	Il1b	0.032794	0.0297	0.023154	0.03559	0.623479	0.262454
30	Lcn2	0.008039	0.008065	0.020481	0.036683	0.987727	0.339753
31	Smad4	0.666844	0.634719	0.224429	0.472095	0.528873	0.081848
32	Trim27	0.44057	0.409639	0.400956	0.39193	0.363565	0.84778
33	Saa1	0.007771	0.008431	0.003604	0.008499	0.686138	0.008779
34	Stat6	0.011246	0.012675	0.00548	0.012844	0.310895	0.006443

35	Epas1	0.118297	0.122453	0.063605	0.126695	0.715891	0.085056
36	Fth1	8.27107	7.823645	12.10742	10.12592	0.550265	0.231022
37	Ftl1	3.051175	3.167726	2.439446	3.152218	0.621149	0.09736
38	Gast	0.007771	0.008065	0.003604	0.008499	0.860607	0.008779
39	Ggh	0.061242	0.069158	0.041502	0.062903	0.270486	0.142022
40	Herc2	0.323256	0.301078	0.273275	0.268044	0.354969	0.869643
41	Hfe	0.027479	0.023567	0.018634	0.036539	0.363139	0.037129
42	Hif1a	0.144096	0.12521	0.06031	0.10897	0.081934	0.156598
43	Hmox1	0.061712	0.052363	0.066466	0.150277	0.452103	0.057685
44	Id1	0.038423	0.041967	0.024664	0.045018	0.662734	0.100576
45	Ifna2	0.01001	0.009491	0.005368	0.012305	0.850758	0.041967
46	Ifna4	0.007771	0.008065	0.003759	0.008499	0.860607	0.008373
47	Ifnb1	0.008262	0.008599	0.003884	0.008853	0.852075	0.010902
48	Il10	0.007771	0.008065	0.003604	0.008846	0.860607	0.004212
49	Il1a	0.018561	0.019324	0.01921	0.024782	0.773414	0.344068
50	Nos2	0.586098	0.501664	0.31465	0.559412	0.762478	0.182222
51	Spic	0.075424	0.071478	0.066295	0.104985	0.57783	0.269443
52	Stat3	0.354791	0.341432	0.142882	0.287183	0.595846	0.099515
53	Tfrc	0.0931	0.099157	0.602722	0.2551	0.554229	0.225457
54	Pcbp1	0.682598	0.465519	0.631387	0.73657	0.308162	0.202
55	Eif2ak1	0.123477	0.111092	0.276118	0.17224	0.220474	0.209149
56	Slc11a1	0.019358	0.017986	0.014885	0.028003	0.580363	0.092705
57	Neu3	0.028821	0.027812	0.060246	0.053327	0.835653	0.667419
58	Slc40a1	0.083922	0.095411	0.166625	0.28874	0.384726	0.179292
59	Il22	0.007771	0.008065	0.003604	0.008499	0.860607	0.008779
60	Hp	0.007771	0.008065	0.007638	0.013376	0.860607	0.047671
61	Hpx	0.007771	0.008065	0.003604	0.008595	0.860607	0.007156
62	Pcbp4	0.009495	0.012202	0.004643	0.010652	0.020129	0.003501
63	Pcbp3	0.012452	0.012558	0.006289	0.01225	0.961568	0.027975
64	Ireb2	0.200697	0.205773	0.137189	0.161649	0.721662	0.372345
65	Ndfip1	0.31997	0.296984	0.159203	0.292991	0.268846	0.069558
66	Glrx3	0.303586	0.295483	0.199801	0.284397	0.756802	0.12322
67	Cisd2	0.046779	0.041849	0.034236	0.03579	0.519249	0.70719
68	Slc25a37	0.184587	0.180537	0.716806	0.481279	0.769777	0.500716
69	Slc48a1	0.154751	0.122308	0.247154	0.231763	0.023006	0.795474
70	Asb11	0.007771	0.008065	0.00373	0.008499	0.860607	0.011532
71	Hfe2	0.007771	0.008065	0.003604	0.009815	0.860607	0.000626
72	Steap1	0.007771	0.008065	0.003604	0.008639	0.860607	0.00791
73	Tmprss6	0.007771	0.008065	0.003604	0.008561	0.860607	0.007936
74	Cybrd1	0.010012	0.01606	0.005803	0.011169	0.240113	0.116958
75	Il6	0.007771	0.008065	0.003604	0.008949	0.860607	0.003406

76	Tlr9	0.18901	0.175538	0.065271	0.162854	0.559203	0.091765
77	Hamp	0.007771	0.008065	0.003604	0.008499	0.860607	0.008779
78	Steap4	0.009093	0.009466	0.005369	0.009517	0.844773	0.086015
79	Aco2	0.281366	0.271247	0.275595	0.268562	0.587524	0.778817
80	Tlr3	0.015441	0.015644	0.007944	0.018626	0.946068	0.027149
81	Cisd1	0.068871	0.065689	0.064531	0.059389	0.651308	0.417664
82	Slc25a38	0.007771	0.008065	0.004564	0.008499	0.860607	0.051437
83	Slc25a28	0.090025	0.085501	0.051173	0.076466	0.605732	0.113797
84	Nox1	0.007771	0.008065	0.003605	0.008499	0.860607	0.008795
85	Fam132b	0.02599	0.026918	0.127975	0.10671	0.83357	0.76172
86	Bola2	0.921033	0.942639	0.696702	0.956523	0.764892	0.068752
87	Nox3	0.007771	0.008065	0.003604	0.008499	0.860607	0.008779
88	Slc11a2	0.027327	0.036439	0.039777	0.03899	0.159956	0.950754
89	Slc11a2	0.062631	0.060864	0.091422	0.059077	0.80646	0.126955
90	Iscu	0.844944	0.813611	0.853614	0.975764	0.703808	0.477372

APPENDIX XIII

APPENDIX XIII. Expression profile of 90 iron metabolism genes in liver

Liver							
	Gene name	Gene expression (2^(-ΔCt))				p-value	
		HRG1+/+ Standard	HRG1-/- Standard	HRG1+/+ 2ppm	HRG1-/- 2ppm	+/+ vs -/- Standard	+/+ vs -/- 2ppm
1	Ncoa4	2.104806	2.054607	1.840099	1.519775	0.842456	0.010102
2	Ankrd37	0.026956	0.029494	0.085682	0.074238	0.686342	0.526779
3	Smad7	0.045746	0.060019	0.042773	0.045979	0.088687	0.718038
4	Neo1	0.088618	0.085184	0.079316	0.084068	0.623462	0.697684
5	Mfsd7b	0.033904	0.0287	0.034737	0.029811	0.278941	0.486382
6	Steap3	0.282205	0.379398	0.259662	0.211577	0.086504	0.301235
7	Alas2	0.738493	0.827988	0.578526	0.659839	0.479046	0.605066
8	Steap2	0.049261	0.045718	0.079847	0.083476	0.590147	0.782351
9	Pcbp2	2.472163	2.660609	2.80595	2.293929	0.551858	0.040291
10	Slc39a8	0.47985	0.515413	0.442933	0.463886	0.568555	0.698327
11	Slc39a14	1.113893	1.281578	1.196207	1.240187	0.243892	0.749833
12	Hmox2	0.500969	0.557152	0.547028	0.518539	0.23307	0.525405
13	Slc11a2	0.266538	0.245697	0.402017	0.37846	0.51679	0.585676
14	Il12a	0.006174	0.006711	0.006229	0.005119	0.648028	0.155095
15	Heph	0.012257	0.012459	0.011403	0.010497	0.925382	0.65044
16	Fbxl5	0.330613	0.292015	0.326683	0.318606	0.306851	0.83004
17	Slc38a1	0.009863	0.009664	0.013854	0.012196	0.858419	0.58464
18	Cp	11.18418	11.29099	9.244314	10.39812	0.91491	0.361235
19	Nox4	0.301777	0.369597	0.31618	0.232075	0.092537	0.254908
20	Trfr2	1.397556	1.488136	1.472023	1.308716	0.534117	0.257797
21	Tlr7	0.011021	0.013092	0.021151	0.024298	0.357052	0.576796
22	Alas1	2.448702	2.371844	3.160594	2.155087	0.937472	0.12928
23	Aco1	1.474099	1.462684	1.302615	1.191635	0.954875	0.612794
24	Bmp6	0.026047	0.031494	0.011476	0.009744	0.217314	0.512344
25	Epo	0.006174	0.006711	0.006229	0.005119	0.648028	0.155095
26	Fech	1.327336	1.405528	1.272371	1.251952	0.658019	0.908706
27	Fxn	0.358537	0.367927	0.352618	0.32621	0.776755	0.458308
28	Ifnab	0.017581	0.026947	0.014468	0.019398	0.213494	0.506078
29	Il1b	0.061586	0.069314	0.102627	0.061808	0.72544	0.139748
30	Lcn2	0.267921	0.128132	0.29268	0.464611	0.267906	0.5562
31	Smad4	0.772931	0.71437	0.779715	0.86016	0.512164	0.508856
32	Trim27	0.488392	0.486109	0.474558	0.432887	0.954172	0.297162
33	Saa1	4.429164	2.245883	2.858346	3.647674	0.406544	0.754409
34	Stat6	0.013739	0.014096	0.011708	0.011772	0.863464	0.968186

35	Epas1	1.147802	1.351177	1.687153	1.768037	0.217485	0.708785
36	Fth1	46.97091	48.5549	49.69345	40.89033	0.792539	0.181332
37	Ftl1	46.89152	42.25637	28.7884	32.36782	0.390758	0.393369
38	Gast	0.006174	0.006711	0.006229	0.005119	0.648028	0.155095
39	Ggh	0.285346	0.29256	0.323914	0.260677	0.83938	0.059112
40	Herc2	0.35564	0.382736	0.383258	0.344749	0.384618	0.262309
41	Hfe	0.561019	0.530981	0.488806	0.465035	0.683101	0.5818
42	Hif1a	0.246592	0.26424	0.241707	0.270835	0.50479	0.283897
43	Hmox1	0.104365	0.1158	0.192946	0.141604	0.592594	0.151771
44	Id1	0.060124	0.070904	0.070147	0.062814	0.265836	0.739887
45	Ifna2	0.009547	0.018035	0.010855	0.011244	0.010002	0.899766
46	Ifna4	0.006703	0.006711	0.006229	0.007456	0.994363	0.62851
47	Ifnb1	0.00675	0.009052	0.007154	0.00677	0.081153	0.678612
48	Il10	0.006174	0.006711	0.006229	0.005119	0.648028	0.155095
49	Il1a	0.085707	0.089735	0.081813	0.061604	0.788144	0.064725
50	Nos2	0.304159	0.436781	0.207065	0.229652	0.412871	0.89302
51	Spic	0.01849	0.015979	0.042308	0.041677	0.268166	0.957923
52	Stat3	1.169194	1.134505	1.087231	1.269853	0.823213	0.14194
53	Tfrc	0.238403	0.221555	0.775859	0.853378	0.672732	0.600141
54	Pcbp1	1.997149	1.983349	1.84455	1.876354	0.952889	0.902948
55	Eif2ak1	0.38162	0.400133	0.373302	0.38837	0.694657	0.742811
56	Slc11a1	0.028851	0.026178	0.054541	0.055204	0.627299	0.944282
57	Neu3	0.041021	0.032129	0.038816	0.043619	0.134109	0.576291
58	Slc40a1	0.968484	0.996529	0.999023	1.065346	0.854911	0.766943
59	Il22	0.006174	0.006711	0.006229	0.005119	0.648028	0.155095
60	Hp	35.0992	27.749	32.50427	39.64732	0.296094	0.440617
61	Hpx	69.92164	56.03077	57.41014	71.38555	0.17532	0.210616
62	Pcbp4	0.048157	0.06004	0.044817	0.050902	0.160598	0.454102
63	Pcbp3	0.009664	0.010573	0.009489	0.010926	0.543752	0.312287
64	Ireb2	0.827994	0.76695	0.717796	0.781823	0.51992	0.493991
65	Ndfip1	2.190142	2.236745	2.057999	1.917441	0.866357	0.575084
66	Glrx3	1.133977	1.141158	1.237516	1.032026	0.952871	0.141758
67	Cisd2	0.09629	0.102094	0.107751	0.113297	0.725393	0.689943
68	Slc25a37	0.207294	0.225136	0.194363	0.198761	0.563322	0.896901
69	Slc48a1	0.510877	0.319351	0.438605	0.268671	0.004204	0.004492
70	Asb11	0.006174	0.006742	0.012435	0.008084	0.628657	0.524463
71	Hfe2	1.412205	1.495065	1.893776	1.434467	0.674471	0.083435
72	Steap1	0.006195	0.008248	0.007112	0.007579	0.107006	0.600925
73	Tmprss6	1.199311	1.215268	1.141207	1.143271	0.936316	0.992596
74	Cybrd1	0.007649	0.015536	0.009117	0.012143	0.010447	0.37467
75	Il6	0.006174	0.006711	0.006627	0.005119	0.648028	0.077788

76	Tlr9	0.006821	0.007646	0.007404	0.007786	0.441323	0.733958
77	Hamp	9.515957	19.43472	0.006229	0.009745	0.192934	0.116914
78	Steap4	0.984624	0.965356	0.826565	0.967361	0.942259	0.525285
79	Aco2	1.86685	2.084105	2.463018	1.978878	0.308786	0.316985
80	Tlr3	0.03356	0.038133	0.048575	0.037533	0.526121	0.075002
81	Cisd1	1.835598	2.215811	2.51588	1.820311	0.236467	0.059429
82	Slc25a38	0.023206	0.038059	0.026684	0.031214	0.070787	0.727451
83	Slc25a28	0.122955	0.14652	0.103535	0.112261	0.224229	0.46567
84	Nox1	0.006174	0.006711	0.006229	0.005119	0.648028	0.155095
85	Fam132b	0.022474	0.025306	0.026509	0.023461	0.386068	0.348758
86	Bola2	1.552018	1.820475	1.465165	1.285875	0.08256	0.119444
87	Nox3	0.006174	0.006711	0.006229	0.005119	0.648028	0.155095
88	Slc11a2	0.160049	0.185315	0.243143	0.302872	0.542801	0.240097
89	Slc11a2	0.044632	0.03938	0.062076	0.046701	0.475314	0.01464
90	Iscu	3.725625	4.236106	4.066518	2.920808	0.308763	0.004343

APPENDIX XIV

APPENDIX XIV. Expression profile of 90 iron metabolism genes in kidney

Kidney							
	Gene name	Gene expression (2^(-ΔCt))				p-value	
		HRG1+/+ Standard	HRG1-/- Standard	HRG1+/+ 2ppm	HRG1-/- 2ppm	+/+ vs -/- Standard	+/+ vs -/- 2ppm
1	Ncoa4	1.513559	1.28202	0.898102	0.907504	0.1736	0.950794
2	Ankrd37	0.029142	0.023148	0.069268	0.028592	0.138407	0.199186
3	Smad7	0.137197	0.137694	0.088067	0.119587	0.977073	0.30222
4	Neo1	0.153181	0.177308	0.174018	0.137803	0.541968	0.137172
5	Mfsd7b	0.085726	0.089446	0.074088	0.078541	0.791126	0.818661
6	Steap3	0.057907	0.05378	0.061935	0.040484	0.741052	0.124405
7	Alas2	0.069139	0.034089	0.061478	0.06168	0.220845	0.99273
8	Steap2	0.312609	0.337242	0.223876	0.243704	0.810188	0.643705
9	Pcbp2	3.94274	3.598512	3.396793	3.236344	0.318805	0.700694
10	Slc39a8	0.458194	0.379128	0.254521	0.448878	0.49605	0.441777
11	Slc39a14	0.211629	0.166485	0.167922	0.206643	0.266334	0.199727
12	Hmox2	0.42318	0.407004	0.337739	0.389714	0.692318	0.538234
13	Slc11a2	0.34183	0.360294	0.293732	0.335713	0.772855	0.5823
14	Il12a	0.004645	0.003879	0.003802	0.003548	0.234888	0.658763
15	Heph	0.05569	0.063917	0.0531	0.056522	0.627037	0.735438
16	Fbxl5	0.394003	0.419545	0.350427	0.311443	0.304219	0.208803
17	Slc38a1	0.015691	0.014064	0.024973	0.014994	0.362215	0.076301
18	Cp	0.249568	0.213611	0.320409	0.332846	0.375082	0.900885
19	Nox4	1.665862	1.581599	1.157241	1.110812	0.888563	0.906679
20	Trfr2	0.00564	0.00537	0.005248	0.006483	0.852613	0.512809
21	Tlr7	0.010414	0.006997	0.015665	0.011231	0.315114	0.169703
22	Alas1	1.188382	1.01941	1.463099	1.104043	0.605904	0.571103
23	Aco1	1.406815	1.298365	0.935525	1.169077	0.441333	0.372107
24	Bmp6	0.26479	0.263341	0.205326	0.292529	0.944581	0.160257
25	Epo	0.004645	0.003879	0.012059	0.013186	0.234888	0.893449
26	Fech	0.825439	0.810884	0.632568	0.688628	0.842433	0.521691
27	Fxn	0.24796	0.24508	0.172015	0.194118	0.90697	0.476215
28	Ifnab	0.021862	0.015342	0.006295	0.011546	0.172385	0.085648
29	Il1b	0.02121	0.020247	0.024906	0.020693	0.838522	0.608971
30	Lcn2	0.015717	0.022173	0.045399	0.039986	0.620179	0.922122
31	Smad4	0.554963	0.59721	0.577837	0.611259	0.510358	0.669206
32	Trim27	0.331102	0.342718	0.29072	0.294957	0.805476	0.916454
33	Saa1	0.017354	0.010151	0.014972	0.053176	0.73087	0.5414
34	Stat6	0.015338	0.012935	0.013987	0.014714	0.16582	0.843519

35	Epas1	0.718012	0.655311	0.805434	0.813797	0.490888	0.973427
36	Fth1	111.9013	110.2752	75.69413	88.44987	0.789045	0.46176
37	Ftl1	23.54187	25.31998	15.93333	18.4622	0.447805	0.385427
38	Gast	0.004645	0.003879	0.003802	0.003548	0.234888	0.658763
39	Ggh	0.303096	0.302896	0.318241	0.229256	0.996568	0.009933
40	Herc2	0.301479	0.31797	0.301293	0.250579	0.717737	0.116359
41	Hfe	0.100404	0.106231	0.09523	0.079177	0.751637	0.231272
42	Hif1a	0.310568	0.319291	0.296756	0.276532	0.894726	0.807805
43	Hmox1	0.143608	0.133694	0.126591	0.09178	0.814412	0.109713
44	Id1	0.454278	0.541832	0.616308	0.568121	0.455781	0.83062
45	Ifna2	0.011409	0.00796	0.005141	0.007574	0.032769	0.287812
46	Ifna4	0.004645	0.003879	0.003802	0.003548	0.234888	0.658763
47	Ifnb1	0.006066	0.004712	0.003964	0.003857	0.240382	0.883257
48	Il10	0.004645	0.003879	0.003802	0.003548	0.234888	0.658763
49	Il1a	0.006141	0.005932	0.006022	0.007235	0.910309	0.692199
50	Nos2	0.56329	0.594628	0.310762	0.383068	0.800678	0.710929
51	Spic	0.004645	0.003879	0.004206	0.003548	0.234888	0.32807
52	Stat3	0.451136	0.439682	0.433415	0.466417	0.849857	0.573612
53	Tfrc	0.313642	0.388359	0.670269	0.917032	0.13453	0.551542
54	Pcbp1	1.730188	1.72758	1.494005	1.564463	0.990326	0.691797
55	Eif2ak1	0.387529	0.413438	0.324574	0.337392	0.462764	0.748108
56	Slc11a1	0.008045	0.007602	0.011372	0.008899	0.609153	0.176223
57	Neu3	0.020303	0.023411	0.022828	0.017948	0.098291	0.132742
58	Slc40a1	0.295049	0.307257	0.264701	0.308182	0.857874	0.603238
59	Il22	0.004645	0.003879	0.003802	0.003548	0.234888	0.658763
60	Hp	0.045247	0.063056	0.179769	0.283182	0.849294	0.689208
61	Hpx	0.067717	0.021878	0.079114	0.442642	0.445107	0.121291
62	Pcbp4	0.100075	0.136438	0.091864	0.120656	0.049089	0.399312
63	Pcbp3	0.178384	0.167869	0.167172	0.165449	0.627297	0.951444
64	Ireb2	0.549021	0.63373	0.409	0.444599	0.147266	0.70143
65	Ndfip1	2.242544	2.283968	2.021963	1.98158	0.830606	0.861206
66	Glrx3	0.897545	0.941499	0.773776	0.739943	0.417121	0.627132
67	Cisd2	0.140847	0.139944	0.083697	0.110701	0.973374	0.206642
68	Slc25a37	0.153897	0.120264	0.147322	0.109714	0.079446	0.045882
69	Slc48a1	1.238284	0.584859	1.067668	0.520679	0.003822	0.012404
70	Asb11	0.032436	0.015521	0.027778	0.028678	0.218226	0.96164
71	Hfe2	0.004645	0.004465	0.004843	0.006662	0.868974	0.447046
72	Steap1	0.043614	0.042866	0.078579	0.025085	0.979786	0.056822
73	Tmprss6	0.00738	0.007922	0.009734	0.012486	0.742665	0.55675
74	Cybrd1	0.007195	0.006367	0.006078	0.005117	0.729813	0.711579
75	Il6	0.004645	0.003879	0.003802	0.003548	0.234888	0.658763

76	Tlr9	0.013582	0.008742	0.013567	0.018153	0.007584	0.427263
77	Hamp	0.016196	0.009593	0.003802	0.009876	0.664902	0.36705
78	Steap4	0.010714	0.039598	0.075009	0.023004	0.151848	0.118793
79	Aco2	7.066896	7.880921	6.705484	7.121036	0.315248	0.773014
80	Tlr3	0.046437	0.038095	0.039815	0.046217	0.385355	0.493834
81	Cisd1	2.441503	2.407144	1.469222	2.041546	0.929555	0.24164
82	Slc25a38	0.006424	0.004918	0.004064	0.00511	0.415238	0.358185
83	Slc25a28	0.202118	0.177702	0.165656	0.1695	0.408074	0.918535
84	Nox1	0.004645	0.003879	0.003802	0.003548	0.234888	0.658763
85	Fam132b	0.02495	0.027947	0.030023	0.023723	0.634437	0.347538
86	Bola2	1.353151	1.467038	1.375678	1.227972	0.43727	0.203749
87	Nox3	0.004645	0.003879	0.003802	0.003548	0.234888	0.658763
88	Slc11a2	0.22337	0.245074	0.222163	0.288672	0.760397	0.461964
89	Slc11a2	0.072442	0.086877	0.058186	0.062868	0.445062	0.521276
90	Iscu	6.780631	6.647997	6.302668	5.543376	0.816341	0.205166

Chapter 8 Bibliography

1. Yuan X, Rietzschel N, Kwon H, et al. Regulation of intracellular heme trafficking revealed by subcellular reporters. *Proc Natl Acad Sci U S A*. 2016;113(35):E5144-5152.

2. Heinemann IU, Jahn M, Jahn D. The biochemistry of heme biosynthesis. *Arch Biochem Biophys*. 2008;474(2):238-251.

3. Kumar S, Bandyopadhyay U. Free heme toxicity and its detoxification systems in human. *Toxicol Lett*. 2005;157(3):175-188.

4. McKie AT. The role of Dcytb in iron metabolism: an update. *Biochem Soc Trans*. 2008;36(Pt 6):1239-1241.

5. Wang J, Pantopoulos K. Regulation of cellular iron metabolism. *Biochem J*. 2011;434(3):365-381.

6. Hentze MW, Muckenthaler MU, Galy B, Camaschella C. Two to tango: regulation of Mammalian iron metabolism. *Cell*. 2010;142(1):24-38.

7. Gkouvatsos K, Papanikolaou G, Pantopoulos K. Regulation of iron transport and the role of transferrin. *Biochim Biophys Acta*. 2012;1820(3):188-202.

8. Brissot P, Ropert M, Le Lan C, Loréal O. Non-transferrin bound iron: a key role in iron overload and iron toxicity. *Biochim Biophys Acta*. 2012;1820(3):403-410.

9. Liuzzi JP, Aydemir F, Nam H, Knutson MD, Cousins RJ. Zip14 (Slc39a14) mediates non-transferrin-bound iron uptake into cells. *Proc Natl Acad Sci U S A*. 2006;103(37):13612-13617.

10. Jenkitkasemwong S, Wang CY, Coffey R, et al. SLC39A14 Is Required for the Development of Hepatocellular Iron Overload in Murine Models of Hereditary Hemochromatosis. *Cell Metab*. 2015;22(1):138-150.

11. Bezwoda WR, Bothwell TH, Charlton RW, et al. The relative dietary importance of haem and non-haem iron. *S Afr Med J*. 1983;64(14):552-556.

12. Carpenter CE, Mahoney AW. Contributions of heme and nonheme iron to human nutrition. *Crit Rev Food Sci Nutr*. 1992;31(4):333-367.

13. Conrad ME, Weintraub LR, Sears DA, Crosby WH. Absorption of hemoglobin iron. *Am J Physiol*. 1966;211(5):1123-1130.

14. Brown EB, Hwang YF, Nicol S, Ternberg J. Absorption of radiation-labeled hemoglobin by dogs. *J Lab Clin Med*. 1968;72(1):58-64.

15. Grasbeck R, Majuri R, Kouvonen I, Tenhunen R. Spectral and other studies on the intestinal haem receptor of the pig. *Biochim Biophys Acta*. 1982;700(2):137-142.

16. Parmley RT, Barton JC, Conrad ME, Austin RL, Holland RM. Ultrastructural cytochemistry and radioautography of hemoglobin--iron absorption. *Exp Mol Pathol*. 1981;34(2):131-144.

17. West AR, Oates PS. Mechanisms of heme iron absorption: Current questions and controversies. *World J Gastroenterol*. 2008;14(26):4101-4110.

18. Quigley JG, Yang Z, Worthington MT, et al. Identification of a human heme exporter that is essential for erythropoiesis. *Cell*. 2004;118(6):757-766.

19. Qiu A, Jansen M, Sakaris A, et al. Identification of an intestinal folate transporter and the molecular basis for hereditary folate malabsorption. *Cell*. 2006;127(5):917-928.

20. Aich A, Freundlich M, Vekilov PG. The free heme concentration in healthy human erythrocytes. *Blood Cells Mol Dis*. 2015;55(4):402-409.

21. Carmona U, Li L, Zhang L, Knez M. Ferritin light-chain subunits: key elements for the electron transfer across the protein cage. *Chem Commun (Camb)*. 2014;50(97):15358-15361.

22. Kohgo Y, Ikuta K, Ohtake T, Torimoto Y, Kato J. Body iron metabolism and pathophysiology of iron overload. *Int J Hematol*. 2008;88(1):7-15.

23. Shi H, Bencze KZ, Stemmler TL, Philpott CC. A cytosolic iron chaperone that delivers iron to ferritin. *Science*. 2008;320(5880):1207-1210.

24. Ryu MS, Zhang D, Protchenko O, Shakoury-Elizeh M, Philpott CC. PCBP1 and NCOA4 regulate erythroid iron storage and heme biosynthesis. *J Clin Invest*. 2017;127(5):1786-1797.

25. Mancias JD, Wang X, Gygi SP, Harper JW, Kimmelman AC. Quantitative proteomics identifies NCOA4 as the cargo receptor mediating ferritinophagy. *Nature*. 2014;509(7498):105-109.

26. Bellelli R, Federico G, Matte' A, et al. NCOA4 Deficiency Impairs Systemic Iron Homeostasis. *Cell Rep*. 2016;14(3):411-421.

27. De Domenico I, Ward DM, Langelier C, et al. The molecular mechanism of hepcidin-mediated ferroportin down-regulation. *Mol Biol Cell*. 2007;18(7):2569-2578.

28. Nemeth E, Tuttle MS, Powelson J, et al. Hepcidin regulates cellular iron efflux by binding to ferroportin and inducing its internalization. *Science*. 2004;306(5704):2090-2093.

29. Brasse-Lagnel C, Karim Z, Letteron P, Bekri S, Bado A, Beaumont C. Intestinal DMT1 cotransporter is down-regulated by hepcidin via proteasome internalization and degradation. *Gastroenterology*. 2011;140(4):1261-1271.e1261.

30. Ganz T. Hepcidin and iron regulation, 10 years later. *Blood*. 2011;117(17):4425-4433.

31. Valore EV, Ganz T. Posttranslational processing of hepcidin in human hepatocytes is mediated by the prohormone convertase furin. *Blood Cells Mol Dis*. 2008;40(1):132-138.

32. Courselaud B, Pigeon C, Inoue Y, et al. C/EBPalpha regulates hepatic transcription of hepcidin, an antimicrobial peptide and regulator of iron metabolism. Cross-talk between C/EBP pathway and iron metabolism. *J Biol Chem*. 2002;277(43):41163-41170.

33. Steinbicker AU, Bartnikas TB, Lohmeyer LK, et al. Perturbation of hepcidin expression by BMP type I receptor deletion induces iron overload in mice. *Blood*. 2011;118(15):4224-4230.

34. Kautz L, Jung G, Valore EV, Rivella S, Nemeth E, Ganz T. Identification of erythroferrone as an erythroid regulator of iron metabolism. *Nat Genet*. 2014;46(7):678-684.

35. Babitt JL, Huang FW, Wrighting DM, et al. Bone morphogenetic protein signaling by hemojuvelin regulates hepcidin expression. *Nat Genet*. 2006;38(5):531-539.

36. Ramos E, Kautz L, Rodriguez R, et al. Evidence for distinct pathways of hepcidin regulation by acute and chronic iron loading in mice. *Hepatology*. 2011;53(4):1333-1341.

37. Casanovas G, Mleczko-Sanecka K, Altamura S, Hentze MW, Muckenthaler MU. Bone morphogenetic protein (BMP)-responsive elements located in the proximal and distal hepcidin promoter are critical for its response to HJV/BMP/SMAD. *J Mol Med (Berl)*. 2009;87(5):471-480.

38. Wang RH, Li C, Xu X, et al. A role of SMAD4 in iron metabolism through the positive regulation of hepcidin expression. *Cell Metab*. 2005;2(6):399-409.

39. Ganz T, Nemeth E. Hepcidin and disorders of iron metabolism. *Annu Rev Med*. 2011;62:347-360.

40. Meynard D, Kautz L, Darnaud V, Canonne-Hergaux F, Coppin H, Roth MP. Lack of the bone morphogenetic protein BMP6 induces massive iron overload. *Nat Genet*. 2009;41(4):478-481.

41. Andriopoulos B, Corradini E, Xia Y, et al. BMP6 is a key endogenous regulator of hepcidin expression and iron metabolism. *Nat Genet*. 2009;41(4):482-487.

42. Smith SR, Ghosh MC, Ollivierre-Wilson H, Hang Tong W, Rouault TA. Complete loss of iron regulatory proteins 1 and 2 prevents viability of murine zygotes

beyond the blastocyst stage of embryonic development. *Blood Cells Mol Dis*. 2006;36(2):283-287.

43. Galy B, Ferring-Appel D, Kaden S, Grone HJ, Hentze MW. Iron regulatory proteins are essential for intestinal function and control key iron absorption molecules in the duodenum. *Cell Metab*. 2008;7(1):79-85.

44. Galy B, Ferring-Appel D, Sauer SW, et al. Iron regulatory proteins secure mitochondrial iron sufficiency and function. *Cell Metab*. 2010;12(2):194-201.

45. Pantopoulos K, Porwal SK, Tartakoff A, Devireddy L. Mechanisms of mammalian iron homeostasis. *Biochemistry*. 2012;51(29):5705-5724.

46. Vashisht AA, Zumbrennen KB, Huang X, et al. Control of iron homeostasis by an iron-regulated ubiquitin ligase. *Science*. 2009;326(5953):718-721.

47. Moroishi T, Nishiyama M, Takeda Y, Iwai K, Nakayama KI. The FBXL5-IRP2 axis is integral to control of iron metabolism in vivo. *Cell Metab*. 2011;14(3):339-351.

48. Piccinelli P, Samuelsson T. Evolution of the iron-responsive element. *RNA*. 2007;13(7):952-966.

49. Zhang DL, Hughes RM, Ollivierre-Wilson H, Ghosh MC, Rouault TA. A ferroportin transcript that lacks an iron-responsive element enables duodenal and erythroid precursor cells to evade translational repression. *Cell Metab*. 2009;9(5):461-473.

50. Roy CN, Mak HH, Akpan I, Losyev G, Zurakowski D, Andrews NC. Hepcidin antimicrobial peptide transgenic mice exhibit features of the anemia of inflammation. *Blood*. 2007;109(9):4038-4044.

51. Nemeth E, Rivera S, Gabayan V, et al. IL-6 mediates hypoferremia of inflammation by inducing the synthesis of the iron regulatory hormone hepcidin. *J Clin Invest*. 2004;113(9):1271-1276.

52. Peyssonnaux C, Zinkernagel AS, Datta V, Lauth X, Johnson RS, Nizet V. TLR4-dependent hepcidin expression by myeloid cells in response to bacterial pathogens. *Blood*. 2006;107(9):3727-3732.

53. Theurl I, Theurl M, Seifert M, et al. Autocrine formation of hepcidin induces iron retention in human monocytes. *Blood*. 2008;111(4):2392-2399.

54. Lee P, Peng H, Gelbart T, Wang L, Beutler E. Regulation of hepcidin transcription by interleukin-1 and interleukin-6. *Proc Natl Acad Sci U S A*. 2005;102(6):1906-1910.

55. Wessling-Resnick M. Iron homeostasis and the inflammatory response. *Annu Rev Nutr*. 2010;30:105-122.

56. Sharma N, Laftah AH, Brookes MJ, Cooper B, Iqbal T, Tselepis C. A role for tumour necrosis factor alpha in human small bowel iron transport. *Biochem J*. 2005;390(Pt 2):437-446.

57. Atkinson SH, Rockett KA, Morgan G, et al. Tumor necrosis factor SNP haplotypes are associated with iron-deficiency anemia in West African children. *Blood*. 2008;112(10):4276-4283.

58. Laftah AH, Sharma N, Brookes MJ, et al. Tumour necrosis factor alpha causes hypoferraemia and reduced intestinal iron absorption in mice. *Biochem J*. 2006;397(1):61-67.

59. Weiss G, Werner-Felmayer G, Werner ER, Grünewald K, Wachter H, Hentze MW. Iron regulates nitric oxide synthase activity by controlling nuclear transcription. *J Exp Med*. 1994;180(3):969-976.

60. Omara FO, Blakley BR. The effects of iron-deficiency and iron overload on cell-mediated immunity in the mouse. *Br J Nutr*. 1994;72(6):899-909.

61. Hattangadi SM, Wong P, Zhang L, Flygare J, Lodish HF. From stem cell to red cell: regulation of erythropoiesis at multiple levels by multiple proteins, RNAs, and chromatin modifications. *Blood*. 2011;118(24):6258-6268.

62. Ghaffari S, Kitidis C, Zhao W, et al. AKT induces erythroid-cell maturation of JAK2-deficient fetal liver progenitor cells and is required for Epo regulation of erythroid-cell differentiation. *Blood*. 2006;107(5):1888-1891.

63. Socolovsky M, Nam H, Fleming MD, Haase VH, Brugnara C, Lodish HF. Ineffective erythropoiesis in Stat5a(-/-)5b(-/-) mice due to decreased survival of early erythroblasts. *Blood*. 2001;98(12):3261-3273.

64. Chen K, Liu J, Heck S, Chasis JA, An X, Mohandas N. Resolving the distinct stages in erythroid differentiation based on dynamic changes in membrane protein expression during erythropoiesis. *Proc Natl Acad Sci U S A*. 2009;106(41):17413-17418.

65. Paulson RF, Shi L, Wu DC. Stress erythropoiesis: new signals and new stress progenitor cells. *Curr Opin Hematol*. 2011;18(3):139-145.

66. Liao C, Prabhu KS, Paulson RF. Monocyte-derived macrophages expand the murine stress erythropoietic niche during the recovery from anemia. *Blood*. 2018;132(24):2580-2593.

67. Wang GL, Semenza GL. Molecular basis of hypoxia-induced erythropoietin expression. *Curr Opin Hematol*. 1996;3(2):156-162.

68. Liu Y, Pop R, Sadegh C, Brugnara C, Haase VH, Socolovsky M. Suppression of Fas-FasL coexpression by erythropoietin mediates erythroblast expansion during the erythropoietic stress response in vivo. *Blood*. 2006;108(1):123-133.

69. Wu DC, Paulson RF. Hypoxia regulates BMP4 expression in the murine spleen during the recovery from acute anemia. *PLoS One*. 2010;5(6):e11303.

70. Perry JM, Harandi OF, Paulson RF. BMP4, SCF, and hypoxia cooperatively regulate the expansion of murine stress erythroid progenitors. *Blood*. 2007;109(10):4494-4502.

71. Aisen P, Leibman A, Zweier J. Stoichiometric and site characteristics of the binding of iron to human transferrin. *J Biol Chem*. 1978;253(6):1930-1937.

72. Ohgami RS, Campagna DR, Greer EL, et al. Identification of a ferrireductase required for efficient transferrin-dependent iron uptake in erythroid cells. *Nat Genet*. 2005;37(11):1264-1269.

73. Gunshin H, Mackenzie B, Berger UV, et al. Cloning and characterization of a mammalian proton-coupled metal-ion transporter. *Nature*. 1997;388(6641):482-488.

74. Shaw GC, Cope JJ, Li L, et al. Mitoferrin is essential for erythroid iron assimilation. *Nature*. 2006;440(7080):96-100.

75. Troadec MB, Warner D, Wallace J, et al. Targeted deletion of the mouse Mitoferrin1 gene: from anemia to protoporphyria. *Blood*. 2011;117(20):5494-5502.

76. Dailey HA, Meissner PN. Erythroid heme biosynthesis and its disorders. *Cold Spring Harb Perspect Med*. 2013;3(4):a011676.

77. Cox TC, Bawden MJ, Abraham NG, et al. Erythroid 5-aminolevulinate synthase is located on the X chromosome. *Am J Hum Genet*. 1990;46(1):107-111.

78. Weiss MJ, Yu C, Orkin SH. Erythroid-cell-specific properties of transcription factor GATA-1 revealed by phenotypic rescue of a gene-targeted cell line. *Mol Cell Biol*. 1997;17(3):1642-1651.

79. Tanimura N, Miller E, Igarashi K, et al. Mechanism governing heme synthesis reveals a GATA factor/heme circuit that controls differentiation. *EMBO Rep*. 2016;17(2):249-265.

80. Sadlon TJ, Dell'Oso T, Surinya KH, May BK. Regulation of erythroid 5-aminolevulinate synthase expression during erythropoiesis. *Int J Biochem Cell Biol*. 1999;31(10):1153-1167.

81. Magness ST, Tugores A, Brenner DA. Analysis of ferrochelatase expression during hematopoietic development of embryonic stem cells. *Blood*. 2000;95(11):3568-3577.

82. Tugores A, Magness ST, Brenner DA. A single promoter directs both housekeeping and erythroid preferential expression of the human ferrochelatase gene. *J Biol Chem*. 1994;269(49):30789-30797.

83. Chan RY, Schulman HM, Ponka P. Expression of ferrochelatase mRNA in erythroid and non-erythroid cells. *Biochem J*. 1993;292 (Pt 2):343-349.

84. Elder GH, Gouya L, Whatley SD, Puy H, Badminton MN, Deybach JC. The molecular genetics of erythropoietic protoporphyria. *Cell Mol Biol (Noisy-le-grand)*. 2009;55(2):118-126.

85. Tahara T, Sun J, Nakanishi K, et al. Heme positively regulates the expression of beta-globin at the locus control region via the transcriptional factor Bach1 in erythroid cells. *J Biol Chem*. 2004;279(7):5480-5487.

86. BESSIS M. [Erythroblastic island, functional unity of bone marrow]. *Rev Hematol*. 1958;13(1):8-11.

87. Leimberg MJ, Prus E, Konijn AM, Fibach E. Macrophages function as a ferritin iron source for cultured human erythroid precursors. *J Cell Biochem*. 2008;103(4):1211-1218.

88. Rhodes MM, Kopsombut P, Bondurant MC, Price JO, Koury MJ. Adherence to macrophages in erythroblastic islands enhances erythroblast proliferation and increases erythrocyte production by a different mechanism than erythropoietin. *Blood*. 2008;111(3):1700-1708.

89. Seki M, Shirasawa H. Role of the reticular cells during maturation process of the erythroblast. 3. The fate of phagocytized nucleus. *Acta Pathol Jpn*. 1965;15(4):387-405.

90. Soni S, Bala S, Gwynn B, Sahr KE, Peters LL, Hanspal M. Absence of erythroblast macrophage protein (Emp) leads to failure of erythroblast nuclear extrusion. *J Biol Chem*. 2006;281(29):20181-20189.

91. Lee JC, Gimm JA, Lo AJ, et al. Mechanism of protein sorting during erythroblast enucleation: role of cytoskeletal connectivity. *Blood*. 2004;103(5):1912-1919.

92. Kawane K, Fukuyama H, Kondoh G, et al. Requirement of DNase II for definitive erythropoiesis in the mouse fetal liver. *Science*. 2001;292(5521):1546-1549.

93. Keel SB, Doty RT, Yang Z, et al. A heme export protein is required for red blood cell differentiation and iron homeostasis. *Science*. 2008;319(5864):825-828.

94. Chiabrando D, Marro S, Mercurio S, et al. The mitochondrial heme exporter FLVCR1b mediates erythroid differentiation. *J Clin Invest*. 2012;122(12):4569-4579.

95. Beaumont C, Delaby C. Recycling iron in normal and pathological states. *Semin Hematol*. 2009;46(4):328-338.

96. Low PS, Waugh SM, Zinke K, Drenckhahn D. The role of hemoglobin denaturation and band 3 clustering in red blood cell aging. *Science*. 1985;227(4686):531-533.

97. Pantaleo A, Giribaldi G, Mannu F, Arese P, Turrini F. Naturally occurring anti-band 3 antibodies and red blood cell removal under physiological and pathological conditions. *Autoimmun Rev*. 2008;7(6):457-462.

98. Boas FE, Forman L, Beutler E. Phosphatidylserine exposure and red cell viability in red cell aging and in hemolytic anemia. *Proc Natl Acad Sci U S A*. 1998;95(6):3077-3081.

99. Lee SJ, Park SY, Jung MY, Bae SM, Kim IS. Mechanism for phosphatidylserine-dependent erythrophagocytosis in mouse liver. *Blood*. 2011;117(19):5215-5223.

100. Ravichandran KS. Find-me and eat-me signals in apoptotic cell clearance: progress and conundrums. *J Exp Med*. 2010;207(9):1807-1817.

101. Igarashi K, Watanabe-Matsui M. Wearing red for signaling: the heme-bach axis in heme metabolism, oxidative stress response and iron immunology. *Tohoku J Exp Med*. 2014;232(4):229-253.

102. Zhou Y, Wu H, Zhao M, Chang C, Lu Q. The Bach Family of Transcription Factors: A Comprehensive Review. *Clin Rev Allergy Immunol*. 2016;50(3):345-356.

103. Ogawa K, Sun J, Taketani S, et al. Heme mediates derepression of Maf recognition element through direct binding to transcription repressor Bach1. *Embo J*. 2001;20(11):2835-2843.

104. Zenke-Kawasaki Y, Dohi Y, Katoh Y, et al. Heme induces ubiquitination and degradation of the transcription factor Bach1. *Mol Cell Biol*. 2007;27(19):6962-6971.

105. Suzuki H, Tashiro S, Hira S, et al. Heme regulates gene expression by triggering Crm1-dependent nuclear export of Bach1. *EMBO J*. 2004;23(13):2544-2553.

106. Haldar M, Kohyama M, So AY, et al. Heme-mediated SPI-C induction promotes monocyte differentiation into iron-recycling macrophages. *Cell*. 2014;156(6):1223-1234.

107. Delaby C, Rondeau C, Pouzet C, et al. Subcellular localization of iron and heme metabolism related proteins at early stages of erythrophagocytosis. *PloS one*. 2012;7(7):e42199.

108. Soe-Lin S, Apte SS, Andriopoulos B, et al. Nramp1 promotes efficient macrophage recycling of iron following erythrophagocytosis in vivo. *Proc Natl Acad Sci U S A*. 2009;106(14):5960-5965.

109. White C, Yuan X, Schmidt PJ, et al. HRG1 Is Essential for Heme Transport from the Phagolysosome of Macrophages during Erythrophagocytosis. *Cell Metab*. 2013;17(2):261-270.

110. Khan AA, Quigley JG. Heme and FLVCR-related transporter families SLC48 and SLC49. *Mol Aspects Med*. 2013;34(2-3):669-682.

111. Delaby C, Pilard N, Goncalves AS, Beaumont C, Canonne-Hergaux F. Presence of the iron exporter ferroportin at the plasma membrane of macrophages is enhanced by iron loading and down-regulated by hepcidin. *Blood*. 2005;106(12):3979-3984.

112. Delanghe JR, Langlois MR. Hemopexin: a review of biological aspects and the role in laboratory medicine. *Clin Chim Acta*. 2001;312(1-2):13-23.

113. Wang Y, Kinzie E, Berger FG, Lim SK, Baumann H. Haptoglobin, an inflammation-inducible plasma protein. *Redox Rep*. 2001;6(6):379-385.

114. Gordon S, Cleve H, Bearn AG. An improved method of preparing haptoglobin polypeptide chains using guanidine hydrochloride. *Proc Soc Exp Biol Med*. 1968;127(1):52-59.

115. Wejman JC, Hovsepian D, Wall JS, Hainfeld JF, Greer J. Structure and assembly of haptoglobin polymers by electron microscopy. *J Mol Biol*. 1984;174(2):343-368.

116. Andersen CB, Torvund-Jensen M, Nielsen MJ, et al. Structure of the haptoglobin-haemoglobin complex. *Nature*. 2012;489(7416):456-459.

117. Smith A, McCulloh RJ. Hemopexin and haptoglobin: allies against heme toxicity from hemoglobin not contenders. *Front Physiol*. 2015;6:187.

118. Kino K, Tsunoo H, Higa Y, Takami M, Nakajima H. Kinetic aspects of hemoglobin.haptoglobin-receptor interaction in rat liver plasma membranes, isolated liver cells, and liver cells in primary culture. *J Biol Chem*. 1982;257(9):4828-4833.

119. Takahashi N, Takahashi Y, Putnam FW. Complete amino acid sequence of human hemopexin, the heme-binding protein of serum. *Proc Natl Acad Sci U S A*. 1985;82(1):73-77.

120. Hrkal Z, Vodrázka Z, Kalousek I. Transfer of heme from ferrihemoglobin and ferrihemoglobin isolated chains to hemopexin. *Eur J Biochem*. 1974;43(1):73-78.

121. Morgan WT, Muster P, Tatum FM, et al. Use of hemopexin domains and monoclonal antibodies to hemopexin to probe the molecular determinants of hemopexin-mediated heme transport. *J Biol Chem*. 1988;263(17):8220-8225.

122. Thorbecke GJ, Liem HH, Knight S, Cox K, Muller-Eberhard U. Sites of formation of the serum proteins transferrin and hemopexin. *J Clin Invest*. 1973;52(3):725-731.

123. Swerts JP, Soula C, Sagot Y, et al. Hemopexin is synthesized in peripheral nerves but not in central nervous system and accumulates after axotomy. *J Biol Chem*. 1992;267(15):10596-10600.

124. Chen W, Lu H, Dutt K, Smith A, Hunt DM, Hunt RC. Expression of the protective proteins hemopexin and haptoglobin by cells of the neural retina. *Exp Eye Res*. 1998;67(1):83-93.

125. Grinberg LN, O'Brien PJ, Hrkal Z. The effects of heme-binding proteins on the peroxidative and catalatic activities of hemin. *Free Radic Biol Med*. 1999;27(1-2):214-219.

126. Tolosano E, Hirsch E, Patrucco E, et al. Defective recovery and severe renal damage after acute hemolysis in hemopexin-deficient mice. *Blood*. 1999;94(11):3906-3914.

127. Smith A, Morgan WT. Haem transport to the liver by haemopexin. Receptor-mediated uptake with recycling of the protein. *Biochem J*. 1979;182(1):47-54.

128. Braggins PE, Trakshel GM, Kutty RK, Maines MD. Characterization of two heme oxygenase isoforms in rat spleen: comparison with the hematin-induced and constitutive isoforms of the liver. *Biochem Biophys Res Commun*. 1986;141(2):528-533.

129. Maines MD, Trakshel GM, Kutty RK. Characterization of two constitutive forms of rat liver microsomal heme oxygenase. Only one molecular species of the enzyme is inducible. *J Biol Chem*. 1986;261(1):411-419.

130. Trakshel GM, Kutty RK, Maines MD. Purification and characterization of the major constitutive form of testicular heme oxygenase. The noninducible isoform. *J Biol Chem*. 1986;261(24):11131-11137.

131. Yoshida T, Sato M. Posttranslational and direct integration of heme oxygenase into microsomes. *Biochem Biophys Res Commun*. 1989;163(2):1086-1092.

132. Linnenbaum M, Busker M, Kraehling JR, Behrends S. Heme oxygenase isoforms differ in their subcellular trafficking during hypoxia and are differentially modulated by cytochrome P450 reductase. *PLoS One*. 2012;7(4):e35483.

133. Wang M, Roberts DL, Paschke R, Shea TM, Masters BS, Kim JJ. Three-dimensional structure of NADPH-cytochrome P450 reductase: prototype for FMN- and FAD-containing enzymes. *Proc Natl Acad Sci U S A*. 1997;94(16):8411-8416.

134. Schacter BA, Nelson EB, Marver HS, Masters BS. Immunochemical evidence for an association of heme oxygenase with the microsomal electron transport system. *J Biol Chem*. 1972;247(11):3601-3607.

135. Tenhunen R, Marver HS, Schmid R. Microsomal heme oxygenase. Characterization of the enzyme. *J Biol Chem*. 1969;244(23):6388-6394.

136. Ryter SW, Alam J, Choi AM. Heme oxygenase-1/carbon monoxide: from basic science to therapeutic applications. *Physiol Rev*. 2006;86(2):583-650.

137. Kovtunovych G, Eckhaus MA, Ghosh MC, Ollivierre-Wilson H, Rouault TA. Dysfunction of the heme recycling system in heme oxygenase 1-deficient mice: effects on macrophage viability and tissue iron distribution. *Blood*. 2010;116(26):6054-6062.

138. Chiabrando D, Vinchi F, Fiorito V, Mercurio S, Tolosano E. Heme in pathophysiology: a matter of scavenging, metabolism and trafficking across cell membranes. *Front Pharmacol*. 2014;5:61.

139. Beppu M, Nagoya M, Kikugawa K. Role of heme compounds in the erythrocyte membrane damage induced by lipid hydroperoxide. *Chem Pharm Bull (Tokyo)*. 1986;34(12):5063-5070.

140. Aft RL, Mueller GC. Hemin-mediated oxidative degradation of proteins. *J Biol Chem*. 1984;259(1):301-305.

141. Aft RL, Mueller GC. Hemin-mediated DNA strand scission. *J Biol Chem*. 1983;258(19):12069-12072.

142. Chou AC, Fitch CD. Mechanism of hemolysis induced by ferriprotoporphyrin IX. *J Clin Invest*. 1981;68(3):672-677.

143. Kirschner-Zilber I, Rabizadeh E, Shaklai N. The interaction of hemin and bilirubin with the human red cell membrane. *Biochim Biophys Acta*. 1982;690(1):20-30.

144. Wagener FA, Feldman E, de Witte T, Abraham NG. Heme induces the expression of adhesion molecules ICAM-1, VCAM-1, and E selectin in vascular endothelial cells. *Proc Soc Exp Biol Med*. 1997;216(3):456-463.

145. Belcher JD, Chen C, Nguyen J, et al. Heme triggers TLR4 signaling leading to endothelial cell activation and vaso-occlusion in murine sickle cell disease. *Blood*. 2014;123(3):377-390.

146. Graça-Souza AV, Arruda MA, de Freitas MS, Barja-Fidalgo C, Oliveira PL. Neutrophil activation by heme: implications for inflammatory processes. *Blood*. 2002;99(11):4160-4165.

147. Porto BN, Alves LS, Fernández PL, et al. Heme induces neutrophil migration and reactive oxygen species generation through signaling pathways characteristic of chemotactic receptors. *J Biol Chem*. 2007;282(33):24430-24436.

148. Natarajan R, Fisher BJ, Fowler AA. Hypoxia inducible factor-1 modulates hemin-induced IL-8 secretion in microvascular endothelium. *Microvasc Res*. 2007;73(3):163-172.

149. Figueiredo RT, Fernandez PL, Mourao-Sa DS, et al. Characterization of heme as activator of Toll-like receptor 4. *J Biol Chem*. 2007;282(28):20221-20229.

150. Dutra FF, Bozza MT. Heme on innate immunity and inflammation. *Front Pharmacol*. 2014;5:115.

151. Monteiro AP, Pinheiro CS, Luna-Gomes T, et al. Leukotriene B4 mediates neutrophil migration induced by heme. *J Immunol*. 2011;186(11):6562-6567.

152. Stocker R, Yamamoto Y, McDonagh AF, Glazer AN, Ames BN. Bilirubin is an antioxidant of possible physiological importance. *Science*. 1987;235(4792):1043-1046.

153. Otterbein LE, Bach FH, Alam J, et al. Carbon monoxide has anti-inflammatory effects involving the mitogen-activated protein kinase pathway. *Nat Med*. 2000;6(4):422-428.

154. Eisenstein RS, Garcia-Mayol D, Pettingell W, Munro HN. Regulation of ferritin and heme oxygenase synthesis in rat fibroblasts by different forms of iron. *Proc Natl Acad Sci U S A*. 1991;88(3):688-692.

155. Toh SQ, Glanfield A, Gobert GN, Jones MK. Heme and blood-feeding parasites: friends or foes? *Parasit Vectors*. 2010;3:108.

156. Chang KP, Chang CS, Sassa S. Heme biosynthesis in bacterium-protozoon symbioses: enzymic defects in host hemoflagellates and complemental role of their intracellular symbiotes. *Proc Natl Acad Sci U S A*. 1975;72(8):2979-2983.

157. Braz GR, Coelho HS, Masuda H, Oliveira PL. A missing metabolic pathway in the cattle tick Boophilus microplus. *Curr Biol*. 1999;9(13):703-706.

158. Dutta S, Furuyama K, Sassa S, Chang KP. Leishmania spp.: delta-aminolevulinate-inducible neogenesis of porphyria by genetic complementation of incomplete heme biosynthesis pathway. *Exp Parasitol*. 2008;118(4):629-636.

159. Wu B, Novelli J, Foster J, et al. The heme biosynthetic pathway of the obligate Wolbachia endosymbiont of Brugia malayi as a potential anti-filarial drug target. *PLoS Negl Trop Dis*. 2009;3(7):e475.

160. Bonday ZQ, Taketani S, Gupta PD, Padmanaban G. Heme biosynthesis by the malarial parasite. Import of delta-aminolevulinate dehydrase from the host red cell. *J Biol Chem*. 1997;272(35):21839-21846.

161. Padmanaban G, Nagaraj VA, Rangarajan PN. An alternative model for heme biosynthesis in the malarial parasite. *Trends Biochem Sci*. 2007;32(10):443-449.

162. Taylor MC, Kelly JM. Iron metabolism in trypanosomatids, and its crucial role in infection. *Parasitology*. 2010;137(6):899-917.

163. Perally S, Lacourse EJ, Campbell AM, Brophy PM. Heme transport and detoxification in nematodes: subproteomics evidence of differential role of glutathione transferases. *J Proteome Res*. 2008;7(10):4557-4565.

164. Coronado LM, Nadovich CT, Spadafora C. Malarial Hemozoin: From target to tool. *Biochim Biophys Acta*. 2014;1840(6):2032-2041.

165. Orjih AU. On the mechanism of hemozoin production in malaria parasites: activated erythrocyte membranes promote beta-hematin synthesis. *Exp Biol Med (Maywood)*. 2001;226(8):746-752.

166. Sienkiewicz A, Krzystek J, Vileno B, et al. Multi-frequency high-field EPR study of iron centers in malarial pigments. *J Am Chem Soc*. 2006;128(14):4534-4535.

167. Dorn A, Stoffel R, Matile H, Bubendorf A, Ridley RG. Malarial haemozoin/beta-haematin supports haem polymerization in the absence of protein. *Nature*. 1995;374(6519):269-271.

168. Egan TJ, Mavuso WW, Ncokazi KK. The mechanism of beta-hematin formation in acetate solution. Parallels between hemozoin formation and biomineralization processes. *Biochemistry*. 2001;40(1):204-213.

169. Klonis N, Tan O, Jackson K, Goldberg D, Klemba M, Tilley L. Evaluation of pH during cytostomal endocytosis and vacuolar catabolism of haemoglobin in Plasmodium falciparum. *Biochem J*. 2007;407(3):343-354.

170. Skelly PJ, Da'dara AA, Li XH, Castro-Borges W, Wilson RA. Schistosome feeding and regurgitation. *PLoS Pathog*. 2014;10(8):e1004246.

171. Noland GS, Briones N, Sullivan DJ. The shape and size of hemozoin crystals distinguishes diverse Plasmodium species. *Mol Biochem Parasitol*. 2003;130(2):91-99.

172. Ganz T, Nemeth E. Regulation of iron acquisition and iron distribution in mammals. *Biochim Biophys Acta*. 2006;1763(7):690-699.

173. Yen ST, Zhang M, Deng JM, et al. Somatic mosaicism and allele complexity induced by CRISPR/Cas9 RNA injections in mouse zygotes. *Dev Biol*. 2014;393(1):3-9.

174. Zhang J, Chambers I, Yun S, Phillips J, Krause M, Hamza I. Hrg1 promotes heme-iron recycling during hemolysis in the zebrafish kidney. *PLoS Genet*. 2018;14(9):e1007665.

175. Babicki S, Arndt D, Marcu A, et al. Heatmapper: web-enabled heat mapping for all. *Nucleic Acids Res*. 2016;44(W1):W147-153.

176. Bhattacharjee A, Yang H, Duffy M, et al. The Activity of Menkes Disease Protein ATP7A Is Essential for Redox Balance in Mitochondria. *J Biol Chem*. 2016;291(32):16644-16658.

177. Chen S, Paunesku T, Yuan Y, et al. The Bionanoprobe: Synchrotron-based Hard X-ray Fluorescence Microscopy for 2D/3D Trace Element Mapping. *Micros Today*. 2015;23(3):26-29.

178. Vogt S. MAPS : A set of software tools for analysis and visualization of 3D X-ray fluorescence data sets. *J Phys IV France*. 2003;104:635-638.

179. Nishibori E, Takata M, Kato K, et al. The large Debye–Scherrer camera installed at SPring-8 BL02B2 for charge density studies. *Journal of Physics and Chemistry of Solids*. 2001;62(12):2095-2098.

180. Straasø T, Kapishnikov S, Kato K, Takata M, Als-Nielsen J, Leiserowitz L. The Role of the Four Stereoisomers of the Heme Fe–O Cyclic Dimer in the Crystalline Phase Behavior of Synthetic Hemozoin: Relevance to Native Hemozoin Crystallization. *Crystal Growth & Design*. 2011;11(8):3342-3350.

181. Nishibori E, Sunaoshi E, Yoshida A, et al. Accurate structure factors and experimental charge densities from synchrotron X-ray powder diffraction data at SPring-8. *Acta Crystallographica Section A*. 2007;63(1):43-52.

182. Deroost K, Lays N, Noppen S, Martens E, Opdenakker G, Van den Steen PE. Improved methods for haemozoin quantification in tissues yield organ-and parasite-specific information in malaria-infected mice. *Malar J*. 2012;11:166.

183. Barr I, Guo F. Pyridine Hemochromagen Assay for Determining the Concentration of Heme in Purified Protein Solutions. *Bio Protoc*. 2015;5(18).

184. Institute TB.

185. Lin HH, Faunce DE, Stacey M, et al. The macrophage F4/80 receptor is required for the induction of antigen-specific efferent regulatory T cells in peripheral tolerance. *J Exp Med*. 2005;201(10):1615-1625.

186. Huynh KK, Eskelinen EL, Scott CC, Malevanets A, Saftig P, Grinstein S. LAMP proteins are required for fusion of lysosomes with phagosomes. *EMBO J*. 2007;26(2):313-324.

187. Shio MT, Kassa FA, Bellemare MJ, Olivier M. Innate inflammatory response to the malarial pigment hemozoin. *Microbes Infect*. 2010;12(12-13):889-899.

188. Schwarzer E, Turrini F, Giribaldi G, Cappadoro M, Arese P. Phagocytosis of P. falciparum malarial pigment hemozoin by human monocytes inactivates monocyte protein kinase C. *Biochim Biophys Acta*. 1993;1181(1):51-54.

189. van Rooijen N, Sanders A, van den Berg TK. Apoptosis of macrophages induced by liposome-mediated intracellular delivery of clodronate and propamidine. *J Immunol Methods*. 1996;193(1):93-99.

190. Ramos P, Casu C, Gardenghi S, et al. Macrophages support pathological erythropoiesis in polycythemia vera and β-thalassemia. *Nat Med*. 2013;19(4):437-445.

191. Sorbie J, Valberg LS. Iron balance in the mouse. *Lab Anim Sci*. 1974;24(6):900-904.

192. Silvestri L, Pagani A, Nai A, De Domenico I, Kaplan J, Camaschella C. The serine protease matriptase-2 (TMPRSS6) inhibits hepcidin activation by cleaving membrane hemojuvelin. *Cell Metab*. 2008;8(6):502-511.

193. Ahmad KA, Ahmann JR, Migas MC, et al. Decreased liver hepcidin expression in the Hfe knockout mouse. *Blood Cells Mol Dis*. 2002;29(3):361-366.

194. Bridle KR, Frazer DM, Wilkins SJ, et al. Disrupted hepcidin regulation in HFE-associated haemochromatosis and the liver as a regulator of body iron homoeostasis. *Lancet*. 2003;361(9358):669-673.

195. Wrighting DM, Andrews NC. Interleukin-6 induces hepcidin expression through STAT3. *Blood*. 2006;108(9):3204-3209.

196. Smith CL, Arvedson TL, Cooke KS, et al. IL-22 regulates iron availability in vivo through the induction of hepcidin. *J Immunol*. 2013;191(4):1845-1855.

197. Silva I, Rausch V, Peccerella T, Millonig G, Seitz HK, Mueller S. Hypoxia enhances H 2O2-mediated upregulation of hepcidin: Evidence for NOX4-mediated iron regulation. *Redox Biol*. 2018;16:1-10.

198. Shimada T. [Experimental studies on tissue level of amphotericin B]. *Tsurumi Shigaku*. 1977;3(2):101-104.

199. Paine A, Eiz-Vesper B, Blasczyk R, Immenschuh S. Signaling to heme oxygenase-1 and its anti-inflammatory therapeutic potential. *Biochem Pharmacol*. 2010;80(12):1895-1903.

200. Alcaraz MJ, Fernández P, Guillén MI. Anti-inflammatory actions of the heme oxygenase-1 pathway. *Curr Pharm Des*. 2003;9(30):2541-2551.

201. Lenox LE, Shi L, Hegde S, Paulson RF. Extramedullary erythropoiesis in the adult liver requires BMP-4/Smad5-dependent signaling. *Exp Hematol*. 2009;37(5):549-558.

202. Bilzer M, Roggel F, Gerbes AL. Role of Kupffer cells in host defense and liver disease. *Liver Int*. 2006;26(10):1175-1186.

203. Cabantchik ZI. Labile iron in cells and body fluids: physiology, pathology, and pharmacology. *Front Pharmacol*. 2014;5:45.

204. Knutson MD. Non-transferrin-bound iron transporters. *Free Radic Biol Med*. 2019;133:101-111.

205. Lynch SR. Why nutritional iron-deficiency persists as a worldwide problem. *J Nutr*. 2011;141(4):763S-768S.

206. Viteri FE, Ali F, Tujague J. Long-term weekly iron supplementation improves and sustains nonpregnant women's iron status as well or better than currently recommended short-term daily supplementation. *J Nutr*. 1999;129(11):2013-2020.

207. Fillebeen C, Gkouvatsos K, Fragoso G, et al. Mice are poor heme absorbers and do not require intestinal Hmox1 for dietary heme iron assimilation. *Haematologica*. 2015;100(9):e334-337.

208. Wang F, Paradkar PN, Custodio AO, et al. Genetic variation in Mon1a affects protein trafficking and modifies macrophage iron loading in mice. *Nat Genet*. 2007;39(8):1025-1032.

209. Uc A, Stokes JB, Britigan BE. Heme transport exhibits polarity in Caco-2 cells: evidence for an active and membrane protein-mediated process. *Am J Physiol Gastrointest Liver Physiol*. 2004;287(6):G1150-1157.

210. Zhang Q, Widmer G, Tzipori S. A pig model of the human gastrointestinal tract. *Gut Microbes*. 2013;4(3):193-200.

211. VENN JA, MCCANCE RA, WIDDOWSON EM. Iron metabolism in piglet anaemia. *J Comp Pathol Ther*. 1947;57(4):314-325.

212. EJ U. The Mineral Nutrition of Livestock (ed 2nd). Slough, UK: Commonwealth Agricultural Bureaux; 1981.

213. Staron R, Lipinski P, Lenartowicz M, et al. Dietary hemoglobin rescues young piglets from severe iron-deficiency anemia: Duodenal expression profile of genes involved in heme iron absorption. *PLoS One*. 2017;12(7):e0181117.

214. Trinder D, Oates PS, Thomas C, Sadleir J, Morgan EH. Localisation of divalent metal transporter 1 (DMT1) to the microvillus membrane of rat duodenal enterocytes in iron-deficiency, but to hepatocytes in iron overload. *Gut*. 2000;46(2):270-276.

215. Rajagopal A, Rao AU, Amigo J, et al. Haem homeostasis is regulated by the conserved and concerted functions of HRG-1 proteins. *Nature*. 2008;453(7198):1127-1131.

216. Mouse Cell Atlas.

217. Lohrig K, Wolters D. Multidimensional protein identification technology. *Methods Mol Biol*. 2009;564:143-153.

218. Spence JR, Mayhew CN, Rankin SA, et al. Directed differentiation of human pluripotent stem cells into intestinal tissue in vitro. *Nature*. 2011;470(7332):105-109.

219. Donovan A, Lima CA, Pinkus JL, et al. The iron exporter ferroportin/Slc40a1 is essential for iron homeostasis. *Cell Metab*. 2005;1(3):191-200.

220. Ferreira C, Bucchini D, Martin ME, et al. Early embryonic lethality of H ferritin gene deletion in mice. *J Biol Chem*. 2000;275(5):3021-3024.